Title
Modeling Vascular Homeostasis and Improving Data Filtering Methods for Model Calibration

Author
Wu, Jiacheng

Publication Date
2019

Peer reviewed|Thesis/dissertation

Modeling Vascular Homeostasis and Improving Data Filtering Methods for Model Calibration

by

Jiacheng Wu

A dissertation submitted in partial satisfaction of the

requirements for the degree of

Doctor of Philosophy

in

Engineering − Mechanical Engineering

and the Designated Emphasis

in

Computational Science and Engineering

in the

Graduate Division

of the

University of California, Berkeley

Committee in charge:

Professor Shawn C. Shadden, Chair
Professor Grace D. O'Connell
Professor Peter L. Bartlett

Spring 2019

Modeling Vascular Homeostasis and Improving Data Filtering Methods for Model Calibration

Abstract

Modeling Vascular Homeostasis and Improving Data Filtering Methods for Model Calibration

by

Jiacheng Wu

Doctor of Philosophy in Engineering − Mechanical Engineering
and the Designated Emphasis in
Computational Science and Engineering

University of California, Berkeley

Professor Shawn C. Shadden, Chair

Vascular homeostasis is the preferred state that blood vessels try to maintain against external mechanical and chemical stimuli. The vascular adaptive behavior around the homeostatic state is closely related to cardiovascular disease progressions such as arterial aneurysms. In this work, we develop a multi-physics computational framework that couples vascular growth & remodeling (G&R), wall mechanics and hemodynamics to describe the overall vascular adaptive behavior. The coupled simulation is implemented in patient-specific geometries to predict aneurysm progression. Lyapunov stability analysis of the governing equations for vascular adaptation is conducted to obtain a stabilizing criterion for aneurysm rupture. Also, to facilitate patient-specific computations, an algorithm is proposed to generate vascular homeostatic states by incorporating non-uniform residual stress and specifying optimal collagen fiber deposition angles. Since the accuracy and effectiveness of the computational models relies on properly estimating the unknown/hidden model parameters, we also demonstrate recent progress on improving data filtering techniques for inverse problems derived from model calibration. First, iterative ensemble Kalman filter (IEnKF) is applied to solve the inverse problems. The convergence of standard IEnKF is discussed and we show that the poor convergence of IEnKF is caused by the covariance shrinkage effect of the standard Kalman updates. An ensemble resampling based method is proposed to resolve this issue by perturbing the covariance shrinking via ensemble resampling and ensuring "correct" update directions by keeping the first and second moments of the resampling distribution unchanged. In the case of ill-posed inverse problems, we demonstrate that solution non-uniqueness can be overcome by incorporating additional constraints in a Bayesian inference framework. Constraints are imposed by defining a constraint likelihood function, and the method is demonstrated in both exact Bayesian and approximate Bayesian inference scenarios.

To my parents.

Contents

List of Figures

List of Tables

Acknowledgments

I always feel I am very fortunate to have Prof Shawn Shadden as my PhD advisor and sometimes I even wonder how my research career will be if I never met him before. I got to know Shawn when I took my first course on dynamical system with him. I enjoyed the course a lot and our mutual interest in applied math resonated. During my PhD years at Berkeley, he led me through ups and downs. Especially when I got stuck in my research, he is always very patient and willing to give me constructive suggestions and connect me to external collaborators and other resources. I learned a lot from him about how to approach a problem, ask the right question and do high-standard research. He also taught me how to stay positive and believe in myself when facing a challenge. He knows my strength and weakness, being supportive and open to new ideas, and let me pursuit the research direction that excites me and make the most of it. This makes the second part of my thesis on physics-informed inference possible. His positive influence will continue in my future career.

I also benefit a lot during my interactions with other mentors and collaborators. I first want to thank Prof Jay Humphrey from Yale University. His significant research work on vascular growth and remodeling lays the foundation of mathematical modeling of vascular adaptation which is the focus of the first part of my thesis. I was lucky enough to do a summer research with him at Yale in 2017. His advice about going into the research direction that I am really good at and excited about gave me the courage to discard some branches of research in order to focus more on physics-informed inference, which really excited me and suited my background. I want to thank Dr. Christoph Augustin who worked together with me on modeling vascular homeostasis. The fact that he is an expert in both computational biomechanics research and a variety of outdoor sports really sets a great example for my future career and life. I also want to thank Prof Jian-Xun Wang from University of Notre Dame. I still remember the fruitful spring and summer of 2018 when we worked together on Bayesian statistics, date assimilation, constrained inverse problem and derivative-free optimization which led to several papers and helped me land on my new job. I am also grateful to my PhD thesis committee, Prof Grace O'Connell and Prof Peter Bartlett for discussing about my thesis and providing constructive suggestions. Apart from those I met in my PhD years, I would also like to thank my undergraduate research mentors Prof Xiaofeng Lei and Prof Bin Zi. They took good care of me when I was at CUMT and motivated me to pursuit a research career path.

To all my friends I made at Berkeley, I owe you big thanks for being alongside with me for this wonderful journey. I want to first thank my lab mates at Shadden Lab and the Berkeley Biomechanics Group: Amir Arzani, Siavash Ameli, Kirk Hansen, Adam Updegrove, Jeffrey Pyne, Sarah Frank, Debanjan Mukherjee, Miguel Rodriguez, Mehran Mirramezani, Fanwei Kong, Chi Zhu, Jacob Wolf, Jaiyoung Ryu, Jessica Oakes, Neel Jani and Jonathan McKinley. Among them, I would like to specifically thank Kirk Hansen for frequently discussing with me, giving critical insights about my research, and helping me when I encountered life difficulties. Soccer is a big part of my life outside of research, and I made a lot of friends when playing soccer. I want to thank my international teammates in "Carotid Kidz" and

Chinese teammates in "Play For Fun", especially for those who assisted me to score lots of goals:). Among them, I want to specifically thank Baihong Jin and Shuyu Tang. They have been amazing close friends. We shared countless wonderful moments together and exchanged lots of great ideas and in-depth discussions about research, soccer, career and life. This means a lot to me. My research turned more statistics-related since the third year of my PhD, I am grateful to my friend Yuting Wei at statistics department for helping me go through the foundations of statistics and chatting about incorporating physical models into data-driven inference as a constrained optimization. I also want to thank Yuxun Zhou and Weixi Gu from EECS department for fruitful discussions on machine learning. Yuxun also gave me a lot of useful suggestions for my future career.

Last, but also most importantly, I would like to express my greatest gratitude to my parents. They are the ones who fostered a love of math and science in me. They encouraged me to patiently discover my hidden talents as I grew up, not give up when I faced a challenge and go out of my comfort zone when I aimed for bigger goals. All my achievement will not be possible without their unconditional love and support.

Chapter 1

Introduction

1.1 Vascular homeostasis

Cardiovascular disease is one of the leading causes of morbidity and mortality in the world; the progression of which is closely related to vascular adaptation in response to mechanical and chemical stimuli. The function of this vascular adaptive behavior is to maintain a preferred homeostasis against vascular stimuli [49]. Homeostasis reflects the state in which a normal vascular system operates. Failure to maintain vascular homeostasis can potentially leads to vascular diseases such as arterial aneurysm or stenosis [30, 18]. As a framework to better understand this adaptive behavior to the homeostatic state, a theory for vascular growth and remodeling (G&R) was proposed by Humphrey, et al., based on a constrained mixture model [75] in which the vessel wall adapts to mechanical stimuli and recovers a homeostatic state via smooth muscle cell synthesis and matrix turnover [117, 118]. Kinematic models of G&R have also been considered [111], where the time rates of change of the growth stretch ratios are assumed to linearly depend on the local smooth muscle stress and on vascular wall shear stress. The constrained mixture theory of G&R has been applied to study stress-mediated aneurysm expansion in idealized ellipsoidal and cylindrical geometry [13, 12] to better understand key factors influencing expansion rate and resulting aneurysm shape. Recently, G&R simulation has been extended to 3D geometries to predict the more complex case of asymmetric expansion [138]. In other works, [130] studied the role of collagen properties on AAA progression modeling, and [129] studied the influence of the initial state of the aorta on enlargement and mechanical behavior. Humphrey and Holzapfel [72] provided a review of the experimental data, computational models, mechanobiological factors, and open problems for G&R of human abdominal aortic aneurysm.

The vascular homeostatic state plays a key role in vascular adaptation and disease progression. From a modeling perspective, the vascular homeostatic state is the nominal initial state used when modeling the biomechanical behavior of vascular tissue. Usually, it is modeled as a known state with predefined wall structure and stress distribution. However, it is still an open question how the vascular homeostatic state should be defined and it is a

non-trivial task to computationally generate a proper homeostatic state that leads to realistic model behavior. Fung first mentioned in [49] that stress is uniform throughout the transmural directions in the homeostatic state. In [41, 138, 134], the homeostatic state is characterized by uniform stress throughout the geometry with predefined fiber orientations. [40] treats homeostasis as a mechanostat set point that is fixed to certain type of cells but may adapt to the environment.

To model the homeostatic state, two pieces of information need to be specified about the vascular homeostatic state: (a) the vessel wall structure, (b) the stress distribution. Arterial tissue is generally composed of three layers (intima, media, and adventitia) and the major mechanical constituents are elastin, collagen, and smooth muscle fibers [71]. Elastin is effective under small strain, while collagen bears the majority of loading when deformation is large [96], and smooth muscle fibers provide additional and vasoactive support [48]. To model these structural characteristics, different constitutive models have been proposed to describe the mechanical nature of arterial walls; examples include Fung-type models [26] and models based on constitutive relations proposed by Holzapfel et al. [61]. Notably, the arterial wall is often modeled as a two-layer fiber-reinforced material. A non-collagenous ground matrix, which includes elastin, is typically described as isotropic using a neo-Hookean strain energy function [35]. The collagen and smooth muscle fibers, which impart the anisotropic behavior of the vessel wall, are often described by a Fung-type exponential response [61] and [14]. Fiber orientations are prescribed from statistical analyses of histological data [60] or rule-based approaches [10], with more recent works [51] and [64] considering the additional dispersion of fiber orientation.

The total stress distribution in the homeostatic state is hypothesized to be uniform throughout each layer of the vessel wall. To maintain this condition, it is thought that non-uniform residual stress helps to homogenize the stress distribution within the tissue [49]. Therefore, incorporating residual stress is important to accurately modeling the *in vivo* state of a vessel and potential vascular remodeling [63]. In idealized cylindrical vascular geometries, the residual stress field is often specified based on an opening angle [2], however, this approach is often inadequate in more realistic vascular geometries. Pierce et al. [93] prescribed residual stress by specifying the deformation gradient mapping from a stress-free configuration to the actual mixture configuration of the vessel wall. Bellini et al. [14] incorporated a prestretch ratio into the total deformation to model the effect of residual stresses; in this study the authors also showed that the stress distribution within the tissue tends to be more uniform when residual stress is included. Holzapfel et al. investigated a 3D behavior of the residual stress experimentally [66] and developed a theoretical framework to incorporate residual stress in different vascular layers [63]. Previous works have often required parameter information that can be difficult to obtain or is of challenging applicability when complicated patient-specific geometries are considered. Likewise, the residual stress distribution has not been well considered when the vascular homeostatic state needs to be reconstructed in non-idealized geometries.

1.2 Bayesian data filtering methods

Computational models are pervasively used in cardiovascular modeling problems. Recent advances in computer platforms and numerical methods have enabled models to be increasingly sophisticated and comprehensive.With greater model complexity comes greater challenge to determine model parameters (including initial/boundary conditions), which are often unknown or uncertain. To address this challenge, one typically solves an *inverse problem* by using observational data to specify model parameters so that the model output matches the observational data. Many inversion techniques have been developed and used by different communities. These methods can be roughly categorized into two classes: variational and statistical approaches [9]. The variational approach aims to minimize a specific cost function based on classical optimization theory and calculus of variations [110], while the statistical approach aims to evaluate or maximize posterior functions based on statistics and Bayesian theory [27].

Because of its robustness and capability for uncertainty quantification, Bayesian inversion techniques are widely used for hidden state and parameter estimation for many physical systems [77, 126, 125, 83]. In the Bayesian framework, both the hidden state/parameters (prior) and observable quantities (likelihood) are described as random variables with statistical distributions. The Bayesian estimation aims to calculate the posterior distributions of the inferred quantities from the prior and likelihood based on Bayes theorem. Directly computing the posterior distribution based on the prior and likelihood functions is referred to as the exact Bayesian approach. In general, the posterior is obtained by sampling the prior and likelihood distributions based on efficient Monte Carlo sampling such as the Markov chain Monte Carlo (MCMC) method. However, since MCMC requires an enormous amount of samples, which is computationally infeasible when the likelihood calculation involves expensive model evaluations, many approximate Bayesian inversion approaches have been developed, such as the extended Kalman filter (EKF) [57], unscented Kalman filter (UKF) [123], ensemble Kalman filter (EnKF) [39], and sequential Monte Carlo (SMC) method [33].

The iterative ensemble Kalman filter (IEnKF) [76] was developed specifically to handle nonlinear inverse problems and leverage the computational efficiency of utilizing ensemble-based methods. However, despite its broad applicability, the IEnKF can suffer from poor convergence and stability. A major reason the IEnKF can fail to provide accurate estimation is due to a progressively diminished estimation (shrinking) of the covariance. This was initially addressed by including covariance "inflation" in the covariance updates [6]; however, tuning the inflation parameter can be inefficient. More recently, several adaptive covariance inflation methods have been proposed, which tune the inflation based on the innovation [4, 5, 17, 139, 136]. Similarly, [114] proposed an adaptive covariance inflation method where the inflation parameter depends on both the innovation and the covariance between the observed and unobserved components.

Another common challenge in solving inverse problems is identifiability. Measurement data is typically very limited and solutions for the hidden states and parameters are nonunique. Moreover, numerical stability of the inversion can be significantly reduced for ill-posed prob-

lems and uncontrolled inference may happen due to small random noise in the observation data. To address these issues, a general strategy is to incorporate additional information into the inversion process, either by including more observation data or imposing additional constraints. In most mission-critical applications, data are difficult to collect and limited in quality. In such cases, additional constraints can be significantly useful to help regularize the inversion results to consistent ranges and relieve ill-posedness. Fortunately, for many physical systems, constraints on the state and parameters are available based on existed knowledge [58]. Nonetheless, most existing Bayesian methods do not take constraints into account [106].

1.3 Thesis outline

The goal of this thesis is to better understand the vascular adaptive behavior around the homeostatic state and improve data filtering methods for physical models. Chapter 2 describes the theory of vascular G&R and homeostasis in terms constrained mixture theory [75], and develops a computational framework to couple vascular G&R, vessel wall mechanics and hemodynamics in patient-specific geometry applied to the problem of predicting aneurysm progression. Chapter 3 proposes a computational method to generate vascular homeostatic state by incorporating proper residual stress and optimal stress-driven fiber deposition. Chapter 4 conducts a theoretical analysis of the governing equations of vascular G&R around the homeostatic state for cylindrical geometries. A stability criterion is derived and the connection with predicting aneurysm rupture is established. Chapter 5 discusses about implementing IEnKF to solve nonlinear inverse problems and the underlying convergence issue of the standard IEnKF which is improved by a proposed ensemble resampling approach. Chapter 6 proposes a way to incorporate physical model information as prior to improve the convergence of parameter estimation in the case of multiple local minima when observation is insufficient.

Chapter 2

Coupled simulation of hemodynamics and vascular growth and remodeling

2.1 Introduction

In this chapter, we follow the basic framework of the constrained mixture theory for G&R described in [12, 120, 119]. Unlike previous works, we extend the formulation of coupling hemodynamics with vascular G&R to a realistic vascular model that includes branching and several arterial segments. This provides capability to consider more complete patient-specific geometries than previously considered, which is necessary to translate such modeling to many important clinical applications. The model used herein is derived from medical image data and vascular adaptation resulting from an idealized injury model is simulated. Blood flow is modeled as an incompressible, Newtonian fluid and simulated when G&R introduces significant geometric change. Hemodynamic forces are used to regulate G&R over longer time scales. In Sec. 2.2, we define the basic concepts, G&R kinetics, constitutive relations, hemodynamics and stress mediated growth laws. An algorithm for the coupled simulation is presented, which was implemented within a finite element framework using custom code and COMSOL as a generic FEM solver. In Sec. 2.3, we present simulations of different scenarios for abdominal aortic aneurysm expansion by varying initial mass loss. Coupled simulations are performed with different values of G&R feedback gains to demonstrate the influence of these constants on both the resulting aneurysm shape and hemodynamics.

2.2 Methods

2.2.1 Definitions

Vascular G&R is modeled by the theoretical framework proposed in [75]. The vessel wall is modeled as a membrane and treated as a constrained mixture, which implies that at each location the mixture (collagen + elastin + smooth muscle) deforms together. The reference

configuration will be denoted κ_0 for the mixture. This configuration corresponds to zero transmural pressure, $P = 0$, however, constituents in this configuration are not necessarily stress-free due to prestress. At any time t, the deformed configuration of the mixture is defined as $\kappa(t)$. The deformation gradient tensor $\mathbf{F}(t)$ maps $\kappa_0 \mapsto \kappa(t)$.

Collagen is assumed to be anisotropic and is characterized by discretized collagen families k, which have individual collagen fiber directions and reference configurations. Collagen can be incorporated into the mixture at intermediate times τ, with pre-stretch defined by tensor $\mathbf{G}^k(\tau)$. For each orientation k, $\mathbf{G}^k(\tau)$ maps the natural configuration of the newly produced collagen at time τ, denoted $\kappa^k_{n(\tau)}$, to the deformed configuration of the mixture at this time τ; subscript $n(\tau)$ denotes the natural configuration at time τ. For each collagen family, we define a deformation gradient tensor, which maps the natural configuration of that family to the current deformed mixture configuration, by

$$\mathbf{F}^k_{n(\tau)}(t) = \mathbf{F}(t)\mathbf{F}^{-1}(\tau)\mathbf{G}^k(\tau) \ , \tag{2.1}$$

hence, the right Cauchy-Green deformation tensor can be obtained as

$$\mathbf{C}^k_{n(\tau)}(t) = \mathbf{F}^k_{n(\tau)}(t)^\intercal \ \mathbf{F}^k_{n(\tau)}(t) \ . \tag{2.2}$$

These mappings and their compositions are shown schematically in Fig. 2.1.

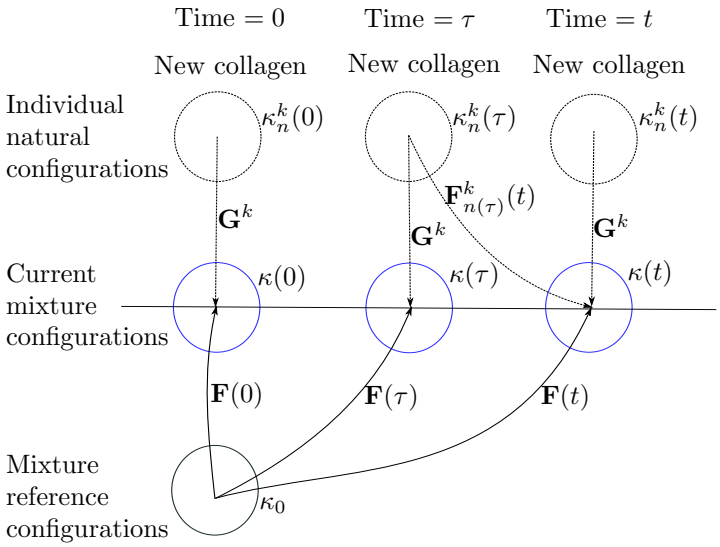

Figure 2.1: Configurations and associated mappings used to describe G&R framework.

The unit vector in the direction of collagen family k at time t is denoted $\mathbf{e}^k(t)$, and collagen fiber produced at time τ is assumed to be deposited in the $\mathbf{e}^k(\tau)$ direction, i.e., in the direction of existing collagen. Therefore, the direction of the collagen fiber produced at

time τ in its natural configuration, $\kappa^k_{n(\tau)}$, is described by the unit vector

$$\mathbf{e}^k_{n(\tau)} = \frac{\mathbf{G}^k(\tau)^{-1}\mathbf{e}^k(\tau)}{\|\mathbf{G}^k(\tau)^{-1}\mathbf{e}^k(\tau)\|} \ . \tag{2.3}$$

With $\mathbf{e}^k(\tau)$ and $\mathbf{e}^k_{n(\tau)}$, $\mathbf{G}^k(\tau)$ can be defined as a two-point tensor

$$\mathbf{G}^k(\tau) = G^k \ \mathbf{e}^k(\tau) \otimes \mathbf{e}^k_{n(\tau)} \ , \tag{2.4}$$

where G^k is the stretch ratio of newly produced collagen fiber from the natural configuration $\kappa^k_{n(\tau)}$ to the mixture configuration κ_τ. We assume G^k does not depends on collagen family k and is equal to the homeostatic collagen stretch ratio G^c_h, set herein to 1.05; subscript h denotes the homeostatic state. The stretch ratio G^k can be obtained as

$$\begin{aligned}
\lambda^k_{n(\tau)}(t) &= \sqrt{\mathbf{e}^k_{n(\tau)} \cdot \mathbf{C}^k_{n(\tau)}(t)\mathbf{e}^k_{n(\tau)}} \\
&= \left\|\mathbf{F}(t)\mathbf{F}^{-1}(\tau)\mathbf{G}^k(\tau)\mathbf{e}^k_{n(\tau)}\right\| \\
&= \left\|\mathbf{F}(t)\mathbf{F}^{-1}(\tau)G^c_h\left(\mathbf{e}^k(\tau)\otimes\mathbf{e}^k_{n(\tau)}\right)\mathbf{e}^k_{n(\tau)}\right\| \\
&= G^c_h\left\|\mathbf{F}(t)\mathbf{F}^{-1}(\tau)\mathbf{e}^k(\tau)\right\| \\
&= G^c_h\frac{\left\|\mathbf{F}(t)\mathbf{F}^{-1}(\tau)\mathbf{e}^k(\tau)\right\| / \left\|\mathbf{F}^{-1}(\tau)\mathbf{e}^k(\tau)\right\|}{\|\mathbf{e}^k(\tau)\| / \|\mathbf{F}^{-1}(\tau)\mathbf{e}^k(\tau)\|} \\
&= G^c_h\frac{\lambda^k(t)}{\lambda^k(\tau)} \ ,
\end{aligned} \tag{2.5}$$

where $\lambda^k(t)$ is the stretch ratio of the mixture in the direction of collagen family k, defined as

$$\lambda^k(t) = \frac{\left\|\mathbf{F}(t)\mathbf{F}^{-1}(\tau)\mathbf{e}^k(\tau)\right\|}{\|\mathbf{F}^{-1}(\tau)\mathbf{e}^k(\tau)\|} \ . \tag{2.6}$$

For elastin, we assume the mapping from the natural configuration to the mixture reference configuration is $\mathbf{G^e}$, and therefore the mapping from elastin's natural configuration to the current mixture configuration is given by

$$\mathbf{F}^e_n(t) = \mathbf{F}(t)\mathbf{G}^e \ . \tag{2.7}$$

In this model we take $\mathbf{G^e} = \mathrm{diag}[G^e_1, G^e_2, \frac{1}{G^e_1 G^e_2}]$, which assumes the prestretch occurs in the principal directions of the existing mixture, where the third component has been written in terms of the prior two by imposing incompressibility.

2.2.2 Kinetics of growth & remodeling

The vessel wall has ability to adapt in response to mechanical stimuli in order to recover a homeostatic state. This process occurs by both the removal of old constituents, and

incorporation of new constituents into the mixture due to natural turnover as well as stress-mediated growth. Let $M^k(t)$ be the mass per unit area of each collagen family k, and the time evolution of $M^k(t)$ is described by

$$M^k(t) = M^k(0)Q^k(t) + \int_0^t m^k(\tau)q^k(t-\tau)d\tau \ . \tag{2.8}$$

The first term on the right of the equation describes natural turnover of the initial mass produced before the G&R process. The second term describes the incorporation and natural turnover of the newly produced constituent. $Q^k(t)$ is the remaining fraction at time t for the kth collagen family produced at time 0. $m^k(\tau)$ is the mass production rate of the kth collagen family at time τ and $q^k(t-\tau)$ is the remaining fraction at time t.

For elastin,

$$M^e(t) = M^e(0)Q^e(t), \tag{2.9}$$

where $Q^e(t)$ is the corresponding remaining fraction of initial mass for elastin at time t. Since functional elastin is thought to be mainly produced during early development, there is no second term for newly produced elastin in (2.9), as there was for collagen in (2.8).

The remaining fraction for collagen family k is assumed to have the following form [41]

$$q^k(t) = \begin{cases} 1, & \text{if } 0 \le t < t_1 \\ \frac{1}{2}\left\{\cos\left(\frac{\pi}{t_2-t_1}(t-t_1)\right)+1\right\}, & \text{if } t_1 \le t \le t_2 \\ 0, & \text{if } t_2 < t \ , \end{cases} \tag{2.10}$$

where t_2 is the lifespan of the constituent. For collagen we use $t_1/t_2 = 0.2$, and $t_2 = 1$. Hence, time herein is normalized by the lifespan of collagen, which is generally between 70–80 days [130, 87]. The function representing the remaining fraction at time t of the initial mass is given by

$$Q^k(t) = 1 - \frac{\int_0^t q^k(\tau)d\tau}{\int_0^{t_2} q^k(\tau)d\tau} = 1 - \frac{2\int_0^t q^k(\tau)d\tau}{t_1+t_2} \ . \tag{2.11}$$

2.2.3 Constitutive relations

Collagen was assumed to follow a Fung-type exponential constitutive relation. The strain energy per unit mass of the kth family of collagen is

$$W^k\left(I^k_{n(\tau)}\right) = \frac{c_2}{4c_3}\left\{\exp\left[c_3\left(I^k_{n(\tau)}-1\right)^2\right]-1\right\} \ , \tag{2.12}$$

where

$$I^k_{n(\tau)} = \left(\lambda^k_{n(\tau)}(t)\right)^2 \ . \tag{2.13}$$

Let

$$\mathbf{C}^k_{n(\tau)}(t) = \mathbf{F}^k_{n(\tau)}(t)^\intercal \, \mathbf{F}^k_{n(\tau)}(t) \tag{2.14}$$

denote the right Cauchy-Green deformation tensor of the kth family of collagen produced at time τ, whose current direction is denoted by $\mathbf{e}^k(t)$, with respect to its natural configuration. The subscript $n(\tau)$ denotes the natural configuration of the constituent produced at time τ. For elastin, the strain energy function is defined based on a Neo-Hookean behavior,

$$W^e(\mathbf{C}_n^e(t)) = \frac{c_1}{2}\left(I_1 - 3\right), \tag{2.15}$$

where

$$I_1(t) = \mathrm{tr}(\mathbf{C}_n^e(t)). \tag{2.16}$$

$\mathbf{C}_n^e(t) = \mathbf{F}_n^e(t)^\intercal\, \mathbf{F}_n^e(t)$ is the right Cauchy-Green deformation tensor of elastin with respect to its nature configuration.

Based on the mass-averaged principle for a constrained mixture, the total strain energy per unit area for all constituents at time t is

$$\begin{aligned} w(t) =&\ w^e(t) + \sum_k w^k(t) \\ =&\ M^e(0)Q^e(t)W^e(\mathbf{C}_n^e(t)) \\ &+ \sum_k \left\{ M^k(0)Q^k(t)W^k\left(I^k_{n(0)}\right) + \int_0^t m^k(\tau)q^k(t-\tau)W^k\left(I^k_{n(\tau)}\right) \right\} \end{aligned} \tag{2.17}$$

where $w^e(t)$ and $w^k(t)$ denote the total strain energy contributed by elastin and the kth collagen family, respectively. We do not directly model the passive response of smooth muscle due to the fact that smooth muscle is much more compliant than collagen and thus has minimal contribution to the passive mechanical behavior of the vessel wall [22]. However the active response of smooth muscle does play an important role in vascular adaptation to altered flow. It is important to note that the strain energy function depends on both the current state and the history of deformation. Once the mathematical form of the total strain energy function is formulated, the deformation of the vessel wall can be obtained from the virtual work principle

$$\delta I = \int_S \delta w\, dA - \int_s P\, \mathbf{n}\cdot\delta\mathbf{x}\, da = 0\ , \tag{2.18}$$

where P is the vascular transmural pressure, $\mathbf{n}$ is the normal vector on vessel wall surface and $\delta\mathbf{x}$ is the virtual displacement of the vessel wall. S and s denote the surface area of vessel wall in the reference and current configuration, respectively.

2.2.4 Defining local anisotropic material property

One of the challenges in implementing growth and remodeling in 3D patient specific geometry is to define local anisotropic material properties, i.e., to define the local directions for collagen families. Usually local collagen directions $\mathbf{e}_0^k$ are defined with respect to local

circumferential and axial directions in the reference configuration, and later evolve with the mixture deformation $\mathbf{F}(t)$. Therefore, the current collagen directions $\mathbf{e}^k(t)$ are defined as

$$\mathbf{e}^k(t) = \mathbf{F}(t)\mathbf{e}_0^k \ . \tag{2.19}$$

Note that normalization is needed to obtain unit direction.

In idealized geometries, circumferential and axial directions can be readily defined (see [13, 12]), but defining these directions in 3D patient specific geometry is nontrivial. In [137], the authors defined the local circumferential and axial directions based on a 2-D parameterization of the vessel wall surface. However, it is not obvious how to apply this approach to a geometry with multiple outlets or bifurcations. In the work herein, local circumferential and axial directions are defined using local principal curvature directions, from which, local collagen directions are then calculated. As long as the geometry is smooth enough (which is usually the case), principal curvature directions are everywhere well-defined.

2.2.5 Hemodynamics

Blood was modeled as an incompressible, Newtonian fluid described by the Navier-Stokes and continuity equation

$$\rho_b \left(\frac{\partial \mathbf{v}(\mathbf{x}, t)}{\partial t} + \mathbf{v}(\mathbf{x}, \mathbf{t}) \cdot \nabla \mathbf{v}(\mathbf{x}, \mathbf{t}) \right) = -\nabla p(\mathbf{x}, t) + \mu \nabla^2 \mathbf{v}(\mathbf{x}, \mathbf{t}) \ , \tag{2.20}$$

$$\nabla \cdot \mathbf{v}(\mathbf{x}, \mathbf{t}) = 0 \ . \tag{2.21}$$

The blood density ρ_b and viscosity μ were set to 1.05 g/cm^3 and 0.035 Poise. A no-slip, no-penetration boundary condition was specified along lumen surface of the fluid domain, and a velocity profile (Dirichlet boundary condition) was specified at the inlet plane. At the outflow surfaces, Neumann-type boundary conditions were specified by coupling resistive models of the downstream vascular beds. Namely, the pressure $P_0(t)$ at each outflow boundary was solved as

$$P_o(t) = R\, Q_o(t) \tag{2.22}$$

The flow rate Q_o at the respective outlets was obtained from the 3D domain, and using Eq. (2.22) the pressure P_o at the outlet was computed and applied at the zero traction outlet faces as Neumman boundary conditions. Details of the FEM implementation of the boundary conditions can be found in [36].

It is important to note that the time scales for G&R ($\lesssim$weeks) and blood flow simulation ($\lesssim$second) are several orders of magnitude different. A fully-coupled simulation of both processes is neither efficient nor necessary, because the hemodynamics stresses imparted from the blood flow do not change significantly until usually several weeks of geometric change has occurred through G&R. Nominally, blood flow was simulated when G&R caused changes to the boundary of the fluid domain, and for all times in between, the values for WSS and pressure were well approximated by the values from the last blood flow simulation.

Specifically, it was assumed that mesh quality was an appropriate measure to monitor vessel deformation and the need for computing a new Navier-Stokes solution. This is (at least) consistent with the fact that the numerical accuracy of the Navier-Stokes solution, and hence WSS, depends on mesh quality.

2.2.6 Stress-mediated growth & remodeling

Here we describe how vascular adaptation is regulated by wall tension and WSS. Once the deformation is obtained by solving the variational equation (2.18), the Cauchy stress tensor is obtained as

$$\begin{aligned}\mathbf{T}(t) &= \frac{1}{J(t)}\mathbf{F}(t)\frac{\partial w}{\partial I_1(t)}\frac{\partial I_1(t)}{\partial \mathbf{F}(t)} + \frac{1}{J(t)}\mathbf{F}(t)\sum_k \frac{\partial w}{\partial I^k_{n(\tau)}(t)}\frac{\partial I^k_{n(\tau)}(t)}{\partial \mathbf{F}(t)} + \mathbf{T}_{\text{active}} \\ &= \frac{2}{J(t)}\frac{\partial w^e}{\partial I_1(t)}\mathbf{B}(t) + \frac{2}{J(t)}\sum_k \frac{\partial w^k}{\partial I^k_{n(\tau)}}\frac{\partial I^k_{n(\tau)}}{\partial I^k(t)}\mathbf{e}^k \otimes \mathbf{e}^k + \mathbf{T}_{\text{active}}, \end{aligned} \tag{2.23}$$

where $\mathbf{B} = \mathbf{F}\mathbf{F}^{\mathsf{T}}$ is the left Cauchy-Green deformation tensor, and $J(t)$ is the determinant of the deformation gradient tensor $\mathbf{F}(t)$. The first term on the right hand side denotes the stress contribution of elastin and the second term denotes that of two collagen families. The last term $\mathbf{T}_{\text{active}}$ denotes the active membrane stress due to active smooth muscle contraction and relaxation. However, to keep the model simple and computation tractable, we do not include this active response term in our later simulations. A scalar measure is obtained from the Cauchy stress tensor in the direction of collagen family k as

$$\sigma^k = \frac{\mathbf{e}^k \cdot \mathbf{T}\mathbf{e}^k}{h}, \tag{2.24}$$

which is the stress in the $\mathbf{e}^k$ direction. The thickness of the vessel wall was calculated as

$$h(t) = \frac{M(t)}{J\rho}\,, \tag{2.25}$$

where $M(t) = \sum_k M^k(t)$ is the total collagen mass and ρ denotes the volume density of collagen.

In G&R theory, the vascular homeostatic state is recovered through stress-mediated feedback. The mass production rate of the kth family of collagen is assumed to depend linearly on the deviation of wall tension σ^k with respect to the homeostatic value σ^h. In addition, WSS regulation may be active via interactions between vascular endothelium and blood flow. It is well-known that endothelial cells can release multiple vasoactive chemicals in response to altered WSS. These chemicals can affect smooth muscle cell proliferation and collagen turnover. For instance, nitric oxide (NO) is a potential inhibitor of synthesis of collagen and smooth muscle proliferation [94], while endothelin-1 (ET-1) is a promoter of synthesis of collagen and smooth muscle proliferation [95]. NO is up-regulated in response to increased

WSS [115] and ET-1 is up-regulated by decreased WSS [86]. These factors make WSS regulation uncertain. Due to lack of further information, we naively assume mass production rate of collagen is proportional to the deviation of wall shear stress τ_w from the preferred state τ_w^h and consider cases of both positive and negative feedback. Thus the complete stress mediated growth law is given by

$$m^k(t) = \frac{M(t)}{M(0)} \left(K_\sigma \left(\sigma^k(t) - \sigma^h \right) - K_\tau \left(\tau_w(t) - \tau_w^h \right) + \tilde{f_h^k} \right) , \tag{2.26}$$

where $\tilde{f_h^k}$ is the basal value of mass production rate for collagen family k,

$$\tilde{f_h^k} = \frac{M^k(0)}{\int_0^\infty q^k(\tau) d\tau} , \tag{2.27}$$

which balances the degradation rate of collagen in the homeostatic state. Note that $\tau_w(t)$ in (2.26) is given directly by the blood flow simulation, whereas σ^k depends on transmural pressure. K_σ and K_τ are feedback gains for the deviations of wall tension and wall shear stress. For $K_\sigma > 0$, if $\sigma^k(t) > \sigma^h$, the mass production rate $m^k(t)$ will increase, and in turn, cause an increase in wall thickness $h(t)$. The thickening of the vessel wall will decrease the vessel radius for the same transmural pressure. Based on Laplace's law for a cylinder, $\sigma = \frac{Pr}{h}$, and we can postulate that σ^k will hence decrease and return back to the homeostatic value. This means that for $K_\sigma > 0$, the growth law (2.26) initiates a negative feedback mechanism. Using similar arguments for wall shear stress based on simple Poiseuille flow, $\tau = \frac{4\eta Q}{\pi r^3}$, we can postulate that a decreased vessel radius will increase WSS, so that $K_\tau > 0$ also initiates a negative feedback mechanism for wall shear stress deviation. Therefore, if K_σ and K_τ are large enough, the stress will converge to the corresponding homeostatic value.

2.3 Results

In this section we apply G&R simulation to a vascular model of the aorta whose lumen morphology is derived from medical image data. The model is a truncated section of an aortofemeral model (ID: OSMSC0006) publicly available on vascularmodel.org [131]. After initialization of the model, scenarios for G&R are considered by introducing mass loss at various locations to simulate the development of abdominal aortic aneurysm. Material constants used in the simulations are listed in Table 2.1. In the following results, two main helical collagen directions (45° and 135° from the axial direction) are included in the simulations. This is consistent with prior observations that close to 90% of the total mass of collagen is distributed in these helical directions [62], although this does not hold universally true and additional families or orientations could be considered. Fig. 2.2 displays the fiber orientation about the aortic bifurcation region. It is observed that the collagen directions in both families naturally become aligned about the apical ridge at the bifurcation, which is consistent with the simulation results in [56] and consistent with experimental findings in [45].

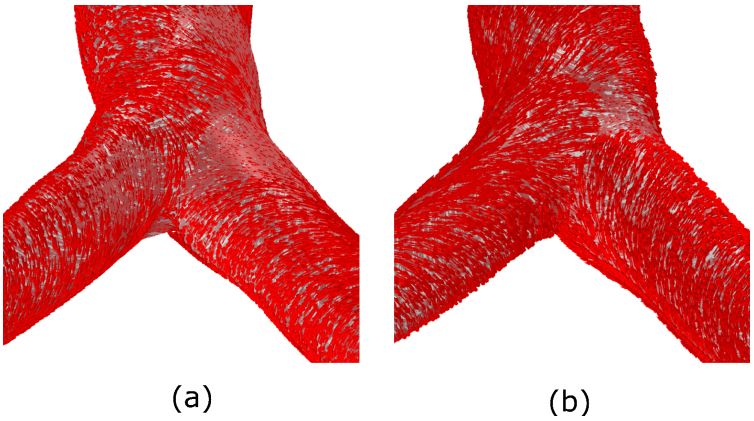

Figure 2.2: Local collagen directions calculated based on principal curvature directions at the aortic bifurcation: (a) 45° collagen family, (b) 135° collagen family.

Table 2.1: Material constants for elastin and collagen [138, 52]

Elastin:	$c_1 = 112$ Pa/kg	$G_1^e = 1.25$	$G_2^e = 1.25$
Collagen:	$c_2 = 917$ Pa/kg	$c_3 = 25$	$G_h^c = 1.05$

2.3.1 Generation of initial homeostatic configuration

In the G&R theory, the healthy vessel wall is assumed to be in the homeostatic state, i.e., the stress of each constituent is equal to the homeostatic value, and therefore no significant growth and remodeling is induced beyond the basal production and turnover rate. Recall that a membrane model is used for the vessel wall. The vascular geometry derived from the medical image data is irregular, and therefore achieving an initial homeostatic stress state requires specifying an appropriately varying mass distribution of the constituents. This can be accomplished by an initial G&R stage to solve for an appropriate homeostatic mass distribution, as proposed in [138]. Namely, an accelerated G&R stage is simulated using a feedback gain for wall tension, K_σ, set to 0.005. This enabled the mass distribution to converge (approximately) to the homeostatic state without significantly altering the overall geometry.

In Fig. 2.3(a)(b), and 2.3(c)(d), the deviation of stress relative to the homeostatic values for the 45°, and 135°, respectively, oriented collagen family are plotted before and after the initial homeostatic simulation. Wall tension distributions become mostly uniform after the initial homeostatic simulation, with stress values in both directions generally within the range of $0.9\sigma^h$ to $1.1\sigma^h$. This initial homeostatic simulation ensured that subsequent G&R would be induced almost entirely at the location(s) where mass loss is introduced–that is, the modeled site(s) of injury.

While convergence of wall tension σ to homeostatic value can be obtained via adjustment of geometry or mass density distribution, convergence of wall shear stress τ_w can only be obtained through adjustment of vascular geometry. Because the initial homeostatic simulation

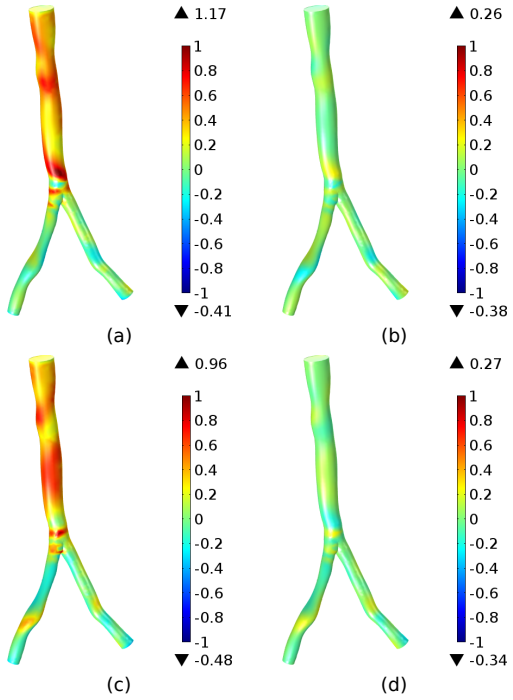

Figure 2.3: Deviation of stress relative to homeostatic stress $\left(\sigma^k - \sigma_h\right)/\sigma_h$ before (left) and after (right) 14 time steps of "accelerated" G&R simulation for the 45°(a)(b) and 135°(c)(d) collagen families. Each time step represents 1/10 of collagen lifespan.

should not introduce large geometric change, i.e., the original geometry should be maintained, wall shear stress regulation was not included in the initial homeostatic simulation.

2.3.2 Simulation for aneurysm expansion

An interesting application of the coupled G&R framework is to simulate aneurysm expansion in a region of vascular damage. Aneurysm expansion can be induced through constituent mass loss at specific locations, coupled with sufficiently low mass production rate of vascular constituents. Initial mass loss was introduced for the following three scenarios:

(1) Banded mass loss distribution

$$M^k(\mathbf{x},0) = \begin{cases} M_h^k(\mathbf{x})\left(1 - 0.5 f_{mr}\left(\cos\left(\frac{\pi(z-z_0)}{2R_0}\right)+1\right)\right), & z_0 - 2R_0 \le z \le z_0 + 2R_0, \\ M_h^k(\mathbf{x}), & \text{else .} \end{cases}$$

(2) Point mass loss distribution

$$M^k(\mathbf{x},0)=\begin{cases} M_h^k(\mathbf{x})\left(1-f_{mr}\right), & |\mathbf{x}-\mathbf{x_c}|\le R_0,\\ M_h^k(\mathbf{x})\left(1-f_{mr}\left(\frac{2R_0-|\mathbf{x}-\mathbf{x_c}|}{R_0}\right)\right), & R_0<|\mathbf{x}-\mathbf{x_c}|\le 2R_0,\\ M_h^k(\mathbf{x}), & \text{else.}\end{cases}$$

(3) Multiple point mass loss distribution

$$M^k(\mathbf{x},0)=\begin{cases} M_h^k(\mathbf{x})\left(1-f_{mr}\right), & |\mathbf{x}-\mathbf{x_{c1}}|\le 0.5R_0,\\ M_h^k(\mathbf{x})\left(1-f_{mr}\left(\frac{R_0-|\mathbf{x}-\mathbf{x_{c1}}|}{0.5R_0}\right)\right), & 0.5R_0<|\mathbf{x}-\mathbf{x_{c1}}|\le R_0,\\ M_h^k(\mathbf{x})\left(1-f_{mr}\right), & |\mathbf{x}-\mathbf{x_{c2}}|\le 0.5R_0,\\ M_h^k(\mathbf{x})\left(1-f_{mr}\left(\frac{R_0-|\mathbf{x}-\mathbf{x_{c2}}|}{0.5R_0}\right)\right), & 0.5R_0<|\mathbf{x}-\mathbf{x_{c2}}|\le R_0,\\ M_h^k(\mathbf{x}), & \text{else.}\end{cases}$$

$M_h^k(\mathbf{x})$ is the mass density generated by the initial homeostatic simulation. f_{mr} is the maximum mass loss percentage set herein to 50%. R_0 is the nominal value of the radius of the abdominal aorta, which was equal to 0.75 cm.

Figures 2.4(a)(b), 2.4(c)(d), and 2.4(e)(f) display the different initial mass loss distributions, along with the resulting vascular geometries after 110 G&R steps assuming $K_\sigma = 0$. (Below, we consider nontrivial values for K_σ.) Each G&R step was set to 0.1 of the collagen lifespan, so that 110 steps is equivalent to ≈800 days, assuming collagen has a life span around 72 days. It can be observed that significant expansion is only induced within or near the region of initial mass loss while the homeostatic state is effectively maintained in all other regions.

COMSOL was used to solve the Navier Stokes equations. For illustrative purpose, a steady inflow was used with a resting infrarenal abdominal aortic flow rate equal to 15.2 cc/s. This approach considered time-averaged flow conditions since we are interested in the affect of the flow over time scales much longer than the cardiac cycle. Alternatively, we could apply a pulsatile inflow boundary condition and then perform time-averaging of the resulting wall shear stress and pressure fields. The outlets of the 3D fluid domain were at the level of the iliac arteries. To set the resistance values for each outlet, an equivalent resistance was first computed so that the mean pressure was 100 mmHg. This resistance was then distributed in parallel to the iliac arteries, resulting in $R = 1.8269 \times 10^9$ Pa·s/m^3, and $R = 1.8285 \times 10^9$ Pa·s/m^3, for the left and right iliac, respectively.

To explore the importance of feedback gains on vascular growth in our coupled framework, different values were considered for K_τ and K_σ. These results are summarized in Fig. 2.6, where the point mass loss shown in Fig. 2.4(c) was used to trigger G&R in all cases. All panels in this figure represent the respective field and geometry at the end of 110 G&R steps. Namely, columns are ordered by increasing expansion resulting from feedback gain choice (not evolution in time). The first column considers relatively large feedback gains: $K_\tau = 0.005$

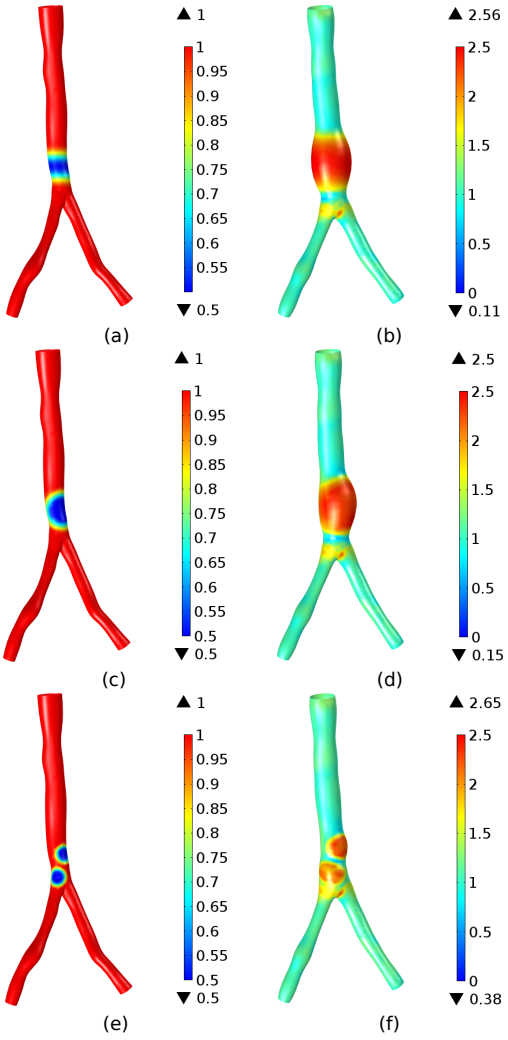

Figure 2.4: Initial mass loss distribution(ratio between current and homeostatic mass density) and resulting aneurysm shapes(color denotes values of det($\mathbf{F}$)) after 110 G&R steps. Correspondence relations: (a)→(b), (c)→(d), (e)→(f)

and $K_\sigma = 0.005$. In this case, the gains are large enough that even with the introduction of significant mass loss, expansion can be strongly suppressed through appropriate increase in wall thickness (mass density). After the 110 G&R steps, stress in both collagen constituents converged to the homeostatic value $\sigma_h = 133$kPa (see Fig. 2.5), and collagen turnover did not introduce any significant expansion.

We next considered four WSS feedback gains $K_\tau = 0.005, 0, -0.005, -0.01$, whose results are respectively shown in columns 2–5 of Fig. 2.6. In each of these cases, we set $K_\sigma = 0$ to isolate the influence of WSS regulation on aneurysm progression, aortic pressure and blood flow. (Note that the case $K_\sigma \neq 0$ and $K_\tau = 0$ was considered previously in Fig. 2.4.) It can be observed that $K_\tau > 0$ (corresponding to negative feedback) led to the lowest rate of

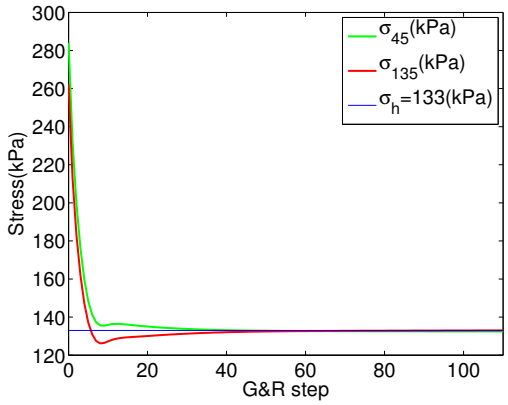

Figure 2.5: Convergence of constituent stress $K_\tau = 0.005$, $K_\sigma = 0.005$ at the location of largest mass loss $\mathbf{x} = \mathbf{x_c}$

expansion (Fig. 2.6, column 2). Positive feedback (corresponding to $K_\tau < 0$) produced the most rapid expansion (Fig. 2.6, column 4 & 5). In all cases, it can be observed that WSS changed by roughly one order of magnitude within the aneurysm region, which contributed to G&R, whereas the change in transmural pressure varied very little (less than 0.1%).

It can be observed from Fig. 2.6 that both positive and negative values for K_τ led to expansion. Note that in the absence of any feedback ($K_\sigma, K_\tau = 0$, Fig. 2.6, column 3), expansion occurs due to the normal turnover of collagen. Namely, the initial insult leads to immediate stretching of the existing collagen so that wall tension balances transmural pressure. This collagen is in an elevated stress state. Natural turnover of collagen produces new collagen whose prestress is lower than this elevated stress state, which causes these new fibers to stretch. This process drives a "basal expansion" due to the insult and natural collagen turnover. $K_\tau > 0$ helps to suppress this basal expansion (column 2), whereas $K_\tau < 0$ contributes to further expansion (columns 4, 5).

2.4 Discussion

We have presented a framework for coupling vascular growth and remodeling with blood flow simulation in a 3D patient-specific geometry using a constrained mixture theory for the vessel wall. Prior computational models [41, 107], coupling blood flow with G&R simulation have been applied to idealized geometry, or to a cylindrical segment of realistic geometry. Vascular G&R intrinsically occurs in all regions, and the purpose of this work was to develop coupled simulation of G&R with blood flow in a more complete and anatomically realistic vascular model than had previously been considered.

One difficulty in applying G&R simulations to complex vascular domains derived from medical image data is defining appropriate initial conditions. When starting from a healthy model, it is reasonable to assume an initial homeostatic configuration. We demonstrated,

as similarly shown in [41, 138] that an accelerated G&R stage can be performed to produce an approximate homeostatic configuration without significant geometrical alteration. As shown in Fig. 2.3, the relative stress deviation was nontrivial (>10%) in some regions after the initial accelerated G&R stage. The rate of convergence of the stress to the homeostatic value is proportional to the deviation. Therefore relatively long simulations times are needed to obtain very small deviations, whereas herein a relatively modest number of G&R steps were used. Indeed, our later simulation for $K_\sigma = 0.005, K_\tau = 0.005$ verified that stresses do eventually converge to very near the homeostatic values after 110 G&R steps. Moreover, our simulations (Fig. 2.6) also show that the initial nontrivial deviations in stress from the homeostatic values do not result in significant unbalanced G&R for the time scales considered herein, and that significant expansion is almost entirely induced near or within the region where mass loss is introduced. Regardless, it might be more natural in future implementations to apply a homeostatic range instead of specifying a single homeostatic value.

Another challenge of applying G&R to complex vascular domains is consistently defining local axial and circumferential directions, with respect to which local anisotropic material properties are defined. In [137] this was addressed by defining local axial and circumferential directions using a 2-D parameterization of the vessel wall surface. However, such parameterization cannot be defined for domains that include multiple/branching vessels. To overcome this issue herein, local principal curvature directions on the surfaces were used to represent local axial and circumferential directions. Initial collagen directions (45° and 135°) were defined with respect to axial and circumferential directions in the reference configuration κ_0 and later evolve with the mixture deformation.

In several prior coupled G&R modeling studies, aneurysm progression is triggered by prescribing initial insult as in [41]. Time dependent insult models have also been used [127] whereby AAA formation is initiated by prescribing a spatial and temporal degradation function for elastin. In more recent papers [128, 7, 105, 107], elastin degradation has been coupled to hemodynamics (mainly WSS) in order to initiate aneurysm progression. Herein, we used a simple insult model to trigger aneurysm progress since our focus was on application of coupled simulation to patient-specific geometry. However, more sophisticated initiation processes can be incorporated in this framework when applied to specific clinical applications.

In the coupled simulations with blood flow, the influence of G&R feedback gains K_σ and K_τ on the resulting aneurysm geometry and hemodynamics were studied. For large values of $K_\sigma = 0.005$ and $K_\tau = 0.005$ (column 1, Fig. 2.6), growth and remodeling can compensate for relatively large initial mass loss so that the resulting geometry changed very little. Fig. 2.5 shows the convergence of the stress $\sigma^k(t)$ to the homeostatic value σ_h at the center of mass loss, $\mathbf{x_c}$. We note that $\mathbf{x_c}$ is the location of largest mass loss and generally corresponds to largest deformation; hence recovery of σ^k at $\mathbf{x_c}$ generally indicates the convergence of stress in entire geometry.

We set $K_\sigma = 0$ to promote aneurysm expansion and then varied the value of K_τ to study the influence of the coupling with WSS regulation on the aneurysm progression. The role of WSS in aneurysm progression is complex and not well understood, therefore we considered

cases for K_τ being positive, negative and zero. Indeed, prior publications have considered K_τ positive [118] and negative [41]. Mass loss will necessarily lead to some expansion when $K_\sigma = 0$. However, $K_\tau > 0$ will compensate and reduce expansion rate due to the induced negative feedback. And conversely, expansion was exaggerated when $K_\tau < 0$ due to the induced positive feedback.

The WSS plots in Fig. 2.6 show that the magnitude of WSS is very low in the aneurysm region (less than 0.05Pa), consistent with reported values in AAA [99]. We note that even for $K_\tau > 0$ WSS does not converge to the homeostatic value. This may be because WSS regulation was turned off during the initial accelerated G&R stage or due to the fact that WSS is more sensitive to vascular geometry and hence more difficult to converge. Lastly, we note that it was verified that setting $K_\tau = 0$ led to identical expansion to a case that did not consider coupling with fluid dynamics. From the pressure plots in Fig. 2.6, it can be observed that pressure change within the 3-D computational domain is small (less than 0.5%), and pressure changes even less at each location between the cases considered. Therefore, it may be reasonable to apply a uniform pressure for all cases instead of explicit coupling the pressure information from the fluid simulation.

The choice of material parameters describing the passive vascular response given in Table 2.1 were obtained from [138]. These parameters are based on a phenomenological model, which may included smooth muscle. Applying these parameters in the model herein, which neglects the passive response due to smooth muscle, may introduce additional uncertainty to these parameters. However, because smooth muscle is at least an order of magnitude less stiff than collagen, its contribution to the passive stress-strain behavior is expected to be small. Hence, we do not anticipate that such additional uncertainty in parameters will be significant, especially in comparison to the inherent uncertainty in these parameters.

2.5 Conclusions

Herein a computational framework to couple vascular growth and remodeling with blood flow simulation in a 3D patient-specific geometry was presented. We demonstrated that stress mediated regulation of wall tension and wall shear stress led to expected long-term response in vessel wall progression following mass loss for different feedback parameters. These results extend prior computational work on coupling G&R with hemodynamics simulation to more complex, subject-specific setting. Additionally, by coupling the time scales of hemodynamics and G&R simulation we are able to better understand the connections between local, short term hemodynamic factors and long term vascular change. Indeed, most image-based blood flow modeling has been concerned with understanding hemodynamic phenomena occurring on the time scale of the cardiac cycle for diagnosing current flow conditions. However, there is compelling need to develop simulation capabilities to predict blood flow conditions and vascular adaption over time scales of months to years, which is difficult, or impossible, to consider experimentally. This framework helps to bridge this gap.

Appendix

Algorithm for coupled simulation of G&R and hemodynamics

(1) Generate initial homeostatic state through accelerated G&R.

(2) a) Introduce initial mass loss to the homeostatic state.
b) Simulate blood flow in the initial geometry and obtain initial WSS field $\tau_w(\mathbf{x}, t)$.
c) Set initial values for mass production rate $m_i \rightarrow m^k(t)$.

(3) Formulate the weak form for displacement $\mathbf{u} = (u, v, w)$ from the virtual work principle,

$$\delta I = \int_S \delta w dA - \int_s P\mathbf{n} \cdot \delta\mathbf{x} da = 0 \ ,$$

and solve using a nonlinear FEM solver.

(4) a) Generate stress measure field $\sigma^k(\mathbf{x}, t)$ based on deformation and constitutive relations
b) Update mass production rate:

$$m^k(t) = \frac{M(t)}{M(0)} \left(K_\sigma \left(\sigma^k(t) - \sigma^h \right) - K_\tau \left(\tau_w(t) - \tau_w^h \right) + \tilde{f}_h \right)$$

(5) If $\left\| m^k(t) - m_i \right\| / \left\| m_i \right\| <$ tolerance (in this work, tolerance= 0.001),
a) Set $m_i \leftarrow m^k(t)$
b) Set $t \leftarrow t + \Delta t$
c) Update values for remaining fractions $Q^k(\cdot)$ and $q^k(\cdot)$
d) Go to Step (6)

Else,
a) Set $m_i \leftarrow m^k(t)$
b) Go to Step (3)

(6) If the geometric change is significant for fluid domain,
a) Solve blood flow in the new geometry
b) Update WSS field $\tau_w(\mathbf{x}, t)$ and pressure $P(\mathbf{x}, t)$
c) Go to Step (3)

Else, go to Step (3)

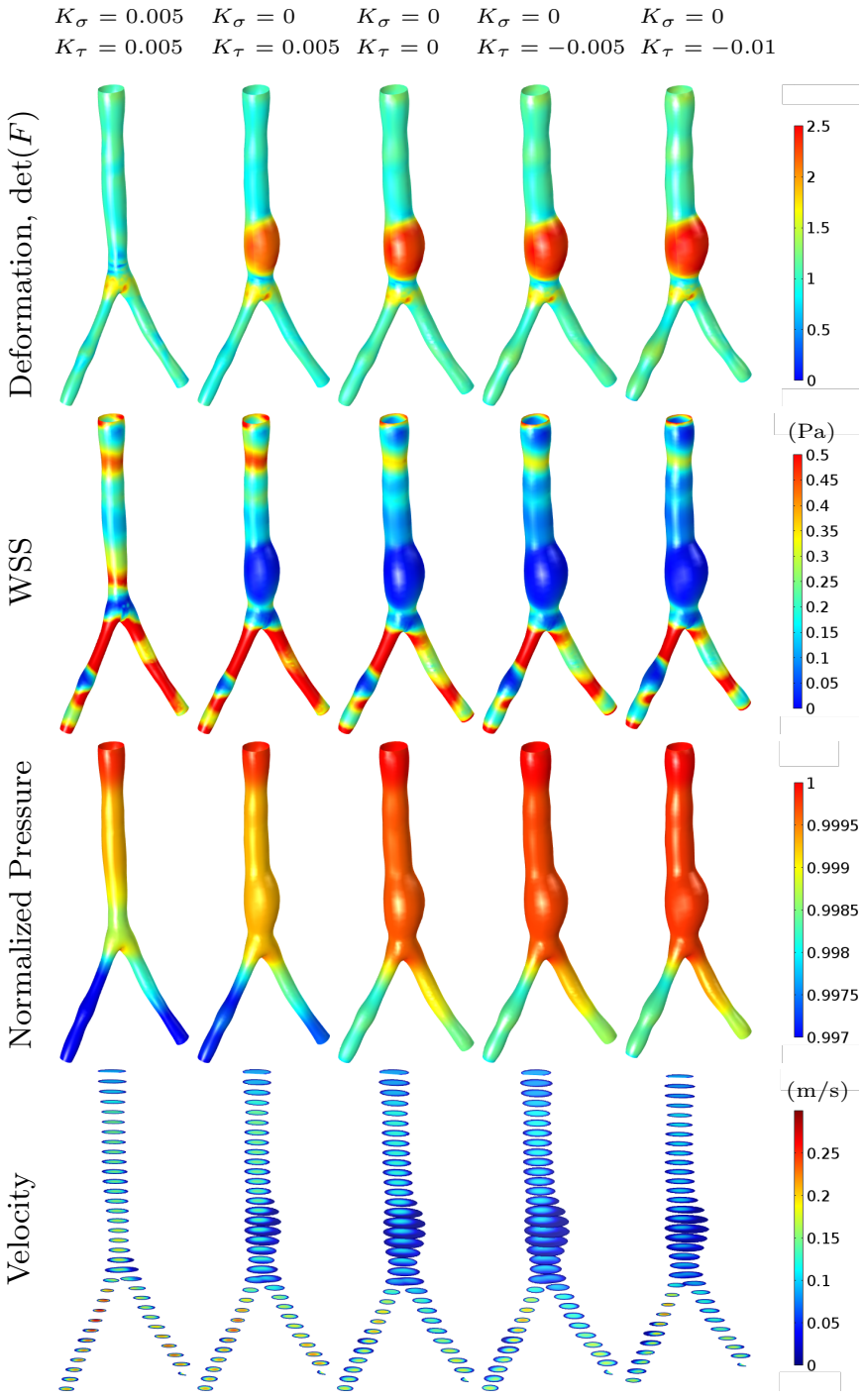

Figure 2.6: Results from coupled simulation with blood flow. The mass loss shown in Fig. 2.4 (c) was used to trigger G&R in all cases. All panels represent the respective field and geometry at the end of 110 G&R steps, with each column representing different feedback gain choices. Pressure is normalized with respect to the peak value for each case: 13339, 13291, 13518, 13602, and 13688 Pascals respectively from left to right.

Chapter 3

Reconstructing vascular homeostasis by growth-based prestretch and optimal fiber deposition

3.1 Introduction

Mathematical modeling of the vascular homeostatic state requires consideration of many important factors, including the influence of residual stress and vessel wall structure. In this chapter, we propose a two-step approach to the reconstruction of the vascular homeostatic state. The first step aims to generate an appropriate residual stress level for a given configuration of the vessel, and the second step aims to generate optimal fiber alignments based on the stress field. Inspired by kinematic G&R models [97], [111], and [112], we introduce a prestretch tensor, obtained through an iterative process to match a prescribed homeostatic stress value at physiologic pressure. The deposition angle of the collagen fibers is then defined by the solution of an optimization problem, which enables the vessel to sustain the stress with minimal amount of biomass, while stochasticity is incorporated into this process to account for fiber dispersion. We further propose the application of supervised learning to predict the prestretch in vascular bifurcations or other geometric anomalies, where theory-based methods struggle due to topological singularities. Based on this overall framework, the generation of the residual stress field and fiber directions is made numerically stable for more realistic geometry. Beyond addressing the vascular homeostatic state reconstruction problem, the method proposed here provides a starting point for general biomechanical analyses, such as FSI simulations of soft tissue, where residual stress and proper fiber alignment play important roles.

3.2 Methods

3.2.1 Constrained mixture model

The vessel wall is modeled as a constrained mixture [75] of collagen, elastin, and smooth muscle fibers, and we assume that all constituents deform as a continuum. The turnover of collagen and smooth muscle fibers is a process of degradation of existing material and production of new material, which can be described mathematically as

$$M^k(t) = M^k(0)Q^k(t) + \int_0^t m^k(\tau)q^k(t-\tau)\,\mathrm{d}\tau\ , \tag{3.1}$$

where k denotes different collagen or smooth muscle fiber families; $M^k(t)$ is the local mass density denoting the mass of the constituent k per unit volume in the reference configuration κ_0; and $m^k(t)$ is the corresponding mass production rate. $Q^k(t)$ is the remaining fraction of the initial mass for the constituent k at time t, and $q^k(t-\tau)$ is the remaining fraction at time t for the constituents produced at time τ. In contrast to collagen and smooth muscle fibers, functional elastin is only produced during early development and does not continuously turnover. Therefore, the time evolution of the mass density for elastin is given by

$$M^e(t) = M^e(0)Q^e(t)\ , \tag{3.2}$$

where $M^e(0)$ is the initial mass density for elastin, and $Q^e(t)$ is the remaining fraction of the initial mass.

Following [61], elastin fibers are modeled as an incompressible isotropic neo-Hookean material and the constitutive relation is given by the strain energy function per unit mass

$$W^e(\mathbf{C}) = \frac{c_1}{2}\left(I_1(\mathbf{C}) - 3\right)\ , \tag{3.3}$$

where $c_1 > 0$ is a stress-like material parameter and $I_1(\mathbf{C}) = \mathrm{tr}(\mathbf{C})$ is the first invariant of the right Cauchy-Green deformation tensor $\mathbf{C}$ which is defined with respect to the reference configuration κ_0. Collagen and smooth muscle fibers are modeled as an anisotropic Fung-type material and the constitutive relations for each family is given by the strain energy function per unit mass

$$W^k(\mathbf{C}) = \frac{c_2}{4c_3}\left\{\exp\left[c_3\left(I^k(\mathbf{C},\mathbf{E}^k_\mathrm{f}) - 1\right)^2\right] - 1\right\}\ , \tag{3.4}$$

where $I^k(\mathbf{C},\mathbf{E}^k_\mathrm{f}) := \mathbf{C} : \mathbf{E}^k_\mathrm{f} \otimes \mathbf{E}^k_\mathrm{f}$ is the fiber invariant corresponding to the square of the stretch λ^k of fiber family k; $\mathbf{E}^k_\mathrm{f}$ is the fiber direction in the reference configuration κ_0.

Based on the mixture rule [75], the total strain energy of the constrained mixture is

$$\begin{aligned} w(\mathbf{C},t) &= M^e(0)Q^e(t)W^e(\mathbf{C},t) \\ &\quad + \sum_k M^k(0)Q^k(t)W^k(\mathbf{C},t) \\ &\quad + \sum_k \int_0^t m^k(\tau)q^k(t-\tau)W^k(\mathbf{C},t,\tau)\,\mathrm{d}\tau \\ &:= w^e(\mathbf{C},t) + \sum_k w^k(\mathbf{C},t)\ . \end{aligned} \tag{3.5}$$

The strain-energy function for collagen and smooth muscle fibers, $W^k(\mathbf{C},t,\tau)$, depends on both the current time t and the time that the fibers are produced τ, which also determines the natural configurations for the fibers.

To incorporate the nearly incompressible behavior of vascular tissue, a standard decomposition [46, 61] of the strain energy was used

$$w(\mathbf{C},t) = U(J) + w(\bar{\mathbf{C}},t)\ , \tag{3.6}$$

$w(\bar{\mathbf{C}})$ is termed the isochoric component and

$$\bar{\mathbf{C}} = J^{-2/3}\mathbf{C}\ . \tag{3.7}$$

The volumetric component $U(J)$ is given by

$$U(J) = \frac{\kappa}{2}(J-1)^2\ , \tag{3.8}$$

with κ the bulk modulus and J the determinant of the deformation gradient tensor. By way of Eq. (3.8), changes to M^k affect both the referential and spatial density of fibers in the tissue; this has to be taken into account when setting initial values for the mass densities in Eq. (3.5).

Note that decomposition in Eq. (3.6) for fiber-reinforced materials can lead to the fiber material contributing stresses orthogonal to the fiber direction [100, 59, 55]. This can be mitigated by using more advanced finite elements [133], or if the bulk modulus is sufficiently large. Although a more consistent decomposition was discussed [100, 59, 55], we found that results of passive inflation from this method were consistent with those derived from using Eq. (3.6) for physiologic pressure values, and the decomposition in Eq. (3.6) was more numerically stable. Nonetheless, either decomposition is possible as the underlying approach presented herein does not inherently depend on this decomposition.

Once the total strain energy of the mixture is formulated, the deformation of the vessel wall can be obtained by applying the virtual work principle

$$\delta I = \int_{\Omega_0} \delta w\,\mathrm{d}V + \int_{\partial\Omega_t} P\,\mathbf{n}_t \cdot \delta x\,\mathrm{d}a = 0\ , \tag{3.9}$$

where δI is the virtual work; Ω_0 is the vessel tissue in the reference configuration; $\partial\Omega_t$ is the inner surface of vessel in the current configuration; P is the transmural blood pressure; $\mathbf{n}_t$ is the outward normal; and δx is the virtual displacement.

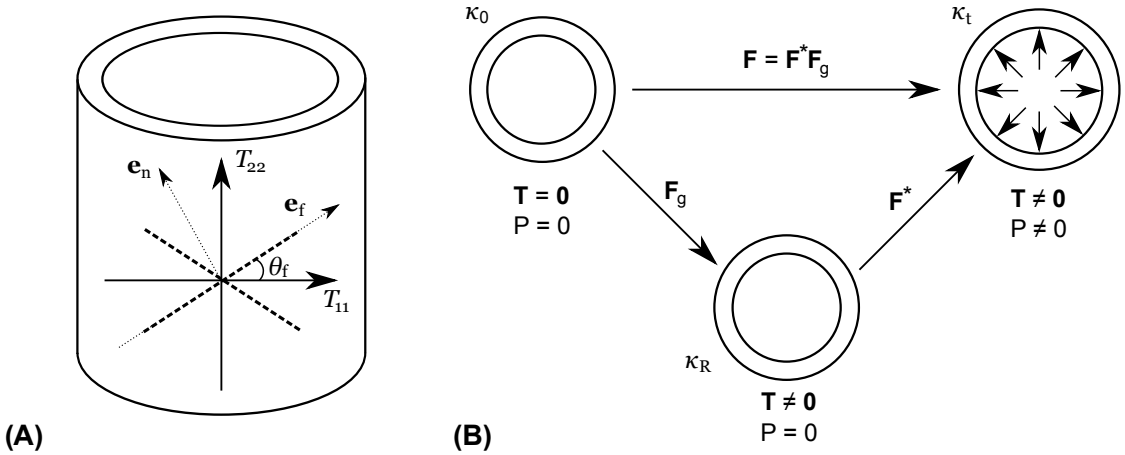

Figure 3.1: (A) T_{11} and T_{22} are the two principal stress directions of the Cauchy stress tensor $\mathbf{T}$; θ_f is the deposition angle of fiber family $\mathbf{e}_f$; and $\mathbf{e}_n$ the fiber normal direction. (B) Relation between different configurations. κ_0 is the unstressed reference configuration ($\mathbf{T} = \mathbf{0}$); κ_R is the configuration with residual stress incorporated; κ_t is the current configuration with external pressure imposed.

3.2.2 Residual stress field generation

3.2.2.1 Basic methodology

In vascular growth and remodeling theory, a nominal homeostatic stress value σ_h is typically assumed [49], and the residual stress field helps to create this homogenized stress distribution [25] and [71]. We define residual stress implicitly through a "growth tensor" $\mathbf{F}_g$ that maps the unstressed reference configuration κ_0 of the vessel to the unpressurized configuration with residual stress κ_R, see Fig. 3.1(B). This approach is similar to prior works [97] and [111] that have used $\mathbf{F}_g$ to broadly describe deformation due to growth and remodeling in *development*. Tensor $\mathbf{F}^*$ in Fig. 3.1(B) describes additional deformation due to *loading*, i.e., pressurization by pressure P. Thus, the total deformation $\mathbf{F}$ with respect to the reference configuration κ_0 is given by

$$\mathbf{F} = \mathbf{F}^*\mathbf{F}_g \ , \tag{3.10}$$

where the growth tensor $\mathbf{F}_g$ is determined by the growth stretch ratios in local (r, θ, z)-directions

$$\mathbf{F}_g = \mathrm{diag}\left(\lambda_{gr}, \lambda_{g\theta}, \lambda_{gz}\right) \ . \tag{3.11}$$

If the growth stretch ratios are known (discussed below), the elastic deformation gradient tensor $\mathbf{F}^*$ and right Cauchy-Green deformation tensor can be written as

$$\mathbf{F}^* = \mathbf{F}\mathbf{F}_g^{-1}, \quad \mathbf{C}^* = \mathbf{F}_g^{-T}\mathbf{C}\mathbf{F}_g^{-1} \ , \tag{3.12}$$

and substituted into Eq. (3.5) to yield the total strain energy of the constrained mixture

$$w(\mathbf{C}^*, t) = w^e(\mathbf{C}^*, t) + \sum_k w^k(\mathbf{C}^*, t) \ . \tag{3.13}$$

The strain energy function is used to define the variational equations for momentum balance, which can be solved numerically to compute the stress distribution. Note, the strain energy in Eq. (3.13) can be decomposed according to Eq. (3.6). For the volumetric part, nearly-constant volume is imposed by

$$U(J) = \frac{\kappa}{2}(J^* - 1)^2 \ , \tag{3.14}$$

where $J^* = \det(\mathbf{F}^*)$. In general, for processes involving growth and remodeling (especially for development), constant volume should not be assumed, however it is a reasonable here since the contribution from $\mathbf{F}_g$, which captures the main volumetric change of the development stage, is excluded.

3.2.2.2 Growth stretch ratios

Above we assume the growth stretch ratios are know. Here we discuss how these can be computed. The basic premise is residual stress (and hence growth stretch ratios) tend to help homogenize the stress state in the loaded configuration, thus helping to define a homeostatic stress state. While the concept of hemostatic stress is fundamental to vascular biomechanics, there is no consensus on its exactness. It has been shown that residual stress homogenizes circumferential stress in the radial direction, but it remains unclear whether homeostatic stress varies spatially. Therefore, for generality we assume that there exists a (known) homeostatic stress *distribution* σ_h and that the growth stretch ratios homogenize circumferential stress in the radial direction. In §3.2.2.3, we discuss computation of σ_h; however, the material here applies to any desired homeostatic stress distribution.

In solving the variational equations for momentum balance, the growth stretch ratios are updated to produce a desired homeostatic stress distribution σ_h. Namely, following [111] and [112], the growth stretch ratios are updated according to the following evolution equations

$$\frac{\dot{\lambda}_{\mathrm{g}\theta}}{\lambda_{\mathrm{g}\theta}} = \frac{1}{\tau_\theta}\left(\frac{\sigma_\theta(t)}{\sigma_\mathrm{h}} - 1\right), \quad \dot{\lambda}_\mathrm{gr} = 0, \quad \dot{\lambda}_\mathrm{gz} = 0 \ , \tag{3.15}$$

where τ_θ is a time constant controlling how fast the growth stretch evolves. Thus, the momentum equations are coupled with these evolution equations and solved in a staggered procedure until convergence of the stretch ratios (and, based on Eq. (3.15), circumferential stress). The algorithm for this iterative procedure can be found in the Appendix. Note, radial stress is governed primarily by the boundary conditions at the inner and outer surfaces, not residual stress [68]. It is also small in comparison to the circumferential stress, which has been shown experimentally [122] and computationally [61], [73], and [23]. Additionally, the axial stress component is mainly determined by the boundary condition and geometry of the vessel. Therefore, only convergence of circumferential stress is considered here. More details can be found in [113], [112], [71], and [74].

3.2.2.3 Defining the homeostatic stress distribution

The method above can be applied for any homeostatic stress σ_{h}, which can generally vary spatially. Indeed, Fung [49] demonstrated that residual stress tends to make the stress distribution uniform primarily in the transmural direction. Hence, we aim to formulate a target homeostatic stress distribution $\sigma_h(x)$ that is uniform in the transmural direction, but may vary in the circumferential and axial directions. This can be formulated through the steady-state solution of the following diffusion equation defined in the vessel wall domain Ω_0 as

$$\begin{aligned} \frac{\partial}{\partial t}\sigma_{\mathrm{h}}(x,t) &= D\nabla^2\sigma_{\mathrm{h}}(x,t), && \text{for } x \in \Omega_0, t \in [0,T] \\ \sigma_{\mathrm{h}} &= g(x), && \text{for } x \text{ on } \Gamma_{\mathrm{inner}}, \\ \mathbf{n}\cdot\nabla\sigma_{\mathrm{h}} &= 0, && \text{for } x \text{ on } \Gamma_{\mathrm{outer}}, \end{aligned} \tag{3.16}$$

where D is a virtual diffusion constant, and Γ_{inner} and Γ_{outer} denote the inner and outer wall of the vessel, respectively. Following [12] and [43], the stress distribution $g(x)$ can be obtained from a passive nonlinear elasticity membrane problem with constitutive relations Eqs. (3.3) and (3.4), and is effectively used here to assign the variation of stress in the circumferential and axial directions. This above system Eq. (3.16) is solved until steady state, which yields a stress distribution that is uniform in the transmural direction, and defines the target homeostatic stress under normal blood pressure.

Although the steady version of Eq. (3.16) could alternatively be used to obtain the steady state solution, we retain the unsteady version for generality since, as shown in Sect. 3.3, the unsteady formulation in Eq. (3.16) enables the ability to generate a quasi-uniform stress distribution in the transmural direction by controlling the simulation ending time T. This quasi-uniform distribution is generally in better agreement with expectations of transmural stress, particularly when considering deviations of blood pressure from the mean arterial pressure (see e.g., Fig. 7 in [14]).

3.2.2.4 Estimating residual stresses near bifurcations and boundaries

Generating the stretch ratios $\lambda_{\mathrm{gr}}, \lambda_{\mathrm{g}\theta}, \lambda_{\mathrm{gz}}$ is based on an iterative algorithm that couples the structural mechanics (momentum) equations (3.9) with the evolution equations (3.15). The iterative method can struggle to converge in bifurcation regions where the irregular geometry may cause stress to deviate significantly from the target homeostatic value. Nonetheless, the overall theoretical framework provides a governing connection to guide how geometric and mechanical factors determine the growth stretch ratio. Therefore, the convergence of this method otherwise throughout the model may be used indirectly to guide specification at locations where numerical factors become nuisance. Thus, instead of explicitly defining the growth stretch ratios at bifurcations or boundaries (or potentially other geometric anomalies), we exclude computational nodes close to these geometrical features, compute the growth stretch ratios in the rest of the domain according to the formulations above, and

use that data along with supervised learning to estimate the growth stretch ratios at the excluded locations.

For the supervised learning process, random forest regression was chosen based on its general accuracy and robustness against overfitting [47]. In order to take both mechanical and geometric factors into account, the initial local stress $\sigma_0(x_i)$ and the local curvature tensor $\mathbf{R}(x_i)$ are used as the prediction features, while local growth stretch ratio $\lambda_g(x_i)$ is the training label. The data pair $(\sigma_0(x_i), \mathbf{R}(x_i); \lambda_g(x_i))$ associated with each location x_i in the vascular geometry contributes to one data point in the overall training data sets. The mapping

$$\mathcal{M} : (\sigma_0(x_i), \mathbf{R}(x_i)) \mapsto \lambda_g(x_i) \tag{3.17}$$

is obtained by constructing a random forest regressor. In random forest regression, the prediction of $\lambda_g(x)$ is determined by the average of B individual regression trees characterized by their parameters Θ_b

$$\hat{f}_{\mathrm{rf}}^{B}(\sigma_0(x), \mathbf{R}(x)) = \frac{1}{B}\sum_{b=1}^{B} T_b(\sigma_0(x), \mathbf{R}(x)|\Theta_b) \ . \tag{3.18}$$

Each individual tree $T_b(\bullet)$ is constructed based on randomly sampled features and bootstrapped data sets, and the optimal tree parameters are obtained by minimizing the least square error

$$\Theta_b^* = \arg\min_{\Theta_b} \sum_{i=1}^{N} \left(\lambda_g(x_i) - T_b(\sigma_0(x_i), \mathbf{R}(x_i)|\Theta_b)\right)^2 \ . \tag{3.19}$$

Once Θ_b^* is obtained in the training process, given a new input $(\sigma_0(x_{\mathrm{new}}), \mathbf{R}(x_{\mathrm{new}}))$, the growth stretch ratio λ_g at the new location x_{new} can be computed as

$$\begin{aligned} \lambda_g(x_{\mathrm{new}}) &= \hat{f}_{\mathrm{rf}}^{B}(\sigma_0(x_{\mathrm{new}}), \mathbf{R}(x_{\mathrm{new}})) \\ &= \frac{1}{B}\sum_{b=1}^{B} T_b(\sigma_0(x_{\mathrm{new}}), \mathbf{R}(x_{\mathrm{new}})|\Theta_b^*) \ . \end{aligned} \tag{3.20}$$

We used the random forest regression implementation available from the Python package *Scikit-learn* [90].

3.2.3 Optimal stochastic fiber deposition

After the residual stress field is generated, stress-driven fiber deposition is incorporated to capture the fiber alignment in the homeostatic state. In most prior studies, collagen fibers are deposited in predefined directions [43], and all later newly produced collagen fibers are deposited to align with the existing corresponding collagen families. In this work, we assume fibers can be freely deposited in orientations based on the stress state at the time of deposition. Inspired by [29], the deposition angle is given by the solution of an optimization problem. Although the stress state is in fact triaxial for the 3D vascular geometry,

the radial component of stress is much smaller compared to the axial and circumferential component. Therefore, for simplicity, we assume the vessel is under a biaxial stress condition (see Fig. 3.1A) with T_{11} and T_{22} as the two largest eigenvalues of the Cauchy stress tensor $\mathbf{T}$ (we use $\mathbf{T}$ to denote the full Cauchy stress tensor and σ to denote scalar quantities derived from $\mathbf{T}$) , which is given by

$$\mathbf{T} = \frac{2}{J}\mathbf{F}\frac{\partial w}{\partial \mathbf{C}}\mathbf{F}^T \ . \tag{3.21}$$

We denote by $\sigma_{\mathrm{f,max}}$ the maximum stress that fibers can sustain when the fiber mass density is equal to some baseline value M_0. The maximum stress is assumed proportional to the fiber mass density. Thus, for any arbitrary fiber density M_f, the maximum stress that fibers can sustain is $\sigma_{\mathrm{f,max}}\frac{M_\mathrm{f}}{M_0}$, and the contribution of the fiber family to the local stress tensor is

$$\mathbf{T}_\mathrm{f} := \sigma_{\mathrm{f,max}}\frac{M_\mathrm{f}}{M_0}\mathbf{e}_\mathrm{f} \otimes \mathbf{e}_\mathrm{f} \ . \tag{3.22}$$

Here, $\mathbf{e}_\mathrm{f} = [\cos\theta_\mathrm{f}, \sin\theta_\mathrm{f}]^T$ is the fiber direction represented in the local coordinate system defined by the circumferential and axial directions and θ_f is the fiber deposition angle (see Fig. 3.1A). Note that the circumferential and axial directions and the deposition angle θ_f are all defined in the current configuration κ_t. Further, the local circumferential and axial directions are computed as the eigenvectors corresponding to the two largest eigenvalues T_{11} and T_{22} of the local Cauchy stress tensor $\mathbf{T}$ [32]. The projections of the fiber stress tensor $\mathbf{T}_\mathrm{f}$ in the circumferential and axial directions are

$$T_{\mathrm{f,circ}} = [1,0]\mathbf{T}_\mathrm{f}[1,0]^T = \sigma_{\mathrm{f,max}}\frac{M_\mathrm{f}}{M_0}\cos^2\theta_\mathrm{f} \ , \tag{3.23}$$

$$T_{\mathrm{f,axial}} = [0,1]\mathbf{T}_\mathrm{f}[0,1]^T = \sigma_{\mathrm{f,max}}\frac{M_\mathrm{f}}{M_0}\sin^2\theta_\mathrm{f} \ . \tag{3.24}$$

Assuming the body tends to minimize the mass needed for vascular fibers, while maintaining the ability to sustain circumferential and axial loading, the optimization problem to determine the deposition angle θ_f is given by

$$\begin{aligned} &\min_{M_\mathrm{f},\theta_\mathrm{f}} M_\mathrm{f} \quad \text{such that} \\ &\sigma_{\mathrm{f,max}}\frac{M_\mathrm{f}}{M_0}\cos^2\theta_\mathrm{f} \geq T_{11}, \\ &\sigma_{\mathrm{f,max}}\frac{M_\mathrm{f}}{M_0}\sin^2\theta_\mathrm{f} \geq T_{22} \ . \end{aligned} \tag{3.25}$$

The solution of Eq. (3.25) is

$$M_\mathrm{f}^* = \frac{T_{11}+T_{22}}{\sigma_{\mathrm{f,max}}}M_0, \tag{3.26}$$

$$\theta_\mathrm{f}^* = \pm\arctan\sqrt{\frac{T_{22}}{T_{11}}} \ , \tag{3.27}$$

which defines the optimal directions for newly produced collagen fibers. As T_{11} and T_{22} may change with time, θ_{f}^{*} is generally not constant. The "$\pm$" sign in Equation (3.27) corresponds to the two collagen families. It is worth noting that the optimal angle θ_{f}^{*} depends on the fiber mass density M_{f} indirectly via T_{11} and T_{22}.

It has been observed that fiber deposition exhibits a stress-dependent stochasticity [44]. We assume that the deposition angle follows a Gaussian distribution

$$\theta_{\mathrm{f}}^{k} \sim \mathcal{N}\left(\theta_{\mathrm{f}}^{*,k}, \Sigma(\sigma_{\mathrm{f}}^{*,k})\right) \ , \tag{3.28}$$

with mean value θ_{f}^{*}. The variance $\Sigma(\sigma_{\mathrm{f}})$ is defined as a function of the fiber stress σ_{f}

$$\Sigma(\sigma_{\mathrm{f}}^{*,k}) = \Sigma_0 \frac{\sigma_{\mathrm{scale}}}{\sigma_{\mathrm{f}}^{*,k}}, \tag{3.29}$$

where σ_{scale} is a scale parameter for vessel wall stress, and Σ_0 is the nominal value of the variance. To avoid numerical instabilities when $\sigma_{\mathrm{f}}^{*,k}$ is very small, a small positive number ϵ is added to the denominator of Equation (3.29). The stress in the new fiber direction is given by the projection of the Cauchy stress tensor onto the fiber direction

$$\sigma_{\mathrm{f}}^{*,k} = \mathbf{T} : \mathbf{e}_{\mathrm{f}}^{*,k} \otimes \mathbf{e}_{\mathrm{f}}^{*,k} \ . \tag{3.30}$$

$\Sigma(\sigma_{\mathrm{f}}^{*,k})$ is designed to be a decreasing function of the stress projection in the fiber direction $\sigma_{f}^{*,k}$ so that fibers are aligned more coherently when $\sigma_{\mathrm{f}}^{*,k}$ is higher [44]. Note that the optimal deposition direction $\mathbf{e}_{\mathrm{f}}^{*,k}$ and the actual fiber deposition direction $\mathbf{e}_{\mathrm{f}}^{k}$ are defined respectively as

$$\mathbf{e}_{\mathrm{f}}^{*,k} = [\cos\theta_{\mathrm{f}}^{*,k}, \sin\theta_{\mathrm{f}}^{*,k}]^{\top} \ , \tag{3.31}$$

$$\mathbf{e}_{\mathrm{f}} = [\cos\theta_{\mathrm{f}}, \sin\theta_{\mathrm{f}}]^{\top} \ . \tag{3.32}$$

Once the fiber deposition directions $\mathbf{e}_{\mathrm{f}}^{k}$ at the time τ are determined in the deformed configuration κ_τ, the fiber direction in configuration κ_{R} can be computed as

$$\mathbf{E}_{\mathrm{f}}^{k}(\tau) = \frac{F^{*}(\tau)^{-1}\mathbf{e}_{\mathrm{f}}^{k}(\tau)}{\left\| F^{*}(\tau)^{-1}\mathbf{e}_{\mathrm{f}}^{k}(\tau) \right\|} \ , \tag{3.33}$$

and the invariant of this fiber at a later time t is

$$I^{k}(\mathbf{C}^{*}(t), \mathbf{E}_{\mathrm{f}}^{k}) := \mathbf{C}^{*}(t) : \mathbf{E}_{\mathrm{f}}^{k}(\tau) \otimes \mathbf{E}_{\mathrm{f}}^{k}(\tau) \ . \tag{3.34}$$

Substituting the fiber invariants into Equations (3.4) yields the strain energy for the collagen fiber

$$\begin{aligned} &W^{k}(\mathbf{C}^{*}(t), \mathbf{E}_{\mathrm{f}}^{k}(\tau)) \\ &= \frac{c_2}{4c_3}\left\{\exp\left[c_3\left(I^{k}(\mathbf{C}^{*}(t), \mathbf{E}_{\mathrm{f}}^{k}(\tau)) - 1\right)^{2}\right] - 1\right\} \ , \end{aligned} \tag{3.35}$$

and therefore the total strain energy for fiber family k can be computed based on Equation (3.5) as

$$\begin{aligned} w^k(\mathbf{C}^*, t) &= \int_{-\infty}^{t} m^k(\tau) q^k(t-\tau) W^k(\mathbf{C}^*(t), \mathbf{E}_{\mathrm{f}}^k(\tau))\, \mathrm{d}\tau \\ &= \int_{t-\hat{t}}^{t} m^k(\tau) q^k(t-\tau) W^k(\mathbf{C}^*(t), \mathbf{E}_{\mathrm{f}}^k(\tau))\, \mathrm{d}\tau \\ &\approx \sum_{i=0}^{N} m^k(\tau_i) q^k(t-\tau_i) W^k(\mathbf{C}^*(t), \mathbf{E}_{\mathrm{f}}^k(\tau_i)) \Delta\tau \ , \end{aligned} \tag{3.36}$$

where $\hat{t}$ is the lifespan of the fibers. N is the number of discretization intervals for computing the time integral. Note that, for each time slice $\Delta\tau = \tau_{i+1} - \tau_i$, the strain energy of the fiber produced at τ_i depends on the deposition angle at that time $\theta_{\mathrm{f}}(\tau_i)$. Based on the total strain energy for the current moment t, the current stress distribution can be computed, which can be used to compute the new optimal fiber deposition angle for the next time step. The general algorithm for applying the above method is described in the Appendix.

3.3 Results

The framework proposed above was implemented to first generate a residual stress field based on the evolution equations (3.15) and then to iteratively generate collagen fiber directions based on the optimality conditions (3.27) along with deposition randomness (3.28). The code was developed in Python, and the finite element solution was implemented using the open source package *FEniCS* [84]. All computations were performed using linear tetrahedral elements with an average edge size smaller than 0.7 mm. The constitutive material parameters were taken from literature [52], [138], and [42] and are summarized in Tab. 3.1 along with the other parameters used for the simulations.

Fig. 3.2 illustrates the results of the algorithm applied to an idealized cylindrical vessel. Panel (A) shows the circumferential stress distribution for a passive inflation with a pressure of 100 mmHg in which the material properties are assumed to be constant throughout the vessel wall and no residual stress is incorporated. As expected the resulting circumferential stress is nonuniform along the transmural direction. Panel B displays the circumferential stress distribution after prestretch is incorporated by the stretch evolution equation (3.15) using a prescribed homeostatic stress σ_{h} of 150 kPa. The convergence of the stress to the homeostatic value over the iterations of the algorithm is plotted in Fig. 3.3 for the cylindrical test case.

Similar numerical simulations were carried out for a patient-specific aortic bifurcation geometry. The original image data was obtained from the Vascular Model Repository (`http://vascularmodel.org`), and a membrane model was constructed using SimVascular [116]. After that, a 3-D volumetric mesh is generated using *Gmsh* [53], and the local

thickness of vessel wall is set to be equal to 10% of the local radius (obtained from maximum inscribed sphere). A homeostatic stress distribution $\sigma_{\mathrm{h}}(x)$ was generated by solving the diffusion equation (3.16) with $g(x)$ set to be the solution of a passive inflation membrane problem at mean arterial pressure of 100 mmHg. Fig. 3.4A displays the steady-state $\sigma_{\mathrm{h}}(x)$, which serves as the target stress distribution for the residual stress generation process. For comparison, Fig. 3.4B displays the stress distribution of a passive inflation with a pressure of 100 mmHg with no residual stress incorporated. As an intermediate step, Fig. 3.4C displays the stress distribution when residual stress generation is applied only to the cylindrical portions of the domain with the inlet, outlet, and bifurcation regions excluded–hence, results in these regions may be considered invalid. The prestretch distribution at the excluded nodes were then predicted by a random forest regressor trained via the data from the remainder of the simulation domain. The resulting final stress distribution is shown in Fig. 3.4D, which qualitatively and quantitatively matches with the nominal target stress distribution shown in Fig. 3.4A. To better visualize the stress distribution near the bifurcation and the effectiveness of the prediction by the random forest regressor, a rescaled and zoom-in view is provided in Fig. 3.4E. It can be seen that higher stress is concentrated along the bifurcation ridge, consistent with previously published results [92].

To evaluate the stress distribution along the thickness directions, cross-sectional views are provided in Fig. 3.5, with panel (A) corresponding to the simulation without residual stress and panel (B) corresponding to the simulation with residual stress incorporated. It can be seen that although the stress distribution is not uniform throughout the geometry, the stress becomes uniform along the thickness when prestretch is included, (and becomes generally more homogenized in other directions although this is not imposed).

Once prestretch is generated, the residual stress distribution can be obtained by releasing the internal pressure and remove tethering boundary conditions. Fig. 3.2C shows the residual stress distribution after a virtual pressure release. It is noteworthy that the circumferential stress in the inner layer is negative – the tissue is under compression – and the stress in the outer layer is positive – the tissue is under extension – which is consistent with prior published results [2]. Qualitatively the pattern of the stress distribution also matches with experimental results on rabbit arteries in [25]. The randomness of the stress distribution is mainly due to the stochasticity of the fiber deposition. Note that for this virtual pressure release experiment, a small axial stretch is needed to achieve numerical stability. Namely, this applied axial stretch makes the inner layer of the vessel less prone to buckle while under compression. While this can be done for an idealized cylinder geometry by applying a small displacement to one of the free ends, this is not a trivial task for more general geometries and results may become unreliable (cf. [65] and [82]), which was confirmed for the patient-specific geometry.

The computation of the prestretch distribution is based on first treating the collagen

fibers as isotropic, the constitutive relation of which is given by the dispersion model [51]

$$\begin{aligned} W^k(\mathbf{C}) &= \frac{c_2}{4c_3}\left\{\exp\left[c_3\left(I_*^k-1\right)^2\right]-1\right\}\ , \\ I_*^k &:= \left(\omega_\mathrm{d}\mathbf{I}+(1-3\omega_\mathrm{d})\mathbf{E}_\mathrm{f}^k\otimes\mathbf{E}_\mathrm{f}^k\right):\mathbf{C} \end{aligned} \tag{3.37}$$

with the dispersion parameter ω_d equal to $\frac{1}{3}$. This is because prestretch is caused by unbalanced growth during the early development when the vascular material is more isotropic. Once the proper amount of prestretch was incorporated, the isotropic collagen fiber network is replaced by anisotropic fibers by setting the dispersion parameter $\omega_\mathrm{d}=0$ (which recovers the original anisotropic constitutive relation Eq. (3.4)) and deposited in the optimal directions defined by Eq. (3.27), with randomness included as described in Sect. 3.2.3. Fig. 3.6 shows the two helical fiber directions generated by the optimal fiber deposition algorithm for both idealized and patient-specific geometries. It can be seen that in both cases that the fiber directions show dispersion instead of perfect alignment in a particular direction, which corresponds to experimental observations [88]. Fig. 3.6B also shows the fiber directions in the bifurcation region of the patient-specific geometry, which qualitatively matches the results in [56].

Since in most practical applications the vascular geometry is derived from *in vivo* imaging, it is important to consider how the generation of residual stress affects the final loaded configuration. Comparison of the loaded, prestretched geometry to the original image-based geometry is shown in Fig. 3.7C, which indicates that the proposed algorithm changes the shape of the geometry to a relatively small degree. By comparison, an inflation that does not consider residual stress results in a more curved and displaced loaded configuration as shown in Fig. 3.7A. Also for comparison, we considered the case of prescribing a uniform homeostatic stress distribution, which as shown in Fig. 3.7B tends to undesirably straighten the artery as might be expected since such configuration would be desirable to achieve more uniform stress.

Used for	Parameter		
Material model Eqs. (3.3, 3.4, 3.8)	$c_1 = 688\,\mathrm{Pa/kg}$ $\kappa = 5\times10^6\,\mathrm{Pa}$	$c_2 = 917\,\mathrm{Pa/kg}$	$c_3 = 25\ [-]$
Fiber deposition Eqs. (3.29, 3.36)	$\Sigma_0 = 0.5$ $\hat{t} = 1$	$\sigma_\mathrm{scale} = 200\,\mathrm{kPa}$ $N = 20$	$\epsilon = 0.001$
Residual stress field generation Eqs. (3.15, 3.16)	Cylinder: $\sigma_\mathrm{h} = 150\,\mathrm{kPa}$ Patient-specific model, nominal blood pressure: $P = 100\,\mathrm{mmHg}$ $D = 1.0$	$\tau_\theta = 2.0$	

Table 3.1: Parameters used in the numerical experiments. Note that all time constants are normalized with respect to the lifespan of the fibers.

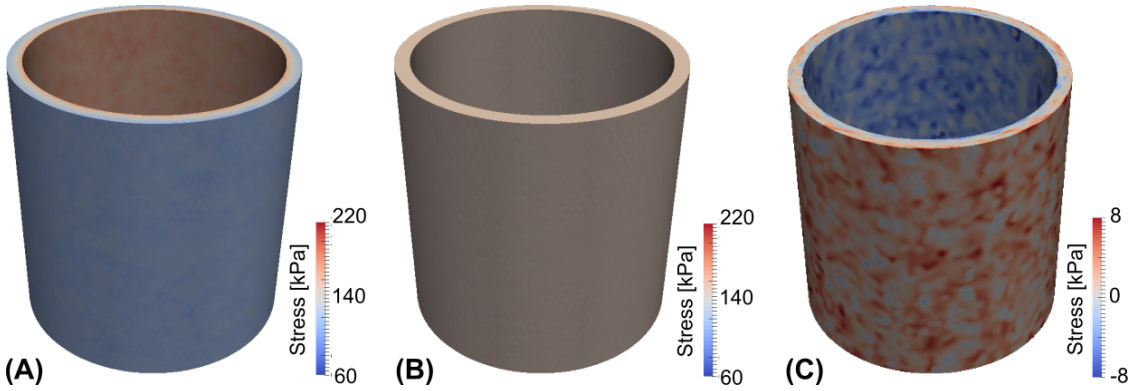

Figure 3.2: Circumferential stress distribution (A) of a standard passive inflation simulation; (B) with residual stress incorporated; (C) residual stress.

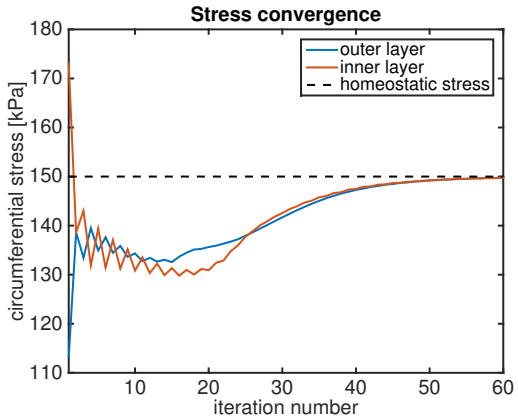

Figure 3.3: Convergence of the circumferential stress to the homeostatic stress after prestretch is incorporated based on Eq. (3.15). The red curve denotes the inner layer and the blue curve denotes the outer layer.

3.4 Discussion

A computational framework to generate the vascular homeostatic state has been proposed, which includes the generation of appropriate prestretch distribution and the specification of physiological vascular fiber deposition directions. A benefit of this framework is that in order to generate the residual stress distribution only a homeostatic stress value (or distribution) needs to be specified. In particular, the specification of the natural configurations of the different constituents and the mechanobiological mechanisms that form the residual stress distribution are not explicitly required and the effects of the residual stress distribution can be incorporated into a growth tensor $\mathbf{F}_{\mathrm{g}}$. This greatly facilitates the determination and generation of the residual stress distribution needed to achieve a homeostatic stress condition for the pressurized *in vivo* state for a particular vascular model geometry. While the approach

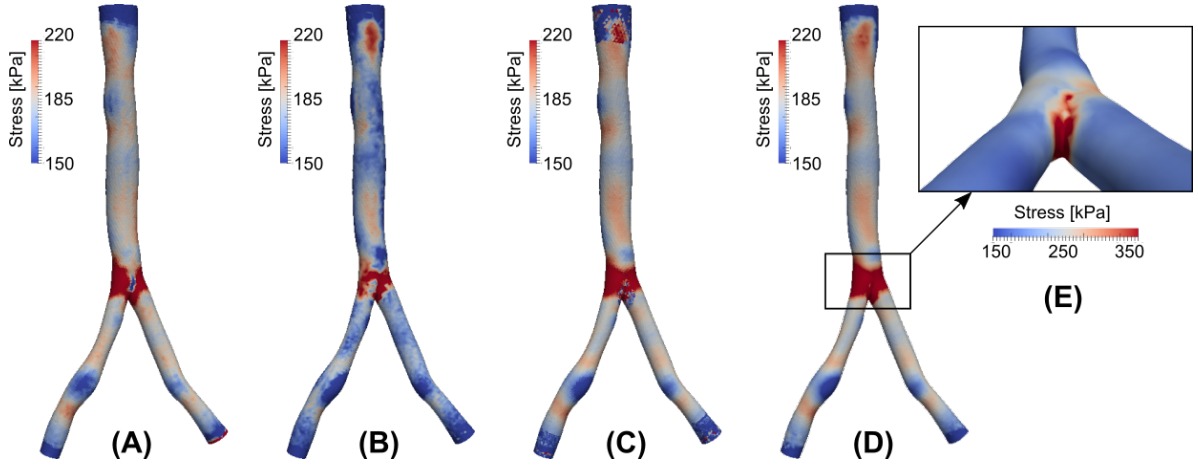

Figure 3.4: (A) Nominal homeostatic stress distribution determined from membrane problem. (B) Stress distribution from a standard passive inflation simulation. (C) Stress distribution after incorporation of residual stress. (D) Stress distribution after residual stress and machine learning repair. (E) Stress distribution near bifurcation (note change in color scale).

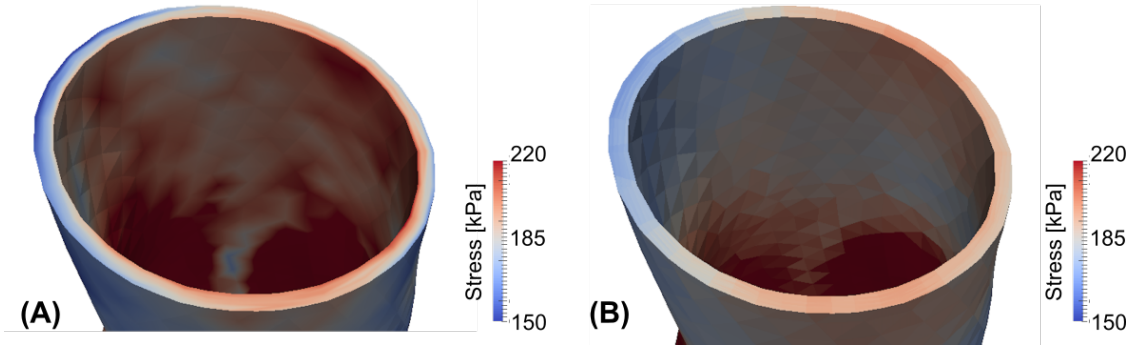

Figure 3.5: Circumferential stress distribution (A) of a standard passive inflation simulation for a patient-specific geometry; (B) with residual stress incorporated for a patient-specific geometry.

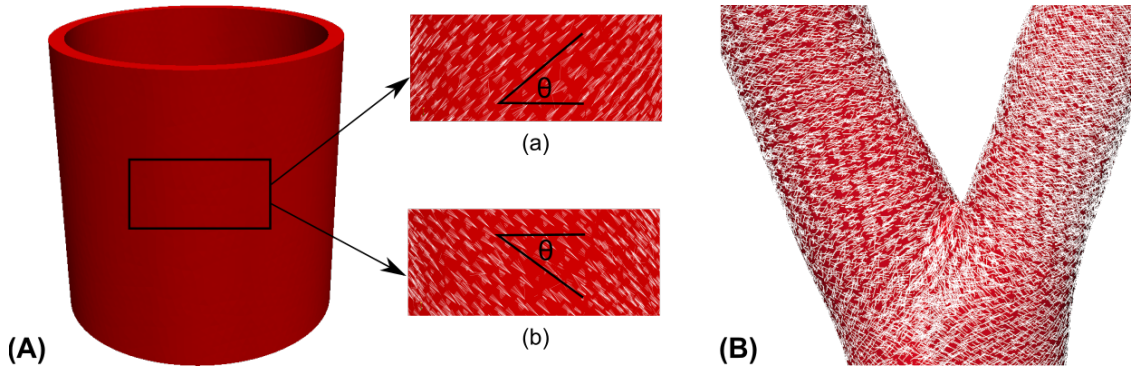

Figure 3.6: (A) Fiber directions in both helical directions for the cylinder geometry; (B) Fiber directions for the patient-specific geometry near the vascular bifurcation.

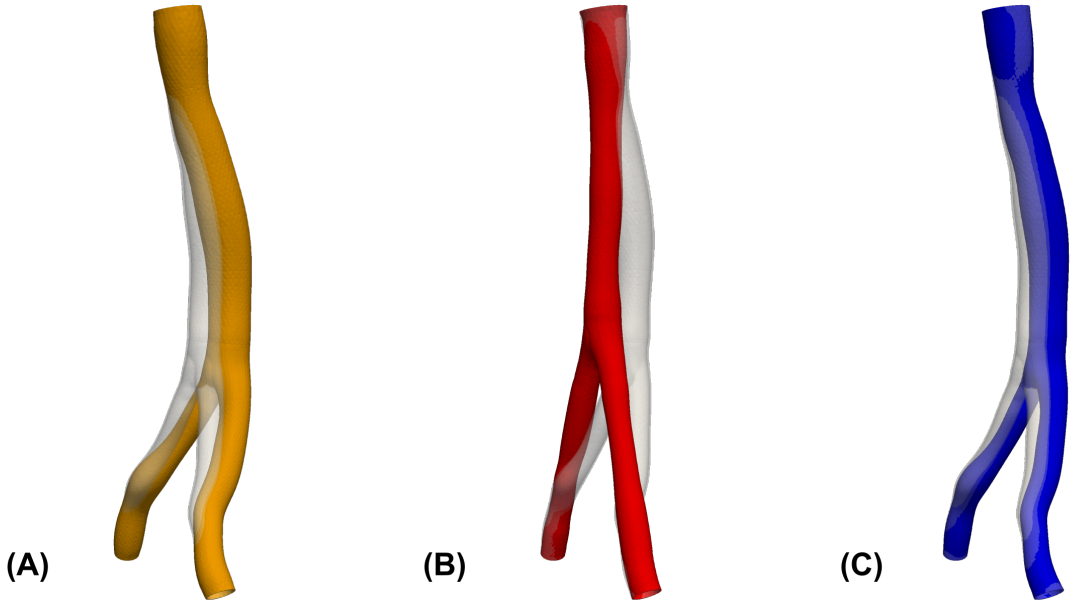

Figure 3.7: Comparison of the original geometry taken from imaging (transparent gray) with the displacement field of (A) an inflation experiment without the application of the residual stress; (B) an inflation experiment with residual stress generated from the uniform homeostatic stress distribution; (C) an inflation with residual stress generated from the residual stress distribution that is uniform only in transmural direction.

for generating the residual stress and fiber distribution through a growth tensor is inspired by classical G&R theories [75, 28, 54], it should not be confused with trying to reproduce the actual G&R process (but rather focuses on the end result of deriving an appropriate loaded and pre-stressed homeostatic state).

A unique feature of this work is the combination of the constrained mixture model of G&R [75] with an optimal fiber deposition process. In the constrained mixture model of G&R, fibers are commonly deposited in predefined fiber family directions, with new fibers aligned in the same direction as the existing fiber family directions. In this work, fibers are deposited based on a physiologically-motivated angle that depends on the current local stress state, instead of predefined directions. And since the local stress may vary over the iterative deposition process, the deposition angle of newly produced fibers also varies. This results in fiber dispersion, which has been well documented in human arteries, see, e.g., [88]. While prior works [51] have accounted for fiber dispersion using a set dispersion parameter κ_d, the method herein naturally leads to dispersion as a result of a stress-driven process. Also, in comparison to prior work [56] that suggests a nominal deposition angle of the form $\tan\theta_{\mathrm{f}}^{*} = \frac{T_{22}}{T_{11}}$, the physiologically-motivated optimal deposition angle employed herein suggest an alternative square root relation of the form $\tan\theta_{\mathrm{f}}^{*} = \sqrt{T_{22}/T_{11}}$ which is consistent with the results shown in [29].

For cylindrical regions, the prestretch distribution can be readily computed using iterative methods, as have been applied previously, e.g, [14], [2], and [93]. However, this method is often unstable when applied to more complex geometries, particularly since the topological features of the bifurcation cause irregular stress distribution that can significantly deviate from the prescribed homeostatic distribution. Thus, instead of being directly computed, the prestretch for the bifurcation region is predicted based on local geometric and mechanical properties from surrounding regions using a random forest regression. The logic here is that we assume the mapping from mechanical and geometric factors to the growth stretch ratio should guide specification regardless of numerical challenges. This provides a way to deal with realistic applications where geometric complexities are difficult to handle numerically using strictly theory-based methods, while maintaining specification based on a governing theory. As with most machine learning, the mapping is not necessarily guaranteed to satisfy a theoretical (fiber-deposition) principle, it is rather trained from the principle. However, it is possible to mathematically constraints inference problems to satisfy deterministic constraints [135].

While prior work has proposed the inclusion of residual stress on a fully three-dimensional patient-specific geometry [3], this approach results in a largely deformed loaded configuration, whereas the method proposed here results in relatively minor distortion of the loaded configuration when compared to the image-derived configuration (see Fig. 3.7C). We note that the distortion that does persist could be due in part to the lack of external tissue support from surrounding organs, which is missing in our model. Additionally, although not explored herein, patient-specific calibration of simulation parameters could be incorporated in the residual stress generation procedure such that the final loaded configuration

matches as closely as possible with the image-based geometry. This is a reasonable addition since model parameters are generic and often fitted from *ex-vivo* experimental data. Also, compared to [20] where the authors presented a backward displacement method to generate prestrech for a patient-specific geometry, our algorithm additionally incorporates stress homogenization and a more physiological material model including the generation of fiber directions. We note that although prior studies have assumed that there is a unique homeostatic stress value [41, 13, 134], there is sparse experimental data confirming this. The seminal work of Fung [49], indicates that stress tends to be homogenized in the transmural direction, and hence the approach presented herein assumes only homogenization of homeostatic stress in the transmural direction. Moreover, using a constant homeostatic stress value results in unphysiologic model deformation as shown in Fig. 3.7(B). Nonetheless, the algorithm presented herein can accommodate any desired homeostatic stress distribution. For example, a presumed constant value can be taken from literature [12, 137], or obtained from additional computations, such as using the stress distribution from an equivalent membrane problem as proposed herein, or computed as the mean stress throughout the geometry from a passive inflation simulation. Likewise, while this method was applied to reconstruct the nominal, healthy homeostatic state, it could potentially be applied to specify the residual stress distribution and fiber alignment in diseased vessels by appropriate change to model parameters.

We note here several limitations of this work. First, to generate the residual prestretch distribution, a homeostatic stress value or distribution needs to be known. Properly specifying this function is nontrivial; it can either be taken from literature [12] and [137] or obtained from additional computations, such as using the stress distribution from an equivalent membrane problem as proposed herein or computed as the mean stress throughout the geometry from a passive inflation simulation. Moreover, the robustness of the generation process should be further verified with a larger number of patient specific geometries. Also, the vessel wall in our study was modeled as a single effective layer while in reality the blood vessels consists of multiple layers that are mechanically relevant. However, this framework can be readily extended to a multi-layer setting (i.e., explicitly modeling the media and adventitia) with corresponding parameters specified for each layer. Likewise, while this method was applied to reconstruct the nominal, healthy homeostatic state, it could potentially be applied to specify the residual stress distribution and fiber alignment in diseased vessels by corresponding changes to model parameters.

3.5 Conclusions

We presented a framework to reconstruct the vascular homeostatic state by developing a method to compute the residual stress distribution and fiber directions. The residual stress is implicitly incorporated by iteratively computing a growth prestretch based on a prescribed homeostatic stress distribution. Vascular fiber directions are further incorporated based on the solution of a physiologically-motivated optimization problem. The methodology was ap-

plied to an idealized cylindrical geometry and a patient-specific aortic bifurcation geometry. Simulation results for residual stress distribution and fiber alignment match with numerical and experimental results in prior works. In contrast to previous studies the proposed framework is not limited by geometrical restrictions such as bifurcations making it more applicable to patient-specific scenarios.

Appendix

The two-stage algorithm to generate the vascular homeostatic state.

1. Generate residual stress field by incorporating proper amount of growth prestretch:

   - Define initial guesses for the growth prestretch:

   $$\lambda_{\mathrm{g}\theta} = 1, \quad \lambda_{\mathrm{gr}} = 1, \quad \lambda_{\mathrm{gz}} = 1 \; ;$$

   - **Do** :

     a) Solve the balance equation

     $$\delta I = \int_{\Omega_0} \delta w \, \mathrm{d}V + \int_{\partial\Omega_t} P \, \mathbf{n}_t \cdot \delta x \, \mathrm{d}a = 0 \; ,$$

     to obtain current stress.

     b) **Exit loop if** $\|\sigma_\theta - \sigma_{\mathrm{h}}\| < \epsilon$.

     c) Update the current prestretch ratios:

     $$\lambda_{\mathrm{g}\theta}^{(t+1)} = \lambda_{\mathrm{g}\theta}^{(t)} + \frac{\Delta t}{\tau_\theta} \left(\frac{\sigma_\theta^{(t)}}{\sigma_{\mathrm{h}}} - 1 \right) \lambda_{\mathrm{g}\theta}^{(t)},$$
     $$\lambda_{\mathrm{gr}}^{(t+1)} = 1,$$
     $$\lambda_{\mathrm{gz}}^{(t+1)} = 1 \; .$$

     d) $t = t + 1$ and return to (a).

     End loop.

2. Generate fiber deposition angles and incorporate fibers into the vascular mixture:

   - **For** $i = 1$ to i_{max}:

     a) Solve the balance equation

     $$\delta I = \int_{\Omega_0} \delta w \, \mathrm{d}V + \int_{\partial\Omega_t} P \, \mathbf{n}_t \cdot \delta x \, \mathrm{d}a = 0 \; ,$$

     to obtain current stress tensor $\mathbf{T}$, and then compute two principal stress components T_{11} and T_{22}.

     b) Compute the optimal deposition angle

     $$\theta_{\mathrm{f}}^* = \pm \arctan \sqrt{\frac{T_{22}}{T_{11}}} \; ,$$

     and generate the actual deposition angles based on the following distribution:

     $$\theta_{\mathrm{f}} \sim \mathcal{N} \left(\theta_{\mathrm{f}}^*, \Sigma(\sigma_{\mathrm{f}}) \right) \; .$$

c) Modify the strain energy function to incorporate the new fibers:

$$w^k(\mathbf{C},t) = \sum_{i=0}^{N} m^k(\tau_i) q^k(t-\tau_i) W^k(\mathbf{C}, \theta_{\mathrm{f}}(\tau_i), t) \Delta\tau \ .$$

End loop.

Chapter 4

Stability Analysis of Vascular Growth and Remodeling

4.1 Introduction

The functional adaptation of arteries to biomechanical stimuli has been long recognized as an important feature of vascular growth and remodeling (G&R), and has led to the development of mathematical theories to describe such phenomena [70]. A common theoretical framework has been the constrained mixture theory model for studying growth and remodeling of soft tissues [75]. Previous research in applying the constrained mixture theory of vascular G&R has focused mostly on numerical investigations, and especially in relation to aneurysm growth. For example, [13, 12] applied the constrained mixture theory to study stress mediated aneurysm expansion in idealized geometries to better understand different factors influencing geometry and aneurysm growth rate. Later, G&R theory was extended to 3D geometries to predict complex aneurysm shapes [138]. In addition, vascular G&R simulations have been coupled with blood flow dynamics to study the coupling between hemodynamics (e.g. wall shear stress) and vascular adaptations in cylindrical-type geometries [41, 128, 107], and more recently to patient-specific geometries [134].

It has been suggested [19, 11] that a better understanding for risk of aneurysm rupture may involve the stability of aneurysm expansion due to vascular G&R, i.e., rupture might be a result of unstable vascular G&R. While the above studies considered the numerical implementation of G&R in various applications, theoretical analysis of the stability of the underlying adaptive mechanism has received less attention. In this regard, the recent work of [101] studied the arterial growth instability using a goal function based approach. In important work of [30, 31], the authors introduced the concept of mechanobiological stability based on comprehensive analysis of the differential equations of mass density and vessel wall position from vascular G&R theory. As shown herein, the mathematical underpinnings of mechanobiological stability can be seen to have origins in the degenerate nature of the (linearized) system about the homeostatic state. This degeneracy complicates the use of

linear stability analysis to study the stability of the homeostatic state to infer the stability of the original (nonlinear) system.

In this chapter, we start from the integral state equations of the continuum based constrained mixture model of G&R and derive the state equations (time-delayed differential equations) describing vascular expansion. By employing a commonly used exponential form of the constituent survival function and by introducing an extended state variable, the delayed differential equations can be reduced to an ODE system. Linear stability analysis is subsequently applied to this ODE system and a stability criteria is obtained based on G&R kinetic parameters and material properties. To address the problem of the degeneracy of the linearized system about the homeostatic state mentioned above, we formulate a reduced sub-system that is shown to be exponentially stable, which enables us to extend the linear stability results to the original (nonlinear) system and rigorously prove stability properties observed in prior computational and theoretical studies.

4.2 Constrained mixture theory of growth and remodeling

The vessel wall has the ability to adapt to changes of mechanical environment to maintain a homeostatic state via vascular G&R [70, 118]. This process occurs through removal of old vascular constituents and incorporation of new constituents, which can be described by an equation of the form

$$M(t) = M(0)Q(t) + \int_0^t m(\tau)q(t-\tau)d\tau \ . \tag{4.1}$$

$M(t)$ is the mass per unit area of vascular constituents at time t. The first term on the right represents the contribution from the "initial" mass before G&R, whereas the second term on the right represents the incorporation and natural turnover of newly produced constituent. Specifically, $Q(t)$ is the remaining fraction of initial mass at the current time t, $m(\tau)$ is the mass production rate of vascular constituent at time τ, and $q(t-\tau)$ is the remaining fraction of newly produced constituent at time t.

The mass production rate $m(t)$ is assumed to depend linearly on the deviation of wall tension σ with respect to a homeostatic stress σ_h [12],

$$m(t) = M(t)\left[k_g[\sigma(t) - \sigma_h] + f_h\right] \tag{4.2}$$

where k_g is the growth feedback constant and f_h is the basal value of the mass production rate. The above growth law describes the stress-mediated feedback mechanism by which the homeostatic stress is maintained.

In the constrained mixture theory of G&R [75], the vessel wall is modeled as a membrane and treated as a constrained mixture, i.e., all vascular constituents deform together at each location. The reference configuration κ_0 for the vascular mixture corresponds to the configuration with zero transmural pressure. For any time t, the current configuration

of the mixture is denoted as $\kappa(t)$, and $\mathbf{F}(t)$ is the deformation gradient tensor mapping from κ_0 to $\kappa(t)$. However, the deformation of individual vascular constituents is computed with respect their natural configurations $\kappa_{n(\tau)}$, which depends on the time τ when the constituent was produced. The newly produced vascular constituent is deposited into the vascular mixture with pre-stretch defined by $\mathbf{G}(\tau)$, which maps from the natural configuration $\kappa_{n(\tau)}$ to the deformed configuration of the mixture at τ. Therefore, based on the relations between different configurations shown in Chapter 2 Figure 2.1, the deformation gradient tensor of the vascular constituents produced at time τ mapping from the natural configuration $\kappa_{n(\tau)}$ to the current deformed configuration $\kappa(t)$ is defined as

$$\mathbf{F}_{n(\tau)}(t) = \mathbf{F}(t)\mathbf{F}^{-1}(\tau)\mathbf{G}(\tau) \ . \tag{4.3}$$

The right Cauchy-Green deformation tensor is computed as

$$\mathbf{C}_{n(\tau)}(t) = \mathbf{F}_{n(\tau)}(t)^T\mathbf{F}_{n(\tau)}(t) \ . \tag{4.4}$$

The pre-stretch tensor $\mathbf{G}(\tau)$ is defined as the two-point tensor

$$\mathbf{G}(\tau) = G_h\mathbf{e}(\tau) \otimes \mathbf{e}_{n(\tau)} \ , \tag{4.5}$$

where $\mathbf{e}(\tau)$ is the direction of vascular constituent at time τ in the mixture configuration $\kappa(\tau)$, and $\mathbf{e}_{n(\tau)}$ is the direction of the vascular constituent produced at time τ in its natural configuration $\kappa_{n(\tau)}$. The relation between $\mathbf{e}(\tau)$ and $\mathbf{e}_{n(\tau)}$ is described by

$$\mathbf{e}_{n(\tau)} = \frac{\mathbf{G}(\tau)^{-1}\mathbf{e}(\tau)}{\|\mathbf{G}(\tau)^{-1}\mathbf{e}(\tau)\|} \ . \tag{4.6}$$

G_h is the pre-stretch of the vascular constituent when it is deposited into the mixture, and since we assume it is equal to the stretch ratio of vascular constituent in the homeostatic state, we mark it using the subscript "h".

After $\mathbf{C}_{n(\tau)}(t)$, $\mathbf{G}(\tau)$ and $\mathbf{e}_{n(\tau)}$ are defined, the stretch ratio of the vascular constituent produced at time τ with respect to its natural configuration $\kappa_{n(\tau)}$ can be computed as

$$\begin{aligned}
\lambda_{n(\tau)}(t) &= \sqrt{\mathbf{e}_{n(\tau)} \cdot \mathbf{C}_{n(\tau)}(t)\mathbf{e}_{n(\tau)}} \\
&= \left\|\mathbf{F}(t)\mathbf{F}^{-1}(\tau)\mathbf{G}(\tau)\mathbf{e}_{n(\tau)}\right\| \\
&= \left\|\mathbf{F}(t)\mathbf{F}^{-1}(\tau)G_h\left(\mathbf{e}(\tau) \otimes \mathbf{e}_{n(\tau)}\right)\mathbf{e}_{n(\tau)}\right\| \\
&= G_h\left\|\mathbf{F}(t)\mathbf{F}^{-1}(\tau)\mathbf{e}(\tau)\right\| \\
&= G_h\frac{\|\mathbf{F}(t)\mathbf{F}^{-1}(\tau)\mathbf{e}(\tau)\| \,/\, \|\mathbf{F}^{-1}(\tau)\mathbf{e}(\tau)\|}{\|\mathbf{e}(\tau)\| \,/\, \|\mathbf{F}^{-1}(\tau)\mathbf{e}(\tau)\|} \\
&= G_h\frac{\lambda(t)}{\lambda(\tau)} \ ,
\end{aligned} \tag{4.7}$$

where $\lambda(t)$ is the stretch ratio of the mixture in the direction of the vascular constituent, defined as

$$\lambda(t) = \frac{\|\mathbf{F}(t)\mathbf{F}^{-1}(\tau)\mathbf{e}(\tau)\|}{\|\mathbf{F}^{-1}(\tau)\mathbf{e}(\tau)\|} \ . \tag{4.8}$$

Based on the mass-averaged principle for a constrained mixture, the total strain energy per unit area for the mixture at current time t is

$$W(t) = \frac{M(0)}{\rho} Q(t) \hat{W}(\lambda_{n(0)}(t)) + \int_0^t \frac{m(\tau)}{\rho} q(t-\tau) \hat{W}(\lambda_{n(\tau)}(t)) d\tau \ , \tag{4.9}$$

where ρ is the volume density of the vessel wall and $\hat{W}$ denotes the strain energy per unit volume, which depends on the stretch ratio $\lambda_{n(\tau)}(t)$. The mathematical form of $\hat{W}$ is determined by the constitutive relation.

Our goal is to perform stability analysis of vascular G&R. To simplify the analysis while retaining the essential dynamics, we assume the geometry is cylindrical and deformation occurs in the radial direction. For conciseness of exposition, we assume here that vascular constituents are aligned in the circumferential direction. We later in Sec. 4.4.7, discuss the extension of this model to the case of multiple vascular constituent orientations, which is known to occur in vivo.

Under these assumptions, the stretch ratio of the mixture in the circumferential direction, $\lambda_{circ}(t)$, is obtained as

$$\lambda_{circ}(t) = \frac{\|\mathbf{F}(t)\mathbf{F}^{-1}(\tau)\mathbf{e}_{circ}\|}{\|\mathbf{F}^{-1}(\tau)\mathbf{e}_{circ}\|} = \frac{r(t)}{R} \ , \tag{4.10}$$

where $r(t)$ is the vessel radius at time t in the mixture configuration $\kappa(t)$ and R is the vessel radius in the mixture reference configuration κ_0. Hence, the stretch ratio of the vascular constituents with respect to the natural configuration is obtained as

$$\lambda_{n(\tau)}(t) = G_h \frac{\lambda_{circ}(t)}{\lambda_{circ}(\tau)} = G_h \frac{r(t)}{r(\tau)} \ . \tag{4.11}$$

For conciseness of exposition, we here assume a linearized stress-strain relation with respect the homeostatic states of the vessel wall for the purpose of stability analysis. However, since vascular material is usually considered nonlinear [61, 69], we later in Sec. 4.4.6 discuss the extension of the model for a nonlinear material model. Based on the above assumptions,

$$\hat{W}(\lambda_{n(\tau)}(t)) = \frac{1}{2} E \left[\lambda_{n(\tau)}(t) - 1\right]^2 = \frac{1}{2} E \left[G_h \frac{r(t)}{r(\tau)} - 1\right]^2 \ , \tag{4.12}$$

where $\lambda_{n(\tau)}(t) - 1$ represents the strain of the vascular constituents with respect their natural configurations $\kappa_{n(\tau)}$. Therefore (4.9) becomes

$$W(t) = \frac{M(0)}{\rho} Q(t) \frac{1}{2} E \left[G_h \frac{r(t)}{r_h} - 1\right]^2 + \int_0^t \frac{m(\tau)}{\rho} q(t-\tau) \frac{1}{2} E \left[G_h \frac{r(t)}{r(\tau)} - 1\right]^2 d\tau \ , \tag{4.13}$$

where r_h is initial homeostatic value for vessel radius. Note that for the initial mass, the stretch ratio is equal to $G_h\frac{r(t)}{r_h}$ instead of $G_h\frac{r(t)}{r(0)}$ because the initial vascular constituents are not necessarily produced at $t = 0$. Instead they are produced when the vessel radius equals to r_h since we assumed the tissue is in the homeostatic state before $t = 0$, after which point G&R occurs.

We are here interested in system stability, and hence the long-term behavior of the model. Due to natural turnover, the "initial" mass terms in both (4.1) and (4.13) rapidly decay to zero in time upon integration of the differential equations. Thus, in terms of stability analysis, we are left with

$$M(t) = \int_0^t m(\tau)q(t-\tau)d\tau \tag{4.14}$$

$$W(t) = \int_0^t \frac{m(\tau)}{\rho}q(t-\tau)\frac{1}{2}E\left[G_h\frac{r(t)}{r(\tau)} - 1\right]^2 d\tau \ . \tag{4.15}$$

Note that this simplification is mainly for the convenience of deriving corresponding differential equations. The true initial conditions for each variable will later be imposed to the resulted differential equations to account for the effect of initial mass. In the case of cylindrical geometry, the force balance equation in the circumferential direction yields

$$Pr(t) = T_\theta(t) = \frac{1}{\lambda_z(t)}\frac{\partial W(t)}{\partial \lambda_\theta(t)} \ , \tag{4.16}$$

where

$$\lambda_z = 1, \quad \lambda_\theta(t) = \frac{r(t)}{R} \ . \tag{4.17}$$

Therefore,

$$\frac{\partial W(t)}{\partial \lambda_\theta} = R\frac{\partial W(t)}{\partial r(t)} = R\int_0^t \frac{m(\tau)}{\rho}q(t-\tau)E\left[G_h\frac{r(t)}{r(\tau)} - 1\right]\frac{G_h}{r(\tau)}d\tau. \tag{4.18}$$

Substituting the above into (4.16) yields

$$Pr(t) = R\int_0^t \frac{m(\tau)}{\rho}q(t-\tau)E\left[G_h\frac{r(t)}{r(\tau)} - 1\right]\frac{G_h}{r(\tau)}d\tau \ . \tag{4.19}$$

Note that mean arterial pressure is used here and is assume to be constant. Although pressure varies over the cardiac cycle, we assume mean pressure is of most interest in the long term behavior of vascular G&R.

4.3 Converting to an ODE system

From the previous section, the time evolution of vascular growth and remodeling is described by the following equations

$$M(t) = \int_0^t m(\tau)q(t-\tau)d\tau \ , \tag{4.20}$$

$$Pr(t) = R\int_0^t \frac{m(\tau)}{\rho}q(t-\tau)E\left[G_h\frac{r(t)}{r(\tau)}-1\right]\frac{G_h}{r(\tau)}d\tau \ , \tag{4.21}$$

$$m(t) = M(t)\left[k_g[\sigma(t)-\sigma_h]+f_h\right] \ , \tag{4.22}$$

$$\sigma(t) = \frac{Pr(t)}{h(t)} \ , \tag{4.23}$$

where $h(t) = \frac{M(t)}{\rho J(t)}$ is the vessel wall thickness, and J is the determinant of the deformation gradient tensor, which is equal to $\frac{r(t)}{R}$. Since the current behavior of the system depends continuously on all past time history, the system is a continuous time-delayed system. For analysis, it is convenient if we can convert this to an ODE system depending on current states. To make this reduction possible, we assume the survival function has an exponential decay

$$q(t) = \exp(-\alpha t) \ , \tag{4.24}$$

where $\alpha > 0$ is the decaying constant. This implies that the rate of decay of the constituent is proportional to its current value as

$$\dot{q}(t) = -\alpha q(t). \tag{4.25}$$

To proceed we differentiate (4.20) with respect to t

$$\dot{M}(t) = m(t) - \alpha\int_0^t m(\tau)q(t-\tau)d\tau \tag{4.26}$$

$$= m(t) - \alpha M(t). \tag{4.27}$$

Substituting in (4.22) yields

$$\dot{M}(t) = M(t)k_g\left[\sigma(t)-\sigma_h\right] + M(t)\left[f_h-\alpha\right]. \tag{4.28}$$

Since f_h is the basal value of the mass production rate, it should balance with the natural decay of constituents caused by the survival function $q(t)$. Thus we require that $f_h = \alpha$ and subseqently

$$\dot{M}(t) = M(t)k_g\left[\sigma(t)-\sigma_h\right] \ . \tag{4.29}$$

Now taking the time derivative of (4.21) yields

$$\begin{aligned} P\dot{r}(t) &= R\left[\frac{m(t)}{\rho}E\left(G_h-1\right)\frac{G_h}{r(t)}\right. \\ &\quad + \int_0^t \frac{m(\tau)}{\rho}q(t-\tau)E\,G_h\frac{\dot{r}(t)}{r(\tau)}\frac{G_h}{r(\tau)}d\tau \\ &\quad \left.-\alpha\int_0^t \frac{m(\tau)}{\rho}q(t-\tau)E\left[G_h\frac{r(t)}{r(\tau)}-1\right]\frac{G_h}{r(\tau)}d\tau\right] . \end{aligned} \tag{4.30}$$

The last term in the above equation is just $-\alpha Pr(t)$, and defining an extended state variable

$$y(t) = R\int_0^t \frac{m(\tau)}{\rho}q(t-\tau)E\frac{G_h^2}{r^2(\tau)}d\tau \tag{4.31}$$

yields

$$\dot{r}(t) = \frac{m(t)}{r(t)}\frac{RE\left[G_h-1\right]G_h}{P\rho} + \frac{1}{P}y(t)\dot{r}(t) - \alpha r(t) . \tag{4.32}$$

Take time derivative of (4.31), we obtain the ODE characterizing dynamics of $y(t)$

$$\dot{y}(t) = k_2\frac{m(t)}{r^2(t)} - \alpha y(t) , \tag{4.33}$$

where $k_2 = \frac{G_h^2 ER}{\rho}$. The extended state y represents the generalized stiffness of the vascular mixture, as explained later in the Discussion section.

Based on (4.22), (4.23), (4.29), (4.32) and (4.33), the system of equations for vascular growth can now be written as

$$\dot{M}(t) = M(t)k_g\left[\sigma(t)-\sigma_h\right] \tag{4.34}$$

$$\dot{r}(t) = \frac{1}{k(t)}\left[\alpha r(t) - \frac{m(t)}{r(t)}k_1\right] \tag{4.35}$$

$$\dot{y}(t) = k_2\frac{m(t)}{r^2(t)} - \alpha y(t) \tag{4.36}$$

$$m(t) = M(t)\left[k_g\left[\sigma(t)-\sigma_h\right]+f_h\right] \tag{4.37}$$

$$\sigma(t) = \frac{\rho P r(t)^2}{M(t)R} \tag{4.38}$$

where $k(t) = \frac{1}{P}y(t) - 1$, $k_1 = \frac{RE[G_h-1]G_h}{P\rho}$ and $f_h = \alpha$.

4.4 Stability analysis of the ODE system

4.4.1 Linearization of state equations

The stability of vascular growth is characterized by the stability of the ODE system we obtained in previous section. To analyze its stability, we examine the nature of the linearized system about the homeostatic state. Namely, we assume the vessel is initially in its

homeostatic state before G&R is introduced by whatever cause. Mass density and vessel radius in the initial homeostatic state are denoted M_h and r_h respectively. Strictly speaking, as shown later, there is no "homeostatic state" for mass density $M(t)$ and $r(t)$ because asymptotic stability does not hold for $M(t)$ and $r(t)$. However, for convenience, we use the term "homeostatic state" to denote the asymptotic values M_h and r_h.

Based on (4.38), the homeostatic value of circumferential stress σ_h is

$$\sigma_h = \frac{\rho P r_h^2}{M_h R} \,. \tag{4.39}$$

Substituting homeostatic values into (4.32) yields

$$\frac{\rho P r_h}{M_h} = E\left[G_h - 1\right] \,. \tag{4.40}$$

Combining (4.39) and (4.40) and observing $G_h = \frac{r_h}{R}$, we obtain an alternate expression for σ_h

$$\sigma_h = E\left[G_h - 1\right] G_h \,. \tag{4.41}$$

Similarly, substituting homeostatic values into (4.31) yields the homeostatic value for the extended state $y(t)$

$$y_h = \frac{R E G_h^2 M_h}{\rho r_h^2} \,. \tag{4.42}$$

We next consider perturbation of the system around the homeostatic values above

$$\begin{aligned} M(t) &= M_h + \Delta M(t) && (4.43)\\ r(t) &= r_h + \Delta r(t) && (4.44)\\ y(t) &= y_h + \Delta y(t) && (4.45)\\ \sigma(t) &= \sigma_h + \Delta\sigma(t) && (4.46) \end{aligned}$$

with

$$\frac{\Delta M}{M_h},\ \frac{\Delta r}{r_h},\ \frac{\Delta y}{y_h},\ \frac{\Delta\sigma}{\sigma_h} \ll 1 \,. \tag{4.47}$$

To obtain the linearized equations, it is convenient to first obtain the first order approximation of $\Delta\sigma$

$$\begin{aligned} \Delta\sigma(t) &= \sigma(t) - \sigma_h \\ &= \frac{\rho P}{R}\left[\frac{[r_h + \Delta r]^2}{M_h + \Delta M} - \frac{r_h^2}{M_h}\right] \\ &\approx \frac{\rho P}{R}\left[\frac{2r_h}{M_h}\Delta r - \frac{r_h^2}{M_h^2}\Delta M\right] \,. && (4.48) \end{aligned}$$

Therefore, the linearized state equation for mass density $M(t)$ is obtained as

$$\begin{aligned}\Delta\dot{M} &= \dot{M} = Mk_g\Delta\sigma \\ &\approx [M_h + \Delta M]k_g\frac{\rho P}{R}\left[\frac{2r_h}{M_h}\Delta r - \frac{r_h^2}{M_h^2}\Delta M\right] \\ &\approx k_g\frac{\rho P}{R}\left[2r_h\Delta r - \frac{r_h^2}{M_h}\Delta M\right] . \end{aligned} \tag{4.49}$$

Similarly, we can obtain the linearized state equations for vessel radius $r(t)$ and generalized stiffness $y(t)$ as

$$\Delta\dot{r} \approx \frac{1}{k_h}\left[\left[2\alpha - \frac{2k_g r_h^2\rho P}{RM_h}\right]\Delta r + \left[-\frac{\alpha r_h}{M_h} + \frac{k_g r_h^3\rho P}{M_h^2 R}\right]\Delta M\right] \tag{4.50}$$

$$\Delta\dot{y} \approx -\frac{2k_2 M_h}{r_h^3}\left[\alpha - \frac{k_g\rho P r_h^2}{RM_h}\right]\Delta r - \frac{k_2}{r_h^2}\left[\alpha - \frac{k_g\rho P r_h^2}{RM_h}\right]\Delta M - \alpha\Delta y \tag{4.51}$$

where $k_h = \frac{1}{G_h - 1}$ and $k_2 = \frac{G_h^2 ER}{\rho}$.

Equations (4.49)–(4.51) describe the time evolution of the linearized variables $(\Delta M, \Delta r, \Delta y)$. We will first consider the linear stability of the subsystem for $(\Delta M, \Delta r)$. This is reasonable since the dynamics of Δr and ΔM are decoupled from the dynamics of Δy. Also, the time evolution of mass density M and vessel radius r are of paramount interest.

Based on (4.49) and (4.50), the linearized state equations for Δr and ΔM become

$$\begin{bmatrix} \Delta\dot{r} \\ \Delta\dot{M} \end{bmatrix} = \begin{bmatrix} A & B \\ C & D \end{bmatrix} \times \begin{bmatrix} \Delta r \\ \Delta M \end{bmatrix} \tag{4.52}$$

where

$$A = \frac{1}{k_h}\left[2\alpha - \frac{2k_g r_h^2\rho P}{RM_h}\right] , \tag{4.53}$$

$$B = \frac{1}{k_h}\left[-\frac{\alpha r_h}{M_h} + \frac{k_g r_h^3\rho P}{M_h^2 R}\right] , \tag{4.54}$$

$$C = \frac{2k_g\rho P r_h}{R} , \tag{4.55}$$

$$D = -\frac{k_g\rho P r_h^2}{RM_h} . \tag{4.56}$$

4.4.2 Stability of the linearized state equations

To determine whether G&R is stable, we need to first find the eigenvalues of system matrix. Let the characteristic polynomial for the system be equal to zero

$$\begin{vmatrix} A-\lambda & B \\ C & D-\lambda \end{vmatrix} = \lambda^2 - [A+D]\lambda + [AD - BC] = 0 . \tag{4.57}$$

It can be verified that $AD - BC = 0$ based on (4.53)–(4.56). Therefore, the corresponding eigenvalues are

$$\lambda_1 = A + D, \quad \lambda_2 = 0 \, . \tag{4.58}$$

This means $[\Delta r, \Delta M] = [0, 0]$ is a **degenerate** fixed point of the linearized system.

Theorem 4.4.1. (Neutrally Stable Fixed Point) *Consider an autonomous dynamical system* $\dot{\mathbf{x}} = \mathbf{A}\mathbf{x}$ *with system matrix*

$$\mathbf{A} = \begin{bmatrix} A & B \\ C & D \end{bmatrix} \tag{4.59}$$

whose eigenvalues are λ_1 *and* λ_2*. Let* $\tau = \mathrm{Tr}(\mathbf{A}) = A + D$*,* $\Delta = \det(\mathbf{A}) = AD - BC$*. If*

$$\Delta = 0, \quad \tau < 0 \tag{4.60}$$

then $\lambda_1 < 0$ *and* $\lambda_2 = 0$ *and there exists a line of neutrally stable non-isolated* ***degenerate*** *fixed points passing through* $\mathbf{x} = \mathbf{0}$*. A neutrally stable fixed point denotes a fixed point which is Lyapunov stable but not attracting.*

Based on Theorem 4.4.1, the neutrally stabilizing condition for the linearized system (4.52) at the fixed point $(\Delta r, \Delta M) = (0, 0)$ is $A + D < 0$, i.e.

$$k_g > \frac{\alpha R M_h}{\rho P r_h^2} \left[\frac{1}{1 + \frac{E M_h}{2 \rho P r_h}} \right] \, . \tag{4.61}$$

However, since the fixed point is degenerate, stability of the hemostatic state for the nonlinear system cannot be inferred [121].

4.4.3 Avoiding the degeneracy condition

In order to avoid the degenerate fixed point problem encountered above, the 3-state linearized system is reconsidered

$$\frac{d}{dt} \begin{bmatrix} \Delta r \\ \Delta M \\ \Delta y \end{bmatrix} = \begin{bmatrix} \frac{1}{k_h} \left[\alpha - \frac{k_g \rho P r_h^2}{R M_h} \right] \left[2\Delta r - \frac{r_h}{M_h} \Delta M \right] \\ \frac{k_g \rho P r_h}{R} \left[2\Delta r - \frac{r_h}{M_h} \Delta M \right] \\ -\frac{k_2 M_h}{r_h^3} \left[\alpha - \frac{k_g \rho P r_h^2}{R M_h} \right] \left[2\Delta r - \frac{r_h}{M_h} \Delta M \right] - \alpha \Delta y \end{bmatrix} \, . \tag{4.62}$$

It can be observed that there is a linear relation between derivatives of Δr and ΔM,

$$\dot{\Delta r} = B_1 \dot{\Delta M} \tag{4.63}$$

where

$$B_1 = \frac{\left[\alpha - \frac{k_g \rho P r_h^2}{R M_h} \right] R}{k_h k_g \rho P r_h} \, , \tag{4.64}$$

which in fact is responsible for the degeneracy observed above. Note that B_1 is positive if

$$k_g < \frac{\alpha R M_h}{\rho P r_h^2} \ . \tag{4.65}$$

We can now integrate the derivative relation (4.63) from 0 to t to obtain

$$\Delta r(t) = B_1 \Delta M(t) + B_2 \ , \tag{4.66}$$

where constant B_2 only depends on initial conditions

$$B_2 = \Delta r(0) - B_1 \Delta M(0) \ . \tag{4.67}$$

By eliminating Δr using the relations above, the 3-state system $(\Delta r, \Delta M, \Delta y)$ is reduced to a 2-state system of $(\Delta M, \Delta y)$

$$\frac{d}{dt} \begin{bmatrix} \Delta M \\ \Delta y \end{bmatrix} = \begin{bmatrix} \frac{k_g \rho P r_h}{R} \left[2B_1 - \frac{r_h}{M_h} \right] \Delta M + \frac{2 k_g \rho P r_h}{R} B_2 \\ B_3 \Delta \dot{M} - \alpha \Delta y \end{bmatrix} \ , \tag{4.68}$$

where the constant B_3 is defined as

$$B_3 = - \frac{k_2 \left[\alpha - \frac{k_g \rho P r_h^2}{R M_h} \right] M_h R}{k_g \rho P r_h^2} \ . \tag{4.69}$$

The linear system (4.68) is nonhomogeneous because of the constant term $\frac{2 k_g \rho P r_h}{R} B_2$ on the right hand side of the first equation. It can be shown that the above nonhomogeneous system is neutrally stable in the sense that the state variables $(\Delta M, \Delta y)$ remain bounded, while exponential stability cannot be obtained due to the nonhomogeneous term. However, in order to extend the stability conclusion from the linearized system to the original nonlinear system, exponential stability of the linearized system should be obtained. Therefore, we homogenize the linear system by taking the time derivative of the first equation in (4.68), yielding a homogeneous 2-state system for $(\Delta \dot{M}, \Delta y)$ as

$$\frac{d}{dt} \begin{bmatrix} \Delta \dot{M} \\ \Delta y \end{bmatrix} = \begin{bmatrix} \frac{k_g \rho P r_h}{R} \left[2B_1 - \frac{r_h}{M_h} \right] & 0 \\ B_3 & -\alpha \end{bmatrix} \times \begin{bmatrix} \Delta \dot{M} \\ \Delta y \end{bmatrix} \ . \tag{4.70}$$

The eigenvalues for the system matrix in (4.70) are

$$\lambda_1 = \frac{k_g \rho P r_h}{R} \left[2B_1 - \frac{r_h}{M_h} \right], \quad \lambda_2 = -\alpha \ . \tag{4.71}$$

Therefore the linear system is exponentially stable if and only if

$$\frac{k_g \rho P r_h}{R} \left[2B_1 - \frac{r_h}{M_h} \right] < 0, \quad \alpha > 0 \tag{4.72}$$

By substituting (4.64) in to the inequalities above, the exponentially stability condition is given by

$$k_g > \frac{\alpha R M_h}{\rho P r_h^2}\left[\frac{1}{1+\frac{EM_h}{2\rho P r_h}}\right] \triangleq k_{cr}, \qquad \alpha > 0\ , \tag{4.73}$$

where k_{cr} denotes the critical value for the growth feedback constant k_g to ensure stability.

Theorem 4.4.2. (Lyapunov's Indirect Method) *Consider an autonomous nonlinear system* $\dot{\mathbf{x}} = \mathbf{f}(\mathbf{x})$ *with linearized system about* $\mathbf{x} = \mathbf{0}$ *(without loss of generality) as* $\dot{\mathbf{x}} = \mathbf{A}\mathbf{x}$*, where*

$$\mathbf{A} = \nabla \mathbf{f}(\mathbf{x})|_{\mathbf{x}=\mathbf{0}} \tag{4.74}$$

is the system matrix for the linear system. If the eigenvalues of matrix A satisfy

$$Re(\lambda_i) < 0, \quad \forall\ i = 1, 2, \ldots\ , \tag{4.75}$$

(i.e the linearized system is exponentially stable), then the nonlinear system $\dot{\mathbf{x}} = \mathbf{f}(\mathbf{x})$ *is locally exponentially stable about* $\mathbf{x} = \mathbf{0}$*.*

Based on Theorem 4.4.2, for the nonlinear system (4.34)–(4.38) describing vascular growth, the 2-state system $(\Delta\dot{M}, \Delta y)$ is locally exponentially stable, i.e., locally $\dot{M} \to 0$ and $y \to y_h$ exponentially.

It can be noted that the stabilizing condition (4.73) for $(\Delta\dot{M},\ \Delta y)$ is the same as the one in (4.61) derived from the degenerate linear system for $(\Delta M,\ \Delta r)$. (The additional criterion $\alpha > 0$ from considering Δy is automatically satisfied by definition.) However, the above analysis is necessary to establish *exponential stability* for the linear system, which enables the extrapolation of the stability properties to the original nonlinear system. On the other hand, we would like to establish the behavior of the mass density M, as opposed to its time derivative $\dot{M}$. This can be achieved however by noticing that, due to local exponential stability of $\Delta\dot{M}$, there exist constants $a > 0$ and $b > 0$ such that

$$\|\Delta\dot{M}\| \le be^{-at}, \quad \forall\ t > 0 \tag{4.76}$$

within a local neighborhood. To obtain a norm estimation of mass density $M(t)$, we first integrate $\Delta\dot{M}$ from 0 to t

$$\Delta M(t) = \Delta M(0) + \int_0^t \Delta\dot{M} dt\ . \tag{4.77}$$

Taking the norm for the above equation and applying the triangle inequality gives

$$\begin{aligned}
\|\Delta M(t)\| &\le \|\Delta M(0)\| + \int_0^t \|\Delta\dot{M}\| dt \\
&\le \|\Delta M(0)\| + b\int_0^t e^{-at} dt \\
&= \|\Delta M(0)\| + b\,\frac{1-e^{-at}}{a} \\
&\le \|\Delta M(0)\| + \frac{b}{a}\ .
\end{aligned} \tag{4.78}$$

Reapplying the triangle inequality, an estimation of the norm of $M(t)$ for the nonlinear system can be obtained as

$$\|M(t)\| = \|M_h + \Delta M(t)\| \leq \|M_h\| + \|\Delta M(t)\| \leq \|M_h\| + \|\Delta M(0)\| + \frac{b}{a} \leq C < \infty \ . \quad (4.79)$$

Similarly, if we construct the 2-state system of $(\dot{\Delta r}, \Delta y)$ and apply the same analysis above, we can obtain

$$\|r(t)\| < \infty \quad (4.80)$$

under the same stabilizing condition given by (4.73).

4.4.4 Asymptotic stability for wall tension $\sigma(t)$

By taking the time derivative of (4.38), we can obtain the linearized ODE for the time evolution of wall tension deviation

$$\begin{aligned} \frac{d}{dt}\Delta\sigma(t) &= \frac{\rho P}{R}\left[\frac{2r(t)}{M(t)}\dot{r}(t) - \frac{r^2(t)}{M^2(t)}\dot{M}(t)\right] \\ &\approx \left[\frac{1}{k_h}\left[2\alpha - \frac{2k_g r_h^2 \rho P}{RM_h}\right] - \frac{k_g \rho P r_h^2}{RM_h}\right]\Delta\sigma \\ &= [A + D]\Delta\sigma \ , \end{aligned} \quad (4.81)$$

which implies that stability criteria (4.73) also ensures the exponential stability for wall tension deviation, i.e.

$$\lim_{t\to\infty} \Delta\sigma(t) = 0 \ . \quad (4.82)$$

4.4.5 Summary of stability conclusions

When the following stability conditions are satisfied,

$$k_g > \frac{\alpha R M_h}{\rho P r_h^2}\left[\frac{1}{1 + \frac{EM_h}{2\rho P r_h}}\right] \triangleq k_{cr}, \qquad \alpha > 0$$

the states $r(t)$, $M(t)$, $y(t)$ and $\sigma(t)$ for the nonlinear system (4.34–4.36) have the following stability behavior about the homeostatic states

$$\begin{aligned} \|r(t)\| < \infty &\Rightarrow r(t) \text{ is neutrally stable ;} \\ \|M(t)\| < \infty &\Rightarrow M(t) \text{ is neutrally stable ;} \\ y(t) \to y_h &\Rightarrow y(t) \text{ is asymptotically stable ;} \\ \sigma(t) \to \sigma_h &\Rightarrow \sigma(t) \text{ is asymptotically stable ,} \end{aligned} \quad (4.83)$$

Thus, stability analysis shows that even when the stability criteria (4.73) is satisfied, only σ and y will converge to corresponding homeostatic values while M and r will only stay

bounded but not necessarily converge to the original homeostatic values. This matches observations in [13, 134] that in stable aneurysm expansion cases, only wall tension σ is able to recover the homeostatic value, while the geometry and mass density do not return to the original homeostatic states.

4.4.6 Extension to nonlinear constitutive relations

A linear constitutive relation for the vessel wall was considered above. Alternatively, we here assume a nonlinear Fung-type exponential constitutive relation, i.e. the strain energy density function is given by

$$\hat{W}(\lambda_{n(\tau)}(t)) = \frac{c_2}{4c_3}\left\{\exp\left[c_3\left(\lambda_{n(\tau)}(t)^2-1\right)^2\right]\right\} . \tag{4.84}$$

This type of constitutive relation is commonly used to describe the mechanical properties of vascular constituents (e.g. collagen and smooth muscle fibers). In the homeostatic state, the stretch ratio of the fiber, $\lambda_{n(\tau)}(t)$, is equal to G_h. Therefore, it can be represented as

$$\lambda_{n(\tau)}(t) = G_h + \Delta\lambda , \tag{4.85}$$

where $\Delta\lambda$ is a small perturbation for the stretch ratio. Substituting the above equation into the nonlinear constitutive relation (4.84) yields

$$\begin{aligned}\hat{W}(\lambda_{n(\tau)}(t)) &= \frac{c_2}{4c_3}\left\{\exp\left[c_3\left([G_h+\Delta\lambda]^2-1\right)^2\right]\right\} \\ &= \frac{c_2}{4c_3}\left\{\exp(c_3\left[G_h^2-1\right])-1\right\} + c_2\exp(c_3\left[G_h^2-1\right])G_h\left[G_h^2-1\right]\Delta\lambda \\ &\quad + c_2\exp(c_3\left[G_h^2-1\right])G_h^2(\Delta\lambda)^2 + \mathcal{O}((\Delta\lambda)^3) .\end{aligned} \tag{4.86}$$

The relation between $\Delta\lambda$ and the strain in the fiber direction is

$$\Delta\lambda = \lambda_{n(\tau)}(t) - G_h = (1+\epsilon) - G_h = \epsilon - (G_h - 1) , \tag{4.87}$$

where ϵ is the fiber strain. Using the above, we can rewrite the strain energy density function in terms of ϵ,

$$\begin{aligned}\hat{W}(\lambda_{n(\tau)}(t)) \approx & \frac{c_2}{4c_3}\left\{\exp(c_3\left[G_h^2-1\right])-1\right\} \\ & + c_2\exp(c_3\left[G_h^2-1\right])G_h\left[G_h^2-1\right](\epsilon-(G_h-1)) \\ & + c_2\exp(c_3\left[G_h^2-1\right])G_h^2(\epsilon-(G_h-1))^2 \\ = & \Lambda_1 + R_0\epsilon + \frac{1}{2}E_{tan}\epsilon^2 ,\end{aligned} \tag{4.88}$$

where

$$\begin{aligned}
\Lambda_1 &= \frac{c_2}{4c_3}\left\{\exp(c_3[G_h^2-1])-1\right\} \\
&\quad +c_2\left\{\exp(c_3[G_h^2-1])-1\right\}G_h(G_h-1)^2\ , \qquad (4.89)\\
R_0 &= c_2\left\{\exp(c_3[G_h^2-1])-1\right\}(-G_h^3+G_h^2-G_h)\ , \qquad (4.90)\\
E_{tan} &= 2c_2\left\{\exp(c_3[G_h^2-1])-1\right\}G_h^2\ . \qquad (4.91)
\end{aligned}$$

Substituting (4.88) into the force balance equation (4.16) yields

$$\begin{aligned}
Pr(t) =& R\frac{\partial W(t)}{\partial r(t)} \\
=& R\int_0^t \frac{m(\tau)}{\rho}q(t-\tau)\left\{R_0\frac{\partial \epsilon}{\partial r(t)}+E_{tan}\epsilon\frac{\partial \epsilon}{\partial r(t)}\right\}d\tau \\
=& R\int_0^t \frac{m(\tau)}{\rho}q(t-\tau)\left\{E_{tan}\frac{G_h^2}{r(\tau)^2}r(t)-(E_{tan}-R_0)\frac{G_h}{r(\tau)}\right\}d\tau\ . \qquad (4.92)
\end{aligned}$$

Taking time derivative of the above equation yields

$$\begin{aligned}
P\dot{r}(t) =& R\left\{\frac{m(t)}{\rho}\left[E_{tan}\frac{G_h^2}{r(t)}-(E_{tan}-R_0)\frac{G_h}{r(t)}\right]\right. \\
&+\int_0^t \frac{m(\tau)}{\rho}q(t-\tau)E_{tan}\frac{G_h^2}{r(\tau)^2}\dot{r}(t)d\tau \\
&\left.-\alpha\int_0^t \frac{m(\tau)}{\rho}q(t-\tau)\left[E_{tan}\frac{G_h^2}{r(\tau)^2}r(t)-(E_{tan}-R_0)\frac{G_h}{r(\tau)}\right]d\tau\right\}\ . \qquad (4.93)
\end{aligned}$$

As before, if we define a similar extended state variable

$$y(t) = R\int_0^t \frac{m(\tau)}{\rho}q(t-\tau)E_{tan}\frac{G_h^2}{r(\tau)^2}d\tau\ , \qquad (4.94)$$

the differential equation for radius $r(t)$ can be obtained as

$$\dot{r}(t) = \frac{m(t)}{r(t)}\frac{RE_{tan}\left[G_h-\frac{E_{tan}-R_0}{E_{tan}}\right]G_h}{P\rho}+\frac{1}{P}y(t)\dot{r}(t)-\alpha r(t)\ , \qquad (4.95)$$

which is similar to the differential equation for the linear material (4.32). After this, we can follow a parallel path to the stability analysis presented in the sections above and obtain a similar stabilizing criteria for nonlinear material

$$k_g > \frac{\alpha R M_h}{\rho P r_h^2}\left[\frac{1}{1+\frac{E_{tan}M_h}{2\rho P r_h}}\right] \triangleq k_{cr}, \qquad \alpha > 0\ .$$

Note that the effective difference between the stabilizing criteria for a linear material versus a nonlinear material comes by replacing the material stiffness E with E_{tan}.

4.4.7 Extension to multiple component directions

Here we extend our framework from a single constituent model to a multiple constituent model were constituents are aligned in different directions. Assume that each constituent family is indexed by k and the angle between the constituent family direction and the circumferential directions is defined as $\alpha_k \in \left[-\frac{\pi}{2}, \frac{\pi}{2}\right]$. Since our model only considers the radial expansion of the vessel wall, we seek an effective stiffness caused by the multiple constituents. Assume the strain in the circumferential direction is ϵ. Due to the fact that all constituents deform together in a constrained mixture model, the strain in vascular constituent family k can be computed as

$$\epsilon_k = \frac{\sqrt{(1+\epsilon)^2 + \tan^2\alpha_k} - \sqrt{1+\tan^2\alpha_k}}{\sqrt{1+\tan^2\alpha_k}} = \frac{\epsilon}{1+\tan^2\alpha_k} + \mathcal{O}(\epsilon^2)\ . \tag{4.96}$$

The stress in the constituent family k can be computed as

$$\sigma_k = E\epsilon_k \approx \frac{E\epsilon}{1+\tan^2\alpha_k}, \tag{4.97}$$

Therefore, force in the vascular constituent family k is

$$f_k = A_k E\epsilon_k\ , \tag{4.98}$$

where A_k is the cross-section area of the constituent family k. We can represent the multiple constituents by an effective constituent in the circumferential direction by the following equivalency relation

$$\sum_k (A_k E\epsilon_k)\cos\alpha_k = \sum_k f_k \cos\alpha_k = f = E_e\left(\sum_k A_k\right)\epsilon. \tag{4.99}$$

Therefore, an effective stiffness E_e can be obtained as

$$E_e = \frac{\sum_k \frac{A_k\cos\alpha_k}{1+\tan^2\alpha_k}}{\sum_k A_k} E\ . \tag{4.100}$$

Because A_k is proportional to the mass density of each constituent family, M_k, the effective stiffness can be rewritten as

$$E_e = \frac{\sum_k \frac{M_k\cos\alpha_k}{1+\tan^2\alpha_k}}{\sum_k M_k} E\ . \tag{4.101}$$

After this point, we can apply the same formulas derived for the single constituent model and obtain similar stability conclusions.

4.5 Numerical Experiments

The stability analysis and derived stability criteria presented above are, strictly speaking, applicable in the case of infinitesimal perturbations to the system. To understand how well these theoretical results hold in the context of large deviations, we must perform numerical integration of the original system. Therefore, in this section we simulate the vascular expansion based on the system of nonlinear differential equations (4.34–4.38). Material constants and geometric constants used in the simulations are listed in Table 4.1. All simulations were done within *Simulink*. In all simulations, pathological G&R is triggered by introducing 50% initial uniform mass loss of vascular constituents as in [13, 41].

Based on the stabilizing criteria (4.73) and the given G&R parameters listed in Table 4.1, the critical value of the growth feedback constant is $k_{cr} = 2.1 \times 10^{-6}$. The stabilizing condition (4.73) indicates that radial expansion is stable when $k_g > k_{cr}$ while the radial expansion is unstable when $k_g \leq k_{cr}$. To test this, four scenarios of pathological G&R are simulated with different values of the growth feedback constant: Case (1) $k_g = 1.5 \times 10^{-6}$, Case (2) $k_g = 3.0 \times 10^{-6}$, Case (3) $k_g = 5.0 \times 10^{-6}$, Case (4) $k_g = 7.0 \times 10^{-6}$. For these four cases, the time evolution of the state variables for vascular expansion, mass density $M(t)$, vessel radius $r(t)$, generalized stiffness $y(t)$ and wall tension $\sigma(t)$, were recorded and plotted in Figure 4.1.

The simulation results show that when $k_g > k_{cr}$ (Case 2–4), vascular expansion is stable. In these three stable cases, we observed that generalized stiffness $y(t)$ and wall tension $\sigma(t)$ converge to the corresponding homeostatic states asymptotically while mass density $M(t)$ and vessel radius $r(t)$ only exhibit neutral stability, i.e., the values of the states remain bounded. In Case 1, where $k_g < k_{cr}$, vessel radius $r(t)$ and wall tension $\sigma(t)$ both increase unboundedly, which indicates unstable vascular expansion. Also observed is that the larger the value of k_g, the faster the states converge to the steady states.

We also simulated four cases with increased stiffness E to study the influence of vessel stiffness on vascular expansion. The value of stiffness was increased to $E = 3.8 \times 10^6$ Pa while all other parameters remained unchanged. For this value of E, the critical value for the growth feedback constant is $k_{cr} = 1.0 \times 10^{-6}$. Four scenarios were considered, with Case (1) $k_g = 1.5 \times 10^{-6}$, Case (2) $k_g = 3.0 \times 10^{-6}$, Case (3) $k_g = 5.0 \times 10^{-6}$, Case (4) $k_g = 7.0 \times 10^{-6}$, and the time course of the four state variables are plotted in Figure 4.2. For the elevated value of stiffness E, all four cases satisfy the stabilizing condition $k_g > k_{cr}$ and all four cases obtain stable vascular expansion, including the case of $k_g = 1.5 \times 10^{-6}$ that was unstable for the normal value of stiffness E.

Lastly, we simulated four cases considering an increase of vascular constituent decay constant $\alpha = 4.6$. This corresponds to an increase of turnover rate of vascular constituents, e.g., collagen and smooth muscle. For this scenario, the critical value for the growth feedback constant was $k_{cr} = 4.1 \times 10^{-6}$. The time evolution of the four state variables for Case (1) $k_g = 1.5 \times 10^{-6}$, Case (2) $k_g = 3.0 \times 10^{-6}$, Case (3) $k_g = 5.0 \times 10^{-6}$, Case (4) $k_g = 7.0 \times 10^{-6}$ are plotted in Figure 4.3. With the elevated value of the decaying constant, Cases (3) and (4) satisfies the stabilizing criteria while Cases (1) and (2) do not. Figure 4.3 shows that

Table 4.1: Mechanical, geometric and G&R kinetic constants [11, 138]

$\alpha = 2.3$	$E = 1.9 \times 10^6 Pa$	$P = 13332\ Pa$	$r_h = 0.0075\ m$
$G_h = 1.05$	$M_h = 1.0904\ kg/m^2$	$\sigma_h = 1.01 \times 10^5\ Pa$	$\rho = 1050\ kg/m^3$

only in Cases (3) and (4), vessel radius remains bounded and wall tension converges to the homeostatic value, while in Case (1) and (2) G&R results in unbounded vascular expansion. Case (2), which is stable under the normal conditions, is destabilized due to elevated decaying constant α.

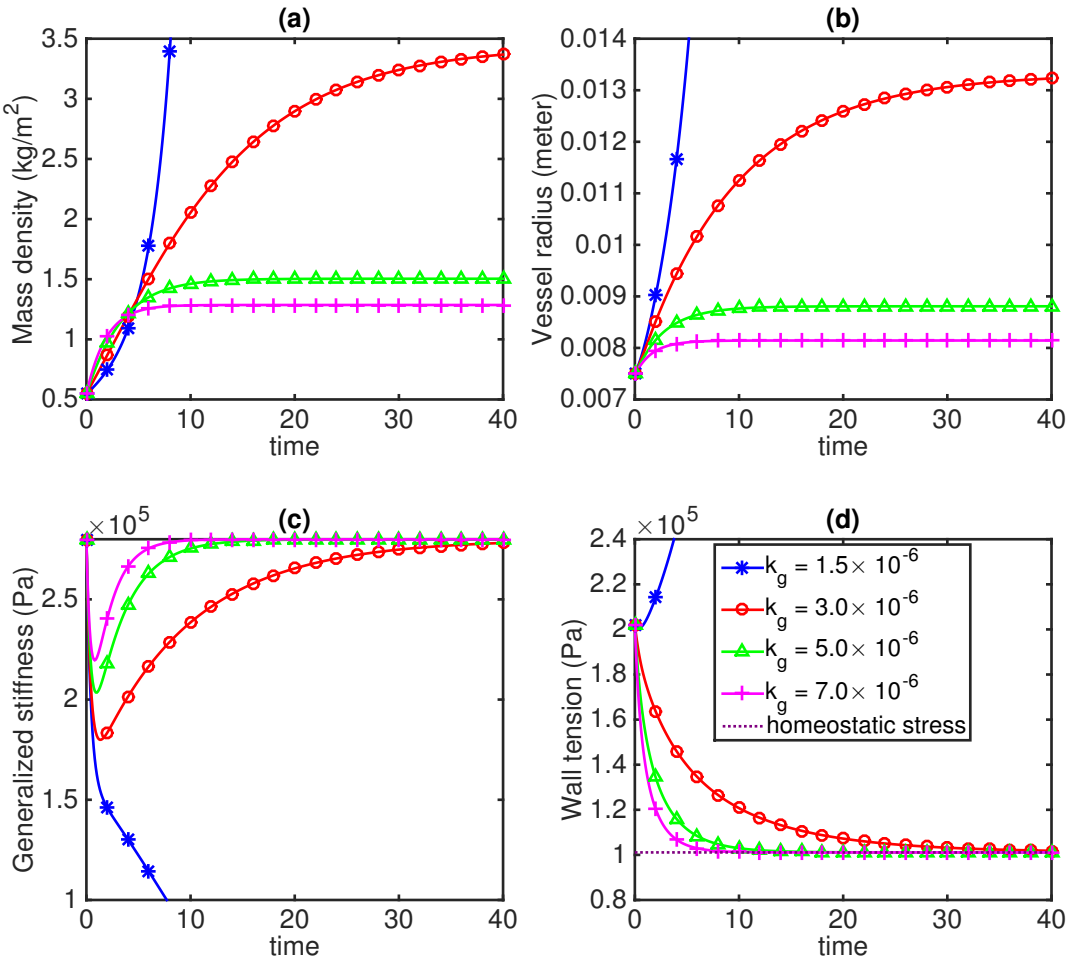

Figure 4.1: Time evolution of vessel properties ($M(t)$, $r(t)$, $y(t)$ and $\sigma(t)$) using various values of growth feedback constant k_g from solving the nonlinear evolution equations. The corresponding critical value for the growth feedback constant is $k_{cr} = 2.1 \times 10^{-6}$.

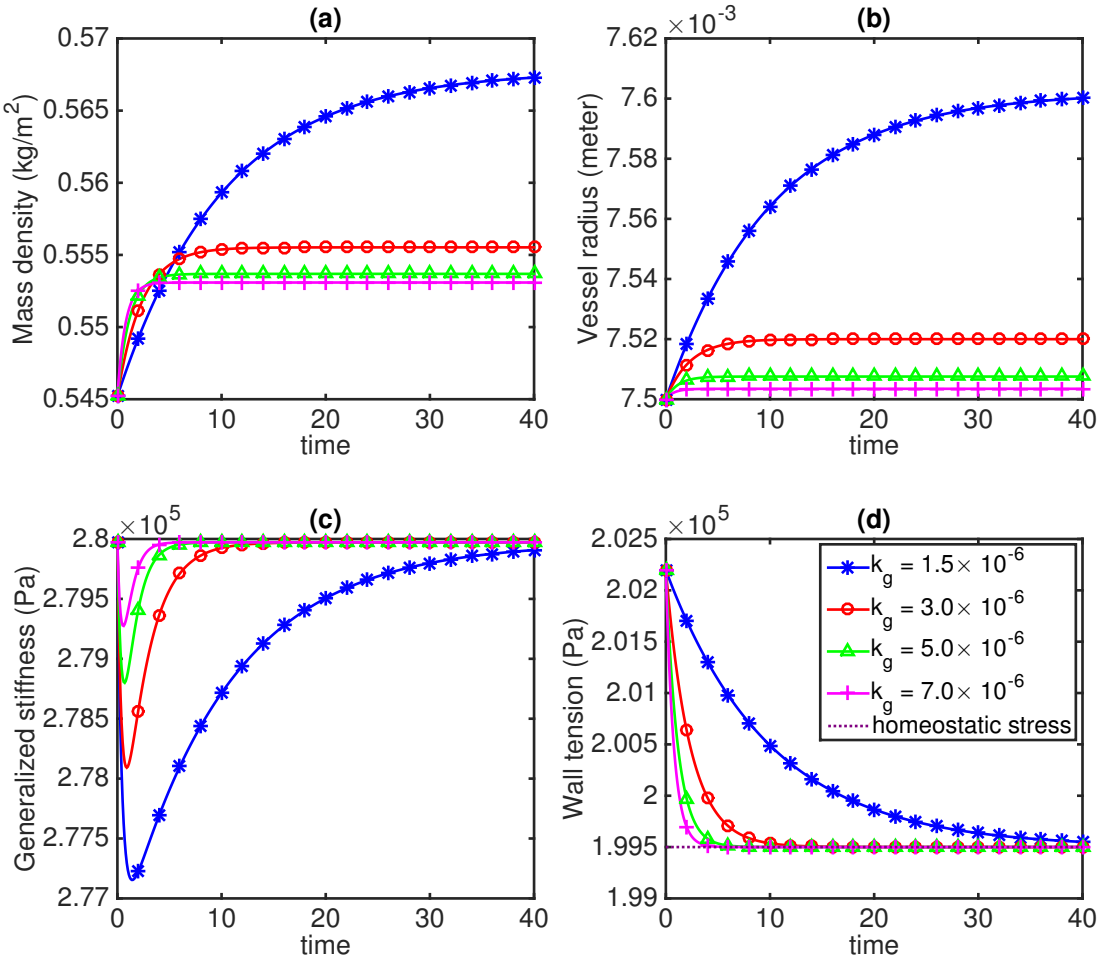

Figure 4.2: Time evolution of vessel properties ($M(t)$, $r(t)$, $y(t)$ and $\sigma(t)$) using various values of growth feedback constant k_g for increased arterial stiffness $\mathbf{E}$. The corresponding critical value for the growth feedback constant is $k_{cr} = 1.0 \times 10^{-6}$.

4.6 Discussion

While prior works [41, 7, 107, 134] have focused on computationally investigating vascular expansion based on the constrained mixture theory of vascular G&R, we herein provide an analytical study of the stability properties of this model. Under appropriate assumptions, the constrained mixture model was used to develop a nonlinear ODE system governing vascular growth, and stability criteria (4.73) were derived for growth about the homeostatic state in terms of G&R kinetic parameters, geometric quantities and material properties.

To obtain stability conclusions for the nonlinear system about the homeostatic state,

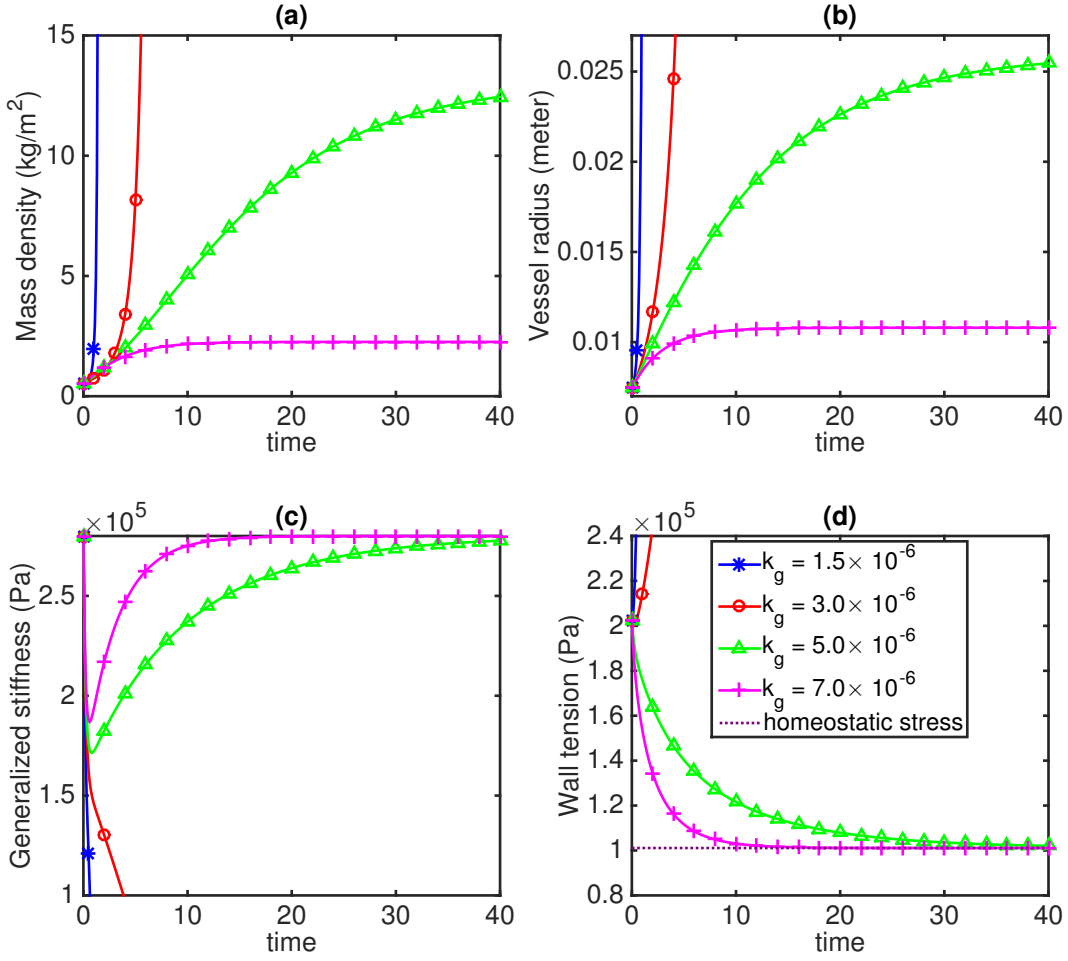

Figure 4.3: Time evolution of vessel properties ($M(t)$, $r(t)$, $y(t)$ and $\sigma(t)$) using various values of growth feedback constant k_g for increased decay constant α. The corresponding critical value for the growth feedback constant is $k_{cr} = 4.1 \times 10^{-6}$

we first linearized the nonlinear equations. The resulting linearization was shown to be degenerate, failing to determine the stability of the original nonlinear system. Indeed, the neutral stability property of vascular G&R observed in prior theoretical [30, 31] and computational [134] studies is due to this degeneracy, however stability properties for the original (nonlinear) system had not previously been clarified. To address this problem, we consider the 2-state subsystem $(\Delta M, \Delta y)$, in which Δr was eliminate due to its linear dependence on ΔM. While the resulting equation for ΔM was non-homogenous, it was homogenized by taking its time derivative. The resulting dynamics for $(\dot{\Delta M}, \Delta y)$ were made exponentially stable by requiring the eigenvalues to be negative, by which local exponential stability of the

mass density rate $\Delta\dot{M}$ and generalized stiffness Δy for the nonlinear system were established. Using the local exponential stability of $\Delta\dot{M}$ and the triangle inequality, neutral stability of the mass density $M(t)$ for the nonlinear system was established. Similar arguments imply that the vessel radius $r(t)$ is neutrally stable and wall tension $\sigma(t)$ is exponentially stable for the nonlinear system.

When converting the integral equation (4.21) for the vessel radius r to a non-delayed ODE, we derived an extended state y defined by (4.31). The meaning of y is discussed here. Consider the vascular force in the circumferential direction

$$T_\theta(t) = Pr(t) = R\int_0^t \frac{m(\tau)}{\rho} q(t-\tau) E\left[G_h \frac{r(t)}{r(\tau)} - 1\right] \frac{G_h}{r(\tau)} d\tau \ . \tag{4.102}$$

Now take the first variation of the above equation corresponding to a snapshot of the G&R process. Since $q(t)$ is a known function of t and time is fixed when taking the variation, δq and δt are both equal to zero. The only two functions that have non-zero first variation are δT_θ and δr, and therefore, the equation is reduced into the following form

$$\begin{aligned}
\delta T_\theta &= \delta\left[R\int_0^t \frac{m(\tau)}{\rho} q(t-\tau) E\left[G_h \frac{r(t)}{r(\tau)} - 1\right] \frac{G_h}{r(\tau)} d\tau\right] \\
&= R\int_0^t \frac{m(\tau)}{\rho} q(t-\tau) E\delta\left[G_h \frac{r(t)}{r(\tau)} - 1\right] \frac{G_h}{r(\tau)} d\tau \\
&= R\int_0^t \frac{m(\tau)}{\rho} q(t-\tau) E\frac{G_h^2}{r^2(\tau)} d\tau \cdot \delta r \\
&= y(t)\cdot\delta r \ .
\end{aligned} \tag{4.103}$$

Therefore, the extended state y can be defined as the ratio of variations of stress and strain in circumferential direction, multiplied by a constant $\frac{R}{h}$,

$$y = \frac{\delta T_\theta}{\delta r} = \frac{\delta T_\theta/h}{\delta r/R}\frac{R}{h} = \frac{\delta\sigma_\theta}{\delta\epsilon_\theta}\frac{R}{h} \ . \tag{4.104}$$

This implies that y physically represents a generalized stiffness resisting radial expansion for the mixture of vascular constituents. In our study we only consider one species of vascular constituents aligned in the circumferential direction for simplicity of exposition. However, we note that within one constituent family, constituents produced at different times τ form a *mixture* of constituents that possess different natural configurations. We demonstrated in Sec. 4.4.7 that it is straightforward to extend the theory to a mixture model with multiple species in the current setting, however cases of asymmetric expansion would require more involved analysis of the associated kinematics.

The derived stability criteria for the nonlinear system were verified by numerical simulations. As shown in Figure 4.1, for the three cases (Case 2-4) satisfying the derived stability criteria, only the generalized stiffness y and the wall tension σ converge to their homeostatic values, while vessel radius r and mass density M only remain bounded (they do not converge

to specific homeostatic values). These results from numerically integrating the nonlinear evolution equations are consistent with the stability conclusions obtained from the presented theoretical analysis. When the system is stable, only y and σ exhibit local exponential stability while r and M exhibit neutral stability. It is interesting to note that these convergence behaviors match with prior observations from computational studies in idealized [13, 12] and patient-specific [134] geometries, where less restrictive modeling assumptions were employed than those used to develop the theoretical model herein. Moreover, we note that while the theoretical analysis only implies *local* stability properties about the homeostatic state, the numerical experiments considered *large* deviations from the homeostatic state; nonetheless identical stability properties were observed as predicted by the theoretical model.

For the numerical experiments, pathological G&R was triggered by introducing an initial mass loss to the vessel wall. This caused an immediate weakening of vessel, as reflected in the initial drop of the generalized stiffness y (see Figure 4.1c). However, for the three stable cases (Case 2-4), after the initial drop due to mass loss, the generalized stiffness y recovered back to the homeostatic value. This is because when $k_g > k_{cr}$, thickening of vessel wall caused by stress mediated growth is fast enough to compensate the natural expansion caused by the initial mass loss and natural turnover of vascular constituent. On the other hand, for Case 1, $k_g \leq k_{cr}$, and the stress mediated growth (feedback) is not strong enough to compensate for the weakening of the vessel and natural turnover. Therefore, expansion proceeds with continuous increase of vessel radius r and wall tension σ.

Based on the stabilizing criteria (4.73), the stability of vascular expansion depends on growth parameters (k_g, α) and material properties ($\mathbf{E}$, ρ). To understand how these factors influence the stability behavior, we first increased the material stiffness E holding all other parameters at their nominal values. The simulation results (Figure 4.2) show that, when stiffness $\mathbf{E}$ is doubled, all four values of the feedback growth constant k_g are stable, including the case $k_g = 1.5 \times 10^{-6}$, which was originally not stable. This can be seen from the definition of the critical value k_{cr}

$$k_{cr} \triangleq \frac{\alpha R M_h}{\rho P r_h^2} \left[\frac{1}{1 + \frac{E M_h}{2 \rho P r_h}} \right] . \tag{4.105}$$

When material stiffness E increases, k_{cr} decreases and stabilizing criterion will be easier to satisfy. This result, that increased arterial stiffness may have a stabilizing effect, matches observations in [31, 101]. We note however that in previous clinical studies [34, 98], it has been observed that increased wall stiffness correlates with the occurrence of aortic aneurysm. However, increased vessel wall stiffness may be a consequence of the disease than a direct cause. Alternatively, other factors such as multidirectional expansion and biochemical effects may be at play in vivo that are not considered in the present modeling.

We also sought to understand the influence of growth parameters (k_g, α). The constant α defines the rate of vascular constituent turnover. When α was increased, the results in Figure 4.3 demonstrate a destabilizing behavior. Namely, Case 2 ($k_g = 3.0 \times 10^{-6}$) that was stable for the nominal parameter set led to unstable expansion. Again, this trend can be anticipate from (4.105). As α is increased, the critical value for the feedback growth constant

also increases, and the cases of $k_g = 1.5\times10^{-6}$ and $k_g = 3.0\times10^{-6}$ fail to satisfy the stabilizing condition. Prior studies [102, 1] have observed increased collagen turnover in abdominal aortic aneurysms and ruptured abdominal aortic aneurysms. Additionally, [37] found that the collagen turnover is significantly more rapid in patients with risk factors for aneurysm formation/rupture, such as smoking or hypertension. These observations are consistent with the theoretical and computational analyses here that increased decay constant α can destabilize the vascular G&R process.

While we assumed (mean) blood pressure to be constant in our analysis, we here consider the effect of increased blood pressure (hypertension) on the stability of vascular G&R. Based on the stabilizing criterion (4.105), an increase of mean blood pressure P will cause a decrease of the critical value k_{cr}, which indicates that hypertension acts as a stabilizing factor. However, this is inconsistent with evidence that hypertension is a risk factor for aneurysm growth and rupture [24]. It is important to notice that (4.40) holds true only when P denotes the pressure producing the homeostatic hoop stress σ_h when $M = M_h$ and $r = r_h$. Let us denote the homeostatic pressure as P_h. In order to study the influence of mean blood pressure on the stability of vascular expansion, we need to consider a deviation from the homeostatic pressure. Thus, for a general pressure P in (4.21), we assume

$$P = P_h + \Delta P \tag{4.106}$$

where ΔP is a small pressure deviation and $P_h = \frac{E[G_h-1]M_h}{\rho r_h}$ based on (4.40). Note that we here only consider a constant change of pressure, i.e. ΔP is independent of time. After the same procedure of linearization, the 3-state linear system equation becomes

$$\frac{d}{dt}\begin{bmatrix}\Delta r\\ \Delta M\\ \Delta y\end{bmatrix} = \begin{bmatrix} \frac{1}{k_h}\left[\alpha - \frac{k_g\rho P_h r_h^2}{RM_h}\right]\left[2\Delta r - \frac{r_h}{M_h}\Delta M + \frac{r_h}{P_h}\Delta P\right] \\ \frac{k_g\rho P_h r_h}{R}\left[2\Delta r - \frac{r_h}{M_h}\Delta M + \frac{r_h}{P_h}\Delta P\right] \\ -\frac{k_2 M_h}{r_h^3}\left[\alpha - \frac{k_g\rho P_h r_h^2}{RM_h}\right]\left[2\Delta r - \frac{r_h}{M_h}\Delta M + \frac{r_h}{P_h}\Delta P\right] - \alpha\left[\Delta y - \frac{k_2 M_h}{r_h^2 P_h}\Delta P\right] \end{bmatrix} \tag{4.107}$$

If we set the new deviation variable for generalized stiffness $y(t)$ as

$$\overline{\Delta y} \triangleq \Delta y - \frac{k_2 M_h}{r_h^2 P_h}\Delta P\,, \tag{4.108}$$

a similar 2-state homogeneous system can be obtained with respect to $(\Delta\dot{M}, \overline{\Delta y})$ by making use of the same linear relation (4.66)

$$\frac{d}{dt}\begin{bmatrix}\Delta\dot{M}\\ \overline{\Delta y}\end{bmatrix} = \begin{bmatrix}\frac{k_g\rho P_h r_h}{R}\left[2B_1 - \frac{r_h}{M_h}\right] & 0\\ B_3 & -\alpha\end{bmatrix} \times \begin{bmatrix}\Delta\dot{M}\\ \overline{\Delta y}\end{bmatrix}\,. \tag{4.109}$$

Note that the coefficient matrix of the above 2-state system is the same as that of (4.70), except the pressure P is now replaced by the homeostatic pressure P_h. Therefore, the same stabilizing condition is obtained as follow

$$k_g > \frac{\alpha R M_h}{\rho P_h r_h^2}\left[\frac{1}{1+\frac{EM_h}{2\rho P_h r_h}}\right] \triangleq k_{cr}, \quad \alpha > 0\ . \tag{4.110}$$

Substituting $P_h = \frac{E[G_h-1]M_h}{\rho r_h}$ into the above inequality yields

$$k_{cr} = \frac{\alpha}{EG_h\left[G_h-\frac{1}{2}\right]} \approx 1.732\frac{\alpha}{E} \tag{4.111}$$

which is independent of the pressure deviation ΔP. Therefore, from the linear analysis, the stability of vascular G&R is independent of mean blood pressure.

However, the above does not imply that blood pressure does not affect solution behavior. Note that $B_1 > 0$ if

$$k_g < \frac{\alpha R M_h}{\rho P r_h^2} = \frac{\alpha}{EG_h\left[G_h-1\right]} \approx 19.048\frac{\alpha}{E} \gg k_{cr}\ . \tag{4.112}$$

We here assume the normal range of the value for k_g is around k_{cr}, which is much less than $19.048\frac{\alpha}{E}$. Therefore, B_1 is always positive. Based on the linear relation between $\Delta r(t)$ and $\Delta M(t)$ in (4.66), and the second equation of (4.107) ,

$$\frac{d}{dt}\Delta M = \lambda_1 \Delta M + \frac{k_g \rho P_h r_h}{R}\left[2B_2 + \frac{r_h}{P_h}\Delta P\right]\ , \tag{4.113}$$

where

$$\lambda_1 = \frac{k_g \rho P_h r_h}{R}\left[2B_1 - \frac{r_h}{M_h}\right] = 2EG_h\left[G_h-1\right]\left[G_h-\frac{1}{2}\right]\left[k_{cr}-k_g\right]\ . \tag{4.114}$$

The solution to the above equation is

$$\Delta M(t) = B_4 e^{\lambda_1 t} + \frac{k_g \rho P_h r_h}{-\lambda_1 R}\left[2B_2 + \frac{r_h}{P_h}\Delta P\right]\ , \tag{4.115}$$

where B_4 is a constant that depends on the initial condition. Based on the linear relation (4.66), the solution for radius change $\Delta r(t)$ is

$$\Delta r(t) = B_1 B_4 e^{\lambda_1 t} + \frac{B_1 k_g \rho P_h r_h}{-\lambda_1 R}\left[2B_2 + \frac{r_h}{P_h}\Delta P\right] + B_2\ . \tag{4.116}$$

The stability of the solution is determine by the exponential term $e^{\lambda_1 t}$. Since ΔP does not influence λ_1, it does not influence the stability of the system. However, ΔP does influences

the particular solutions for $\Delta M(t)$ and $\Delta r(t)$. Therefore, ΔP will cause a shift of the steady states (if they exist), but not the stability of the system.

In the case of stable vascular G&R ($k_g > k_{cr}$, $\lambda_1 < 0$),

$$\Delta M(t \to +\infty) = \frac{k_g \rho P_h r_h}{-\lambda_1 R} \left[2B_2 + \frac{r_h}{P_h} \Delta P \right] , \tag{4.117}$$

$$\Delta r(t \to +\infty) = \frac{B_1 k_g \rho P_h r_h}{-\lambda_1 R} \left[2B_2 + \frac{r_h}{P_h} \Delta P \right] + B_2 . \tag{4.118}$$

Therefore, if ΔP increases, it will cause the final mass density to increase. Indeed, vascular mass density needs to increase in order to balance the increased pressure and maintain the homeostatic stress σ_h. Also (4.108) shows that increased ΔP causes an increased shift of Δy. This also corresponds to the fact that the overall stiffness of the vascular mixture needs to increase to compensate for the increased pressure. Similarly, due to the positiveness of B_1, increased ΔP will cause the increased shift of the final steady state radius. In comparison with prior studies, it has similarly been shown that hypertension (i.e., increased ΔP) does not change the stability of expansion, however it does increase the thickness (proportional to mass density) of vessel wall [132, 21] and the final size of the aneurysm. Also based on the first equation of (4.107), hypertension increases the vessel expansion rate $\dot{\Delta r}$, which is consistent with prior clinical findings [67], regardless of whether the expansion is stable or not. The analysis above considers only the direct influence of hypertension on stability of vascular G&R. However, hypertension may change stability through other factors not considered here. For example, [89] indicate that collagen turnover in aorta and arteries are increased under hypertension. This corresponds to increased of α in our analysis, which is a destabilizing factor for vascular G&R.

4.7 Conclusion

A theoretical study of the stability properties of vascular G&R was presented. A system of nonlinear ordinary differential equations was obtained from the integral equations of the constrained mixture theory for G&R. Degeneracy of the linearized state equations about the homeostatic state results in a "neutral stability property" for vascular growth and remodeling previously observed in prior computational studies, and renders linear stability analysis inconclusive. To resolve this problem and extend the stability conclusions to the original nonlinear system, we were able to construct a two-state sub-system to apply Lyapunov's indirect method. Based on stability analysis for the nonlinear system, we derived a stabilizing condition for radial expansion in terms of material properties (E, ρ), G&R parameters (k_g, α), geometry (R, r_h). The neutral stability shows that, in the stable expansion case, only wall tension σ and generalized stiffness y exhibit convergence to the corresponding homeostatic values while vessel radius r and mass density of vascular constituents only remain bounded without converging to any specific values. The derived theoretical stability criteria were

demonstrated to hold broadly in numerical studies were deviations from the homeostatic state were large. Additionally, we studied the effect of increased stiffness E and increased decay constant α on the stability of radial expansion. Both the theoretical analysis and numerical simulations showed that increased stiffness has a stabilizing effect of vascular expansion while an increased turnover rate of vascular constituents has a destabilizing effect. Finally, the effect of hypertension on the stabilizing criteria was studied. This analysis showed that while increased blood pressure may cause a shift of the final steady states, it does not influence the stability properties of the model.

Chapter 5

Improving the Convergence of the Iterative Ensemble Kalman Filter by Resampling

5.1 Introduction

The Kalman filter provides optimal estimation for linear dynamics with Gaussian noise [79] and has been widely used in engineering applications. There have been several variants of this classic method aimed to improve its generality and efficiency. The extended Kalman filter (EKF) [81] and unscented Kalman filter (UKF) [78] were introduced to better address state estimation for nonlinear systems, and the ensemble Kalman filter (EnKF) [38, 15, 16] was proposed to reduce computational cost by utilizing ensemble-based covariances. The iterative ensemble Kalman filter (IEnKF) [76] was developed to handle nonlinear inverse problems and leverage the computational efficiency of utlizing ensemble-based methods. The IEnKF has since been applied to highly nonlinear inverse problems in areas such as turbulence [80, 125], geophysics [108] and biomedical engineering [124]. Performance analyses of the IEnKF can be found in [104, 103, 85].

Despite its broad applicability, the IEnKF can suffer from poor convergence and stability. A major reason the IEnKF can fail to provide accurate estimation is due to a progressively diminished estimation (shrinking) of the covariance. The objective of the work herein is to provide a mathematical explanation of the covariance shrinking effect observed with the IEnKF, and based on that, propose a new method to improve its convergence without covariance inflation. To achieve these goals, we first motivate the need for iterations in application of EnKF to nonlinear inverse problems, from a constrained optimization point of view in Section 5.2. Then in Section 5.3.1 and Section 5.3.2, we explain the reason that standard IEnKF does not converge in terms of "early stopping", which is a result of the interplay between covariance shrinkage and the effect of the nonlinearity of the forward model. In Section 5.4.1 and Section 5.4.2, we show that the "early stopping" can be prevented and

convergence can be improved by adding an ensemble resampling step with first and second moments kept unchanged. In Section 5.4.3, different resampling distributions are compared and the influence of higher order moments (particularly kurtosis) on the convergence of IEnKF is discussed.

5.2 The IEnKF Method

Consider a system described by a known *forward model*

$$x = F(\theta) \tag{5.1}$$

where $x \in \mathbb{R}^n$ is the *system state* and $\theta \in \mathbb{R}^p$ are the *model parameters*. Assume we have knowledge of the system state through *observations*

$$y = Hx + \epsilon \tag{5.2}$$

where $y \in \mathbb{R}^m$ and ϵ represents measurement error. Without loss of generality, we assume the *observation operator* H is linear. If H is nonlinear, the nonlinearity can be absorbed into the nonlinearity of the forward model $F(\cdot)$ by redefining the state variable x.

The *inverse problem* seeks to estimate θ from observations y. This estimation can be performed using the IEnKF, which employs a *two-stage* iterative estimation process. The first stage entails an ensemble-based Kalman *update*, and the second stage entails a subsequent *prediction* to ensure an overall update that is consistent with the forward model. This two-stage process is iteratively repeated until convergence, as review below.

5.2.1 Update stage

Assume we have a set of *prior ensembles* for θ and x:

$$\left\{\hat{\theta}_t^{(j)}\right\}_{j=1}^{J} \quad \text{and} \quad \left\{\hat{x}_t^{(j)}\right\}_{j=1}^{J} .$$

Index (j) denotes an ensemble member, J is the number of ensembles, and index t denotes the *iteration* number in what will be an iterative update process. The *hat* notation $\hat{(\cdot)}$ denotes a *prior* estimate which has not incorporated the information from obervations yet. Based on the misfit between *observations* and *reconstructed output* (i.e, $y_t^{(j)} - H\hat{x}_t^{(j)}$) an ensemble-based Kalman *update* is used to produce *posterior ensembles* for θ and x:

$$\theta_t^{(j)} = \hat{\theta}_t^{(j)} + C_{\hat{\theta}_t\hat{x}_t} H^T \left(HC_{\hat{x}_t\hat{x}_t}H^T + \Gamma\right)^{-1} \left(y_t^{(j)} - H\hat{x}_t^{(j)}\right) , \tag{5.3a}$$

$$x_t^{(j)} = \hat{x}_t^{(j)} + C_{\hat{x}_t\hat{x}_t} H^T \left(HC_{\hat{x}_t\hat{x}_t}H^T + \Gamma\right)^{-1} \left(y_t^{(j)} - H\hat{x}_t^{(j)}\right) , \tag{5.3b}$$

where $C_{\hat{\theta}_t\hat{x}_t}$, $C_{\hat{x}_t\hat{x}_t}$ are the discrete covariance matrices derived from the prior ensembles:

$$C_{\hat{\theta}_t\hat{x}_t} = \frac{1}{J}\sum_{j=1}^{J}\left(\hat{\theta}_t^{(j)} - \bar{\hat{\theta}}_t\right)\left(\hat{x}_t^{(j)} - \bar{\hat{x}}_t\right)^T ,$$
$$C_{\hat{x}_t\hat{x}_t} = \frac{1}{J}\sum_{j=1}^{J}\left(\hat{x}_t^{(j)} - \bar{\hat{x}}_t\right)\left(\hat{x}_t^{(j)} - \bar{\hat{x}}_t\right)^T . \tag{5.4}$$

The *bar* notation $\bar{(\cdot)}$ denotes *ensemble mean*. For each ensemble member j, the observation $y_t^{(j)}$ is drawn from a normal distribution $\mathcal{N}(\bar{y}, \Gamma)$, where Γ denotes the covariance of the observation error ϵ (see [76] for details).

5.2.2 Prediction stage

The Kalman update (6.19) may generate posterior estimates $\theta_t^{(j)}$ and $x_t^{(j)}$ that no longer satisfy the forward model (5.1). Therefore, a *prediction* is used to apply the forward model to the current posterior parameter estimates to generate prior states for the next iteration step. Namely, the prior ensembles for the next step $\left\{\hat{\theta}_{t+1}^{(j)}\right\}_{j=1}^{J}$ and $\left\{\hat{x}_{t+1}^{(j)}\right\}_{j=1}^{J}$ are obtained by setting

$$\hat{\theta}_{t+1}^{(j)} = \theta_t^{(j)} , \tag{5.5a}$$
$$\hat{x}_{t+1}^{(j)} = F(\theta_t^{(j)}) . \tag{5.5b}$$

5.2.3 Iterative process

The results of (5.5) are plugged back into (6.19), with $t \leftarrow t+1$, and the process is repeated until some stopping criterion is satisfied, e.g., the *innovation* becomes less than some user-defined error tolerance (tol):

$$\|\bar{y} - Hx_t\|^2 < tol \quad \text{where} \quad x_t = F(\theta_t) \tag{5.6}$$

where $\bar{y}$ is the mean of the observation ensemble $\left\{y_t^{(j)}\right\}_{j=1}^{J}$, which is independent of t. Here, the overall estimation of the unknown parameters at step t is computed as the posterior ensemble mean

$$\bar{\theta}_t = \frac{1}{J}\sum_{j=1}^{J}\theta_t^{(j)} , \tag{5.7}$$

Note that when the forward model $F(\cdot)$ is linear with respect to θ, the prediction step (5.5) is not necessary, because

$$\begin{aligned} x_t^{(j)} &= \hat{x}_t^{(j)} + C_{\hat{x}_t\hat{x}_t} H^T \left(HC_{\hat{x}_t\hat{x}_t}H^T + \Gamma\right)^{-1} \left(y_t^{(j)} - H\hat{x}_t^{(j)}\right) \\ &= F\hat{\theta}_t^{(j)} + FC_{\hat{\theta}_t\hat{x}_t} H^T \left(HC_{\hat{x}_t\hat{x}_t}H^T + \Gamma\right)^{-1} \left(y_t^{(j)} - H\hat{x}_t^{(j)}\right) \\ &= F\theta_t^{(j)} \ . \end{aligned} \tag{5.8}$$

However, when $F(\cdot)$ is nonlinear, the posterior estimates $\theta_t^{(j)}$ and $x_t^{(j)}$ from (6.19) will not satisfy (5.1) in general, which is why an iterative estimation process is needed. It is the convergence of this iterative process for nonlinear problems that is the focus of this chapter.

5.2.4 Example

Here we introduce an example that demonstrates the potential problem with convergence of the IEnKF for nonlinear systems. Consider the following forward model:

$$\begin{bmatrix} x_1 \\ x_2 \end{bmatrix} = F(\theta) = \begin{bmatrix} \exp(-(\theta_1+1)^2 - (\theta_2+1)^2) \\ \exp(-(\theta_1-1)^2 - (\theta_2-1)^2) \end{bmatrix} \ , \tag{5.9}$$

with observation operator

$$H = [-1.5, -1.0] \ . \tag{5.10}$$

Assume observation data is available with mean $\bar{y} = -1$ and uncertainty $\Gamma = 0.01$.

Figure 5.1a and 5.1b show, respectively, the solution path for θ in parameter space, and the solution path for x in state space, during progressive iterations of the IEnKF. It can be observed in Fig. 5.1a that the parameter estimate does not converge to a solution where $\|\bar{y} - HF(\theta_t)\|^2 = 0$. In Figure 5.1b the prior mean and posterior mean are sequentially plotted at each iteration. It can be observed that the solution oscillates between these two means. In particular, the update stage makes the solution approach $\|\bar{y} - Hx_t\|^2 = 0$ shown in red, and the prediction stage makes the solution approach the dotted region where the forward model (5.1) is satisfied. This example demonstrates that although innovation is not minimized, further iterations of the IEnKF will not a) improve the estimation of θ, or b) enable the state estimate to converge to a value that simultaneously satisfies the forward model and minimizes misfit with the observations. These two phenomena will be considered more rigorously in the next section.

5.3 Early Stopping of the IEnKF

In this section, we describe why the standard IEnKF leads to poor convergence when applied to nonlinear inverse problems. We first demonstrate how sequential Kalman updating alone affect the covariance matrices and resulting Kalman operator. We then demonstrate how the full IEnKF procedure, involving both Kalman update and prediction, affects the covariance matrices and Kalman operator.

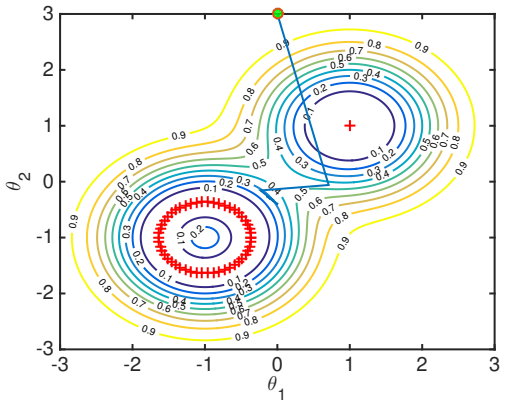

(a) The solution path of the ensemble mean θ_t at each iteration t plotted along with the level sets of $\|\bar{y} - HF(\theta)\|^2$. The green circle denotes the starting value. The red "+" highlight optimal locations where $\|\bar{y} - HF(\theta)\|^2 = 0$.

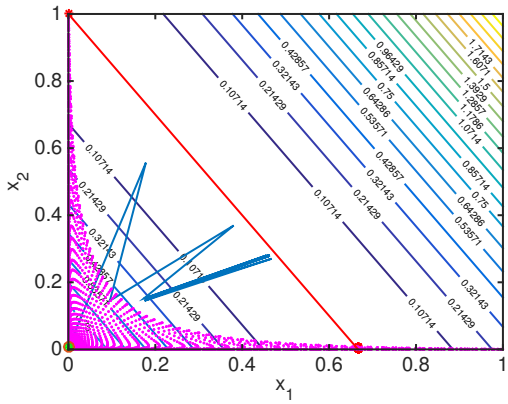

(b) The solution path, including both prior mean $\bar{\hat{x}}_t$ and posterior mean $\bar{x}_t$, at each iteration t plotted along with the level sets of $\|\bar{y} - Hx\|^2$. The green circle denotes the starting value. The red line highlights the optimal locations where $\bar{y} - Hx = 0$. The dotted region represents the image of the forward mapping $F(\cdot)$.

Figure 5.1: Convergence of the IEnKF applied to the model problem demonstrating (a) parameter and (b) state values do not converge to the desired solution (the red locations).

5.3.1 Shrinking covariance

If we ignore the prediction stage (5.5) and only consider the Kalman update (6.19), it can be shown that the covariance matrix $C_{H\hat{x},\hat{\theta}}$ resulting from two sequential Kalman updates is

$$C_{H\hat{x}_{t+1},\hat{\theta}_{t+1}} = \left(I - HC_{\hat{x}_t,\hat{x}_t}H^T\left(HC_{\hat{x}_t,\hat{x}_t}H^T + \Gamma\right)^{-1}\right)C_{H\hat{x}_t,\hat{\theta}_t}\ , \tag{5.11}$$

where I denotes the identity matrix. The above equation can be further simplified as

$$C_{H\hat{x}_{t+1},\hat{\theta}_{t+1}} = P_t C_{H\hat{x}_t,\hat{\theta}_t}\ , \tag{5.12}$$

where P_t is the *shrinking matrix* defined as

$$\begin{aligned} P_t &\doteq I - HC_{\hat{x}_t,\hat{x}_t}H^T\left(HC_{\hat{x}_t,\hat{x}_t}H^T + \Gamma\right)^{-1} \\ &= \Gamma\left(HC_{\hat{x}_t,\hat{x}_t}H^T + \Gamma\right)^{-1}. \end{aligned} \tag{5.13}$$

Note that the observation uncertainty usually takes the form $\Gamma = \alpha I$ with $\alpha > 0$. Thus, the Frobenius norm of $C_{H\hat{x}_{t+1},\hat{\theta}_{t+1}}$ can be upper-bounded in the following manner

$$\begin{aligned}\left\|C_{H\hat{x}_{t+1},\hat{\theta}_{t+1}}\right\|_F &= \left\|P_t C_{H\hat{x}_t,\hat{\theta}_t}\right\|_F \\ &\leq \frac{\alpha}{\lambda_{min}\left(HC_{\hat{x}_t,\hat{x}_t}H^T\right)+\alpha}\left\|C_{H\hat{x}_t,\hat{\theta}_t}\right\|_F \\ &\leq \prod_{\tau=1}^{t}\frac{\alpha}{\lambda_{min}\left(HC_{\hat{x}_\tau,\hat{x}_\tau}H^T\right)+\alpha}\left\|C_{H\hat{x}_1,\hat{\theta}_1}\right\|_F \ . \end{aligned} \tag{5.14}$$

If there exists an uniform lower bound $\delta > 0$ such that

$$\lambda_{min}\left(HC_{\hat{x}_\tau,\hat{x}_\tau}H^T\right) > \delta, \quad \forall\tau = 1, 2, \dots \ , \tag{5.15}$$

then

$$\left\|C_{H\hat{x}_{t+1},\hat{\theta}_{t+1}}\right\|_F \leq \left(\frac{\alpha}{\delta+\alpha}\right)^t \left\|C_{H\hat{x}_1,\hat{\theta}_1}\right\|_F \ . \tag{5.16}$$

Therefore, $C_{H\hat{x}_t,\hat{\theta}_t}$ or $C_{\hat{\theta}_t,H\hat{x}_t}$ will approach to zero as the iteration number increases, i.e.,

$$\lim_{t\to+\infty}\left\|C_{H\hat{x}_t,\hat{\theta}_t}\right\|_F = 0 \ . \tag{5.17}$$

Similarly, it can be shown that $C_{\hat{x}_t,H\hat{x}_t}$ will also converge to a zero matrix as t increases, unless (5.15) is violated. By checking the Kalman update (6.19), it can be noted that the convergence of $C_{\hat{\theta}_t,H\hat{x}_t}$ and $C_{\hat{x}_t,H\hat{x}_t}$ to zero matrices will cause the Kalman gains

$$K_t = C_{\hat{\theta}_t\hat{x}_t}H^T\left(HC_{\hat{x}_t\hat{x}_t}H^T+\Gamma\right)^{-1} \ , \tag{5.18}$$

$$K'_t = C_{\hat{x}_t\hat{x}_t}H^T\left(HC_{\hat{x}_t\hat{x}_t}H^T+\Gamma\right)^{-1} \ , \tag{5.19}$$

to approach to zero as t increases. This implies that further iterations will not update the parameter estimation θ_t, regardless of the innovation $\|\bar{y} - Hx_t\|$. This *early stopping* is one of the main reasons for which the IEnKF fails to converge. It was observed in our example problem in §5.2.4 (Figure 5.1a).

5.3.2 Effect of forward model nonlinearity

We now consider the prediction step (5.5) and show how the nonlinearity of the forward model affects the convergence of the IEnKF. First, consider the prior ensembles for the current step

$$\left\{\hat{\theta}_t^{(j)}\right\}_{j=1}^J \quad \text{and} \quad \left\{\hat{x}_t^{(j)}\right\}_{j=1}^J .$$

The mean of the prior ensembles can be computed as

$$\bar{\hat{\theta}}_t = \frac{1}{J}\sum_{j=1}^{J}\hat{\theta}_t^{(j)} \ , \tag{5.20}$$

$$\begin{aligned}\bar{\hat{x}}_t &= \frac{1}{J}\sum_{j=1}^{J} F\left(\hat{\theta}_t^{(j)}\right) \\ &= \frac{1}{J}\sum_{j=1}^{J} F\left(\bar{\hat{\theta}}_t\right) + \nabla F\left(\bar{\hat{\theta}}_t\right)\left(\hat{\theta}_t^{(j)} - \bar{\hat{\theta}}_t\right) + \mathcal{O}\left(\left\|\hat{\theta}_t^{(j)} - \bar{\hat{\theta}}_t\right\|^2\right) \\ &= F\left(\bar{\hat{\theta}}_t\right) + \nabla F\left(\bar{\hat{\theta}}_t\right)\frac{1}{J}\sum_{j=1}^{J}\left(\hat{\theta}_t^{(j)} - \bar{\hat{\theta}}_t\right) + \mathcal{O}\left(\left\|\hat{\theta}_t^{(j)} - \bar{\hat{\theta}}_t\right\|^2\right) \\ &= F\left(\bar{\hat{\theta}}_t\right) + \mathcal{O}\left(\left\|\hat{\theta}_t^{(j)} - \bar{\hat{\theta}}_t\right\|^2\right) \ , \end{aligned} \tag{5.21}$$

where $\bar{\hat{x}}_t$ is computed using Taylor expansion. Define the Kalman gain for the θ update at step t as

$$K_t \doteq C_{\hat{\theta}_t\hat{x}_t} H^T \left(HC_{\hat{x}_t\hat{x}_t}H^T + \Gamma\right)^{-1} \ , \tag{5.22}$$

so that the Kalman update equation becomes

$$\hat{\theta}_{t+1}^{(j)} = \theta_t^{(j)} = \hat{\theta}_t^{(j)} + K_t\left(y_t^{(j)} - H\hat{x}_t^{(j)}\right) \ . \tag{5.23}$$

The mean of the prior ensemble for θ at step $t+1$ can be computed as

$$\bar{\hat{\theta}}_{t+1} = \frac{1}{J}\sum_{j=1}^{J}\hat{\theta}_{t+1}^{(j)} = \frac{1}{J}\sum_{j=1}^{J}\theta_t^{(j)} = \bar{\hat{\theta}}_t + K_t\left(\bar{y} - H\bar{\hat{x}}_t\right) \ , \tag{5.24}$$

Combining (5.20), (5.21), (5.23), (5.24), we can obtain the deviation of each ensemble member to its ensemble mean at the next step $t+1$ as

$$\hat{\theta}_{t+1}^{(j)} - \bar{\hat{\theta}}_{t+1} = \hat{\theta}_t^{(j)} - \bar{\hat{\theta}}_t - K_t\left(H\hat{x}_t^{(j)} - H\bar{\hat{x}}_t\right) + K_t\left(y_t^{(j)} - \bar{y}\right) \ , \tag{5.25}$$

$$\begin{aligned}\hat{x}_{t+1}^{(j)} - \bar{\hat{x}}_{t+1} &= F\left(\hat{\theta}_{t+1}^{(j)}\right) - F\left(\bar{\hat{\theta}}_{t+1}\right) + \mathcal{O}\left(\left\|\hat{\theta}_{t+1}^{(j)} - \bar{\hat{\theta}}_{t+1}\right\|^2\right) \\ &= \nabla F\left(\bar{\hat{\theta}}_{t+1}\right)\left(\hat{\theta}_{t+1}^{(j)} - \bar{\hat{\theta}}_{t+1}\right) + \mathcal{O}\left(\left\|\hat{\theta}_{t+1}^{(j)} - \bar{\hat{\theta}}_{t+1}\right\|^2\right) \\ &= \nabla F\left(\bar{\hat{\theta}}_{t+1}\right)\left(\hat{\theta}_t^{(j)} - \bar{\hat{\theta}}_t - K_t\left(H\hat{x}_t^{(j)} - H\bar{\hat{x}}_t\right) + K_t\left(y_t^{(j)} - \bar{y}\right)\right) \\ &\quad + \mathcal{O}\left(\left\|\hat{\theta}_{t+1}^{(j)} - \bar{\hat{\theta}}_{t+1}\right\|^2\right) \ . \end{aligned} \tag{5.26}$$

Multiplying (5.26) with H yields the deviation of the reconstructed output Hx with its ensemble mean:

$$H\hat{x}_{t+1}^{(j)} - H\bar{\hat{x}}_{t+1} = H\nabla F\left(\bar{\hat{\theta}}_{t+1}\right)\left(\hat{\theta}_t^{(j)} - \bar{\hat{\theta}}_t - K_t\left(H\hat{x}_t^{(j)} - H\bar{\hat{x}}_t\right) + K_t\left(y_t^{(j)} - \bar{y}\right)\right) + \mathcal{O}\left(\left\|\hat{\theta}_{t+1}^{(j)} - \bar{\hat{\theta}}_{t+1}\right\|^2\right) \ . \tag{5.27}$$

Define a new state vector that includes the model parameter and the reconstructed output that centered with respect the corresponding means

$$z \doteq \left[\theta - \bar{\theta}, Hx - H\bar{x}\right]^T \ , \tag{5.28}$$

and combine (5.25) and (5.27) to yield the following update equation for z

$$\hat{z}_{t+1}^{(j)} = A_t\hat{z}_t^{(j)} + A_t\Delta_{y,t}^{(j)} + \Lambda_t^{(j)} \ , \tag{5.29}$$

where the evolution matrix

$$A_t \doteq \begin{bmatrix} I & -K_t \\ H\nabla F\left(\bar{\hat{\theta}}_{t+1}\right) & -H\nabla F\left(\bar{\hat{\theta}}_{t+1}\right)K_t \end{bmatrix} \ , \tag{5.30}$$

$$\Delta_{y,t}^{(j)} \doteq \begin{bmatrix} 0 \\ y_t^{(j)} - \bar{y} \end{bmatrix}, \quad \Delta_t^{(j)} \doteq \mathcal{O}\left(\left\|\hat{\theta}_{t+1}^{(j)} - \bar{\hat{\theta}}_{t+1}\right\|^2\right), \quad \Lambda_t^{(j)} \doteq \begin{bmatrix} 0 \\ \Delta_t^{(j)} \end{bmatrix} \ . \tag{5.31}$$

Therefore the evolution equation of the covariance matrix of $\hat{z}$ can be obtained from (5.29)

$$C_{\hat{z}_{t+1},\hat{z}_{t+1}} = A_tC_{\hat{z}_t,\hat{z}_t}A_t^T + A_tC_{\Delta_{y,t},\Delta_{y,t}}A_t^T + A_tC_{\hat{z}_t,\Lambda_t} + C_{\Lambda_t,\hat{z}_t}A_t^T + C_{\Lambda_t,\Lambda_t} \ , \tag{5.32}$$

where

$$C_{\hat{z}_{t+1},\hat{z}_{t+1}} = \begin{bmatrix} C_{\hat{\theta}_{t+1},\hat{\theta}_{t+1}} & C_{\hat{\theta}_{t+1},H\hat{x}_{t+1}} \\ C_{H\hat{x}_{t+1},\hat{\theta}_{t+1}} & C_{H\hat{x}_{t+1},H\hat{x}_{t+1}} \end{bmatrix} \ , \tag{5.33}$$

$$C_{\Delta_{y,t},\Delta_{y,t}} = \begin{bmatrix} 0 & 0 \\ 0 & C_{y_t,y_t} \end{bmatrix} = \begin{bmatrix} 0 & 0 \\ 0 & \Gamma \end{bmatrix} \ . \tag{5.34}$$

Note that in obtaining (5.32) we have used that the observations y are independent of the new state z, i.e. $\Delta_{y,t}$ is independent of $\hat{z}_t$ and Λ_t. To understand how different terms in (5.33) evolve, (5.32) is re-written in the matrix form below:

$$\begin{aligned} \begin{bmatrix} C_{\hat{\theta}_{t+1},\hat{\theta}_{t+1}} & C_{\hat{\theta}_{t+1},H\hat{x}_{t+1}} \\ C_{H\hat{x}_{t+1},\hat{\theta}_{t+1}} & C_{H\hat{x}_{t+1},H\hat{x}_{t+1}} \end{bmatrix} &= A_t \begin{bmatrix} C_{\hat{\theta}_t,\hat{\theta}_t} & C_{\hat{\theta}_t,H\hat{x}_t} \\ C_{H\hat{x}_t,\hat{\theta}_t} & C_{H\hat{x}_t,H\hat{x}_t} + \Gamma \end{bmatrix} A_t^T \\ &+ A_t \begin{bmatrix} 0 & C_{\hat{\theta}_t,\Delta_t} \\ 0 & C_{H\hat{x}_t,\Delta_t} \end{bmatrix} + \begin{bmatrix} 0 & 0 \\ C_{\Delta_t,\hat{\theta}_t} & C_{\Delta_t,H\hat{x}_t} \end{bmatrix} A_t^T \\ &+ \begin{bmatrix} 0 & 0 \\ 0 & C_{\Delta_t,\Delta_t} \end{bmatrix} \ . \end{aligned} \tag{5.35}$$

The properties of the matrix A_t are critical to the evolution of the covariances. Thus the eigen-problem for A_t is solved here first. To simplify the notation, A_t is re-defined as

$$A_t \doteq \begin{bmatrix} I & -K_t \\ H\nabla F\left(\bar{\hat{\theta}}_{t+1}\right) & -H\nabla F\left(\bar{\hat{\theta}}_{t+1}\right) K_t \end{bmatrix} = \begin{bmatrix} I_{d_\theta \times d_\theta} & a \\ b & ba \end{bmatrix} , \tag{5.36}$$

and the characteristic equation for A_t is given by

$$\begin{aligned} \det(A_t - \lambda I) &= \det\left((1-\lambda) I_{d_\theta \times d_\theta}\right) \det\left(ba - \lambda I_{d_y \times d_y} - b\left((1-\lambda) I_{d_\theta \times d_\theta}\right)^{-1} a\right) \\ &= (1-\lambda)^{d_\theta - d_y} \lambda^{d_y} \det\left(\lambda I_{d_y \times d_y} - \left(I_{d_y \times d_y} + ba\right)\right) = 0 , \end{aligned} \tag{5.37}$$

where d_θ and d_y are the dimensions for the hidden model parameter θ and the observed output y respectively. Solving the equation above yields the three different kinds of eigenvalues (the multiplicities are not necessarily equal to one):

$$\lambda_1 = 0 , \tag{5.38}$$

$$\lambda_2 = \lambda(I + ba) = \lambda\left(I - H\nabla F\left(\bar{\hat{\theta}}_{t+1}\right) K_t\right) \approx \lambda\left(\Gamma\left(HC_{\hat{x}_t \hat{x}_t} H^T + \Gamma\right)^{-1}\right) , \tag{5.39}$$

$$\lambda_3 = 1 . \tag{5.40}$$

There are two key points worth clarifying here: (1) λ_2 are the eigenvalues of the matrix $\Gamma\left(HC_{\hat{x}_t \hat{x}_t} H^T + \Gamma\right)^{-1}$ which satisfy $0 < \lambda_2 < 1$; (2) λ_3 represent the insufficiency of the observation and only show up when $d_y < d_\theta$ which is usually the case in real applications as the observation is usually limited, and this scenario will be the focus for the rest of this chapter.

5.3.2.1 Convergence of $C_{\hat{\theta},\hat{\theta}}$ and $C_{\hat{\theta},H\hat{x}}$

Based on Eq. (5.35), the update equation for $C_{\theta,\theta}$ can be obtained

$$C_{\hat{\theta}_{t+1},\hat{\theta}_{t+1}} = C_{\hat{\theta}_t,\hat{\theta}_t} - C_{\hat{\theta}_t,H\hat{x}_t}\left(C_{H\hat{x}_t,H\hat{x}_t} + \Gamma\right)^{-1} C_{H\hat{x}_t,\hat{\theta}_t} . \tag{5.41}$$

Note that $\hat{\theta}_t$ is a vector of dimension d_θ. For each scalar entry of $\hat{\theta}_t$, the evolution equation is

$$C_{\hat{\theta}^s_{t+1},\hat{\theta}^s_{t+1}} = C_{\hat{\theta}^s_t,\hat{\theta}^s_t} - C_{\hat{\theta}^s_t,H\hat{x}_t}\left(C_{H\hat{x}_t,H\hat{x}_t} + \Gamma\right)^{-1} C_{H\hat{x}_t,\hat{\theta}^s_t} , \tag{5.42}$$

where the superscript s denotes that $\hat{\theta}^s_t$ is scalar. Since the second term on the right hand side of the above equation is non-negative, the sequence $\left\{C_{\hat{\theta}^s_t,\hat{\theta}^s_t}\right\}_{t=1}^{\infty}$ is a monotone decreasing sequence that all elements are bounded below ($\hat{\theta}^s_t \geq 0$). Thus the sequence is convergent based on monotone convergence theorem. This indicates that the incremental term must converge to zero, i.e.

$$\lim_{t\to\infty} C_{\hat{\theta}^s_t,H\hat{x}_t}\left(C_{H\hat{x}_t,H\hat{x}_t} + \Gamma\right)^{-1} C_{H\hat{x}_t,\hat{\theta}^s_t} = 0 \quad \Rightarrow \quad \lim_{t\to\infty} C_{\hat{\theta}^s_t,H\hat{x}_t} = 0, \forall s = 1, ..., d_\theta , \tag{5.43}$$

which is equivalent to

$$\lim_{t\to\infty} C_{\hat{\theta}_t,H\hat{x}_t} = 0 \; . \tag{5.44}$$

This further indicates the convergence of $C_{\hat{\theta}_t,\hat{\theta}_t}$ as

$$\lim_{t\to\infty} \left\| C_{\hat{\theta}_{t+1},\hat{\theta}_{t+1}} - C_{\hat{\theta}_t,\hat{\theta}_t} \right\|_F = 0 \; , \tag{5.45}$$

and the sequence of $C_{\hat{\theta}_t,\hat{\theta}_t}$ lies in a complete space (based on the Cauchy Convergence Criterion). However, this does not mean that the $C_{\hat{\theta}_t,\hat{\theta}_t}$ will converge to zero (In real applications, we only require the covariance of $C_{\hat{\theta},\hat{\theta}}$ to decrease below a preset tolerance for true convergence [76]). And in the case of $d_y < d_\theta$, $C_{\hat{\theta}_t,\hat{\theta}_t}$ will not converge to zero. This is related to the eigenvalue $\lambda_3 = 1$ for the evolution matrix A_t. To see this, the eigenvector of the matrix A_t for $\lambda_3 = 1$ is solved,

$$\left(A_t - \lambda_3 I\right) z = \begin{bmatrix} \mathbf{0} & a \\ b & ba - I \end{bmatrix} \begin{bmatrix} z_\theta \\ z_{Hx} \end{bmatrix} = 0 \Rightarrow z_{Hx} = 0 \; . \tag{5.46}$$

Therefore, the eigenvector v_3 corresponding to $\lambda_3 = 1$ lies in the subspace of θ and has zero component in the Hx direction. The evolution matrix A_t plays a key role in shrinking the covariances $C_{\hat{\theta}_t,\hat{\theta}_t}$, $C_{\hat{\theta}_t,H\hat{x}_t}$ and $C_{H\hat{x}_t,H\hat{x}_t}$ because $0 < \lambda_1, \lambda_2 < 1$. However it does not have the variance shrinking effect in the direction of the eigenvector v_3 corresponding to $\lambda_3 = 1$ (violating the contraction requirement). Therefore, due to the non-shrinking direction v_3 lies in the subspace of θ, the sequence of $C_{\hat{\theta}_t,\hat{\theta}_t}$ will converge, but will not converge to $\mathbf{0}$.

$$\begin{aligned} C_{\hat{\theta}_{t+1},H\hat{x}_{t+1}} = {} & C_{\hat{\theta}_t,H\hat{x}_t} - C_{\hat{\theta}_t,H\hat{x}_t} \left(C_{H\hat{x}_t,H\hat{x}_t} + \Gamma\right)^{-1} C_{H\hat{x}_t,H\hat{x}_t} \\ & + C_{\hat{\theta}_t,\Delta_t} - C_{\hat{\theta}_t,H\hat{x}_t} \left(C_{H\hat{x}_t,H\hat{x}_t} + \Gamma\right)^{-1} C_{H\hat{x}_t,\Delta_t} \end{aligned} \tag{5.47}$$

5.3.2.2 Convergence of $C_{H\hat{x},H\hat{x}}$

Based on Eq. (5.35), the evolution equation for $C_{H\hat{x},H\hat{x}}$ can be derived as

$$\begin{aligned} & C_{H\hat{x}_{t+1},H\hat{x}_{t+1}} \\ = {} & H\nabla F\left(\bar{\hat{\theta}}_{t+1}\right) \left(C_{\hat{\theta}_t,\hat{\theta}_t} - C_{\hat{\theta}_t,H\hat{x}_t} \left(C_{H\hat{x}_t,H\hat{x}_t} + \Gamma\right)^{-1} C_{H\hat{x}_t,\hat{\theta}_t}\right) \left(H\nabla F\left(\bar{\hat{\theta}}_{t+1}\right)\right)^T \\ & + H\nabla F\left(\bar{\hat{\theta}}_{t+1}\right) \left(C_{\hat{\theta}_t,\Delta_t} - C_{\hat{\theta}_t,H\hat{x}_t} \left(C_{H\hat{x}_t,H\hat{x}_t} + \Gamma\right)^{-1} C_{H\hat{x}_t,\Delta_t}\right) \\ & + \left(C_{\Delta_t,\hat{\theta}_t} - C_{\Delta_t,H\hat{x}_t} \left(C_{H\hat{x}_t,H\hat{x}_t} + \Gamma\right)^{-1} C_{H\hat{x}_t,\hat{\theta}_t}\right) \left(H\nabla F\left(\bar{\hat{\theta}}_{t+1}\right)\right)^T \\ & + C_{\Delta_t,\Delta_t} \; , \end{aligned} \tag{5.48}$$

and by applying Eq. (5.25), the above equation can be simplified to

$$\begin{aligned} C_{H\hat{x}_{t+1},H\hat{x}_{t+1}} = {} & H\nabla F\left(\bar{\hat{\theta}}_{t+1}\right) C_{\hat{\theta}_{t+1},\hat{\theta}_{t+1}} \left(H\nabla F\left(\bar{\hat{\theta}}_{t+1}\right)\right)^T \\ & + H\nabla F\left(\bar{\hat{\theta}}_{t+1}\right) C_{\hat{\theta}_{t+1},\Delta_t} + C_{\Delta_t,\hat{\theta}_{t+1}} \left(H\nabla F\left(\bar{\hat{\theta}}_{t+1}\right)\right)^T \\ & + C_{\Delta_t,\Delta_t} \; . \end{aligned} \tag{5.49}$$

Because $C_{\hat{\theta}_t, H\hat{x}_t}$ is equal to zero in the steady state based on Eq. (5.44), a steady state condition of the nonlinear term Δ_t can be derived

$$\begin{aligned} C_{\hat{\theta}_t, H\hat{x}_t} &= E\left(\hat{\theta}_t - \bar{\hat{\theta}}_t, H\nabla F\left(\bar{\hat{\theta}}_t\right)\left(\hat{\theta}_t - \bar{\hat{\theta}}_t\right) + \Delta_{t-1}\right) \\ &= C_{\hat{\theta}_t, \hat{\theta}_t}\left(H\nabla F\left(\bar{\hat{\theta}}_t\right)\right)^T + C_{\hat{\theta}_t, \Delta_{t-1}} = 0 \,, \end{aligned} \tag{5.50}$$

which is equivalent to

$$C_{\hat{\theta}_t, \Delta_{t-1}} = -C_{\hat{\theta}_t, \hat{\theta}_t}\left(H\nabla F\left(\bar{\hat{\theta}}_t\right)\right)^T \,. \tag{5.51}$$

This is the stationary condition for the nonlinear term. Substituting the stationary condition (5.51) into Eq. (5.49) yields

$$\begin{aligned} C_{H\hat{x}_{t+1}, H\hat{x}_{t+1}} = & H\nabla F\left(\bar{\hat{\theta}}_{t+1}\right) C_{\hat{\theta}_{t+1}, \hat{\theta}_{t+1}}\left(H\nabla F\left(\bar{\hat{\theta}}_{t+1}\right)\right)^T \\ & - H\nabla F\left(\bar{\hat{\theta}}_{t+1}\right) C_{\hat{\theta}_{t+1}, \hat{\theta}_{t+1}}\left(H\nabla F\left(\bar{\hat{\theta}}_{t+1}\right)\right)^T \\ & - H\nabla F\left(\bar{\hat{\theta}}_{t+1}\right) C_{\hat{\theta}_{t+1}, \hat{\theta}_{t+1}}\left(H\nabla F\left(\bar{\hat{\theta}}_{t+1}\right)\right)^T \\ & + C_{\Delta_t, \Delta_t} \\ = & - H\nabla F\left(\bar{\hat{\theta}}_{t+1}\right) C_{\hat{\theta}_{t+1}, \hat{\theta}_{t+1}}\left(H\nabla F\left(\bar{\hat{\theta}}_{t+1}\right)\right)^T + C_{\Delta_t, \Delta_t} \,. \end{aligned} \tag{5.52}$$

The nonlinear term $\Delta_t = \mathcal{O}\left(\left\|\hat{\theta}_{t+1} - \bar{\hat{\theta}}_{t+1}\right\|^2\right)$ as a random variable can be decomposed into two parts: (a) a term that is correlated with $\hat{\theta}_{t+1}$ and (b) a term that is uncorrelated

$$\Delta_t = \beta^T \hat{\theta}_{t+1} + \gamma_{t+1} \tag{5.53}$$

where β can be obtained by using standard linear regression and applying Eq. (5.51):

$$\begin{aligned} \beta = & C^{-1}_{\hat{\theta}_{t+1}, \hat{\theta}_{t+1}} C_{\hat{\theta}_{t+1}, \Delta_t} \\ = & C^{-1}_{\hat{\theta}_{t+1}, \hat{\theta}_{t+1}} C_{\hat{\theta}_{t+1}, \hat{\theta}_{t+1}}\left(H\nabla F\left(\bar{\hat{\theta}}_{t+1}\right)\right)^T \\ = & -\left(H\nabla F\left(\bar{\hat{\theta}}_{t+1}\right)\right)^T \,, \end{aligned} \tag{5.54}$$

and the covariance of Δ_t can be computed as

$$\begin{aligned} C_{\Delta_t, \Delta_t} &= \beta^T C_{\hat{\theta}_{t+1}, \hat{\theta}_{t+1}} \beta + C_{\gamma_{t+1}, \gamma_{t+1}} \\ &= H\nabla F\left(\bar{\hat{\theta}}_{t+1}\right) C_{\hat{\theta}_{t+1}, \hat{\theta}_{t+1}}\left(H\nabla F\left(\bar{\hat{\theta}}_{t+1}\right)\right)^T + C_{\gamma_{t+1}, \gamma_{t+1}} \end{aligned} \tag{5.55}$$

Therefore, Eq. (5.52) can be reduced to the following simple form in the steady state.

$$C_{H\hat{x}_{t+1},H\hat{x}_{t+1}} = C_{\gamma_{t+1},\gamma_{t+1}} \tag{5.56}$$

where γ_t represents the uncorrelated component of the nonlinear effect and it cannot be reduced by usual Kalman iterations. Intuitively, this can also be directly observed from Eq. (5.35) as the nonlinear term C_{Δ_t,Δ_t} on the right hand side that is not shrunk by A_t acts directly to the entry corresponding to $C_{H\hat{x},H\hat{x}}$.

In conclusion, the take home message here is that: for the iterative ensemble Kalman filter described by the update step (6.19) and the prediction step (5.5),

- $C_{\hat{\theta}_t,H\hat{x}_t}$ will converge to zero matrix as t increases.
- $C_{H\hat{x}_t,H\hat{x}_t}$ will not converge to zero because of the nonlinearity effect of $F(\theta)$.
- $C_{\hat{\theta}_t,\hat{\theta}_t}$ will not converge to zero matrix because the insufficiency of observations.

5.3.2.3 Example

We return to the example in §5.2.4 to demonstrate the above conclusions. Figure 5.2 plot the evolution of the norms of the various covariance matrices, Kalman gain and innovation. The covariance matrix $C_{\hat{\theta}_t,H\hat{x}_t}$ converges to zero in relatively few iterations. Consequently, $C_{\hat{\theta}_t,\hat{\theta}_t}$ stops updating. $C_{H\hat{x}_t,H\hat{x}_t}$ oscillates and fails to converge due to the nonlinearity. The Kalman gain converges to zero, and the innovation fails to improve with subsequent iterations. This example demonstrated a typical situation that standard ensemble Kalman filter fails due to early stopping of the Kalman updates. The numerical simulation results are consistent with the theoretical analysis above.

5.3.3 Steady-state

In §5.3.2, we focused on the transient behavior of the various covariance matrices and their relation to the "early stopping" of the IEnKF in nonlinear problems. In this section, the steady-state behavior of the IEnKF is studied as well as the effect of observation uncertainty Γ.

Let $t = f$ denote the iteration number where θ_t is effectively unchanged with further iterations. Denote the (fixed) ensemble for θ at this step (and beyond) as

$$\left\{\theta_f^{(j)}\right\}_{j=1}^{J} . \tag{5.57}$$

There is no need to distinguish between the prior and posterior ensemble of θ as they are assumed the same for $t \geq f$. Therefore, the prior ensemble of the state x will be

$$\left\{\hat{x}_f^{(j)}\right\}_{j=1}^{J} = \left\{F\left(\theta_f^{(j)}\right)\right\}_{j=1}^{J} , \tag{5.58}$$

and will not change with respect to t since $\left\{\theta_f^{(j)}\right\}_{j=1}^{J}$ is fixed. The mean of the prior ensemble for x is

$$\bar{\hat{x}}_f = \frac{1}{J}\sum_{j=1}^{J} F\left(\theta_f^{(j)}\right) \ . \tag{5.59}$$

The mean of the posterior ensemble of x is

$$\begin{aligned}
\bar{x}_f &= \frac{1}{J}\sum_{j=1}^{J} x_f^{(j)} \\
&= \frac{1}{J}\sum_{j=1}^{J}\left(\hat{x}_f^{(j)} + C_{\hat{x}_f\hat{x}_f}H^T\left(HC_{\hat{x}_f\hat{x}_f}H^T+\Gamma\right)^{-1}\left(y_t^{(j)} - H\hat{x}_f^{(j)}\right)\right) \\
&= \bar{\hat{x}}_f + C_{\hat{x}_f\hat{x}_f}H^T\left(HC_{\hat{x}_f\hat{x}_f}H^T+\Gamma\right)^{-1}\left(\bar{y} - H\bar{\hat{x}}_f\right) \ .
\end{aligned} \tag{5.60}$$

based on the relation between prior and posterior state estimation Eq. (6.19b). Therefore the final difference (i.e., oscillation magnitude) of the prior and posterior mean of the state x is

$$\bar{x}_f - \bar{\hat{x}}_f = C_{\hat{x}_f\hat{x}_f}H^T\left(HC_{\hat{x}_f\hat{x}_f}H^T+\Gamma\right)^{-1}\left(\bar{y} - H\bar{\hat{x}}_f\right) \ . \tag{5.61}$$

Left multiplying the above by H,

$$H\bar{x}_f - H\bar{\hat{x}}_f = HC_{\hat{x}_f\hat{x}_f}H^T\left(HC_{\hat{x}_f\hat{x}_f}H^T+\Gamma\right)^{-1}\left(\bar{y} - H\bar{\hat{x}}_f\right) \ , \tag{5.62}$$

gives the oscillation magnitude of the reconstructed output. We can also obtain the relation between the output reconstruction error of the prior mean and posterior mean:

$$H\bar{x}_f - \bar{y} = \Gamma\left(HC_{\hat{x}_f\hat{x}_f}H^T+\Gamma\right)^{-1}\left(H\bar{\hat{x}}_f - \bar{y}\right) \ . \tag{5.63}$$

It can be seen from Eq. (5.62) and (5.63) that the relative magnitudes of Γ and $C_{H\hat{x}_f,H\hat{x}_f}$ determine the steady-state oscillation magnitude and mean output reconstruction error. Based on the derivations above, the following summarizes the steady-state behavior of the standard IEnKF:

- The prior and posterior ensembles of the parameter θ will approach to a fixed ensemble $\left\{\theta_f^{(j)}\right\}_{j=1}^{J}$.
- The estimate for the system state x will oscillate between a prior and posterior ensemble that both are fixed with respect to t. The oscillation magnitude of the prior and posterior means is given by (5.62).
- The larger the uncertainty in the observation, Γ, the smaller the oscillation magnitude, $H\bar{x}_f - H\bar{\hat{x}}_f$;
- The larger the uncertainty in the observation, Γ, the larger the final mean output reconstruction error, $H\bar{x}_f - \bar{y}$.

5.3.4 Example

Figure 5.3 plots the convergence of the system state for different observation uncertainties $\Gamma = 0.1$ and $\Gamma = 0.0001$. It shows that the oscillation magnitude is smaller in the case of $\Gamma = 0.1$ than that for $\Gamma = 0.0001$. The intuition behind this is that when the observation uncertainty Γ is smaller, the magnitude of the Kalman filter is larger. Therefore, the Kalman updates tend to be larger. It can also be shown that when Γ is smaller, the posterior after each Kalman update is closer to the line of $\bar{y} - Hx = 0$. This is because when the observation has less uncertainty, the reconstructed output Hx is more likely to approach to the observation $\bar{y}$.

5.4 The Ensemble Resampling Method

We herein propose an Ensemble Resampling Method (ERM) to prevent early stopping of IEnKF by resampling of the parameter ensemble. We provide a mathematical foundation for this approach by, first, showing that resampling perturbs the covariance shrinkage and consequently prevents the Kalman gain K_t from approaching to zero in the early iterations, and second, proposing a condition to ensure the deviation of the Kalman gain caused by the resampling remains small and asymptotically converges to zero. This condition ensures that the resampling not only prevents the early stopping, but also maintains the correct Kalman update direction. Finally, the influence of the higher order moments on the convergence of IEnKF is discussed.

5.4.1 Perturb Covariance Shrinkage with Resampling

To prevent early stopping of IEnKF, we need to prevent $C_{\hat{\theta}_t, H\hat{x}_t}$ (or Kalman gain K_t) from approaching to zero before the innovation is minimized. It is achieved by resampling the posterior ensemble of the parameter, $\left\{\theta_t^{(j)}\right\}_{j=1}^{J}$. This is equivalent to add a random deviation $\Delta_{r,t}^{(j)}$ to the jth posterior ensemble member before assigning to the prior ensemble member of the next step:

$$\hat{\theta}_{t+1}^{(j)} = \theta_t^{(j)} + \Delta_{r,t}^{(j)} = \hat{\theta}_t^{(j)} + K_t\left(y_t^{(j)} - H\hat{x}_t^{(j)}\right) + \Delta_{r,t}^{(j)} \ . \tag{5.64}$$

Derivations similar to (5.26) and (5.27) yields a similar evolution equation for the extended state z

$$\hat{z}_{t+1}^{(j)} = A_t\hat{z}_t^{(j)} + A_t\Delta_{y,t}^{(j)} + \tilde{\Lambda}_t^{(j)} \ , \tag{5.65}$$

except the additional term $\tilde{\Lambda}_t^{(j)}$ now takes a different form

$$\tilde{\Lambda}_t^{(j)} \doteq \begin{bmatrix} \Delta_{r,t}^{(j)} \\ \tilde{\Delta}_t^{(j)} \end{bmatrix}, \quad \tilde{\Delta}_t^{(j)} := \Delta_t^{(j)} + H\nabla F\left(\bar{\hat{\theta}}_{t+1}\right)\Delta_{r,t}^{(j)} \ , \tag{5.66}$$

which includes both the effects from the nonlinearity, $\Delta_t^{(j)}$, and the resampling process, $\Delta_{r,t}^{(j)}$. From the evolution equation (5.65), the evolution equation for the covariances can be obtained in the following form:

$$\begin{aligned}\begin{bmatrix} C_{\hat{\theta}_{t+1},\hat{\theta}_{t+1}} & C_{\hat{\theta}_{t+1},H\hat{x}_{t+1}} \\ C_{H\hat{x}_{t+1},\hat{\theta}_{t+1}} & C_{H\hat{x}_{t+1},H\hat{x}_{t+1}} \end{bmatrix} &= A_t \begin{bmatrix} C_{\hat{\theta}_t,\hat{\theta}_t} & C_{\hat{\theta}_t,H\hat{x}_t} \\ C_{H\hat{x}_t,\hat{\theta}_t} & C_{H\hat{x}_t,H\hat{x}_t} + \Gamma \end{bmatrix} A_t^T \\ &+ A_t \begin{bmatrix} C_{\hat{\theta}_t,\Delta_{r,t}} & C_{\hat{\theta}_t,\tilde{\Delta}_t} \\ C_{H\hat{x}_t,\Delta_{r,t}} & C_{H\hat{x}_t,\tilde{\Delta}_t} \end{bmatrix} + \begin{bmatrix} C_{\Delta_{r,t},\hat{\theta}_t} & C_{\Delta_{r,t},H\hat{x}_t} \\ C_{\tilde{\Delta}_t,\hat{\theta}_t} & C_{\tilde{\Delta}_t,H\hat{x}_t} \end{bmatrix} A_t^T \\ &+ \begin{bmatrix} C_{\Delta_{r,t},\Delta_{r,t}} & C_{\Delta_{r,t},\tilde{\Delta}_t} \\ C_{\tilde{\Delta}_t,\Delta_{r,t}} & C_{\tilde{\Delta}_t,\tilde{\Delta}_t} \end{bmatrix} . \end{aligned} \tag{5.67}$$

Note that, due to additional deviation caused by resampling, Δ_r, the fourth irreducible term has non-zero contributions to all four entries of the covariance matrix, i.e. none of $C_{\hat{\theta},\hat{\theta}}$, $C_{\hat{\theta},H\hat{x}}$ and $C_{H\hat{x},H\hat{x}}$ will converge to zero unless the nonlinear effect Δ_t and the resampling deviation $\Delta_{r,t}$ both approach to zero. Therefore the Kalman gain K_t will not approaches to zero in the early stage to cause early stopping of Kalman updates. The Kalman updates will be equal to zero only when the innovation $\bar{y} - H\hat{x}$ approaches to zero.

5.4.2 Small Deviation Condition for the Kalman Gain

It has already been shown in Section 5.4.1 that adding a resampling process between the update step and the prediction step can help to prevent the early stopping of Kalman filter updates by perturbing the covariance shrinkage via resampling. However, to ensure convergence of IEnKF, we also need to make sure the update "direction" is correct after resampling, i.e. the change of the Kalman gain is small after the resampling process. This is achieved by keeping the mean and covariance unchanged during the resampling process. The idea will be shown below.

For simplicity of notation, we define the parameter and state before resampling as random variables θ_t and x_t, the parameter and state after resampling as random variables $\theta_{r,t}$ and $x_{r,t}$, and the difference caused by resampling as

$$\Delta_{r,t} = \theta_{r,t} - \theta_t \ . \tag{5.68}$$

The relation between parameter and state is

$$x_t = F(\theta_t), \quad x_{r,t} = F(\theta_{r,t}) \ . \tag{5.69}$$

During the resampling process, the first and second moments of the parameter θ are keep unchanged, that is,

$$E(\theta_{r,t}) = E(\theta_t) = \bar{\theta}_t, \quad Var(\theta_{r,t}) = Var(\theta_t) = \sigma_t^2 \ . \tag{5.70}$$

From this, the expectation and variance of $\Delta_{r,t}$ can be obtained as

$$E\left(\Delta_{r,t}\right) = E\left(\theta_{r,t}\right) - E\left(\theta_t\right) = 0 \,, \tag{5.71}$$
$$Var\left(\Delta_{r,t}\right) = Var\left(\theta_{r,t}\right) + Var\left(\theta_t\right) = 2\sigma_t^2 \,, \tag{5.72}$$

where independence of $\theta_{r,t}$ and θ_t is applied. The updates of iterative Kalman filter is determined by the innovation $y - Hx$ and the Kalman gains

$$\begin{aligned} K_t &= C_{\hat{\theta}_t\hat{x}_t} H^T \left(HC_{\hat{x}_t\hat{x}_t} H^T + \Gamma\right)^{-1} , \\ K_t' &= C_{\hat{x}_t\hat{x}_t} H^T \left(HC_{\hat{x}_t\hat{x}_t} H^T + \Gamma\right)^{-1} \,, \end{aligned} \tag{5.73}$$

which depend on the covariance matrices $C_{\hat{\theta}_t\hat{x}_t}$ and $C_{\hat{x}_t\hat{x}_t}$. The Kalman gain basically defines the "direction" of the updates. Therefore, in order to do correct updates, we need to make sure the Kalman gain is computed properly even after the resampling process. To see this, the differences of the covariances, $\left\|C_{\theta_{r,t},x_{r,t}} - C_{\theta_t,x_t}\right\|$ and $\left\|C_{x_{r,t},x_{r,t}} - C_{x_t,x_t}\right\|$, need to be checked.

Theorem 5.4.1. *Considering the iterative ensemble Kalman filter defined by the update step (6.19) and the prediction step (5.5), if the mean and variance of the parameter θ are kept unchanged during the resampling process described by (5.64), i.e.*

$$E\left(\theta_{r,t}\right) = E\left(\theta_t\right) = \bar{\theta}_t, \quad Var\left(\theta_{r,t}\right) = Var\left(\theta_t\right) = \sigma_t^2 \,.$$

then the deviations of the covariances have the following upper bounds

$$\left\|C_{\theta_{r,t},x_{r,t}} - C_{\theta_t,x_t}\right\| \leq 2\sqrt{2}M\sigma_t^2 \,, \tag{5.74}$$
$$\left\|C_{x_{r,t},x_{r,t}} - C_{x_t,x_t}\right\| \leq 2\sqrt{2}M^2\sigma_t^2 \,, \tag{5.75}$$

where the constant M is a uniform upper bound for the gradient of the forward model mapping $F(\theta)$, i.e.

$$\left\|F'(\theta)\right\| \leq M \,. \tag{5.76}$$

Proof. Assume the forward model $F(\theta)$ considered here is continuous on the closed interval $\left[\theta_t, \bar{\theta}_t\right]$ and differentiable on the open interval $\left(\theta_t, \bar{\theta}_t\right)$, where θ_t is an ensemble member at the step t and $\bar{\theta}_t$ is the ensemble mean. Here without loss of generality, we assume $\theta_t < \bar{\theta}_t$. Then based on the mean value theorem,

$$x_t = F\left(\theta_t\right) = F\left(\bar{\theta}_t\right) + F'(\theta_\eta)\left(\theta_t - \bar{\theta}_t\right) \tag{5.77}$$

where θ_η is some value in the open interval $\left(\theta_t, \bar{\theta}_t\right)$. Taking expectation of the above equation yields

$$\bar{x}_t = E\left(F\left(\theta_t\right)\right) = F\left(\bar{\theta}_t\right) + E\left(F'(\theta_\eta)\left(\theta_t - \bar{\theta}_t\right)\right) \,. \tag{5.78}$$

Therefore the deviation of the ensemble member from the ensemble mean is

$$x_t - \bar{x}_t = F'(\theta_\eta)\left(\theta_t - \bar{\theta}_t\right) - E\left(F'(\theta_\eta)\left(\theta_t - \bar{\theta}_t\right)\right) \ . \tag{5.79}$$

Making use of the upper bound on $F'(\theta)$, we can obtain an upper bound on the variance of the state before resampling as below

$$\begin{aligned} E\left(x_t - \bar{x}_t\right)^2 &= E\left(F'(\theta_\eta)\left(\theta_t - \bar{\theta}_t\right) - E\left(F'(\theta_\eta)\left(\theta_t - \bar{\theta}_t\right)\right)\right)^2 \\ &= E\left(F'(\theta_\eta)\left(\theta_t - \bar{\theta}_t\right)\right)^2 - \left(E\left(F'(\theta_\eta)\left(\theta_t - \bar{\theta}_t\right)\right)\right)^2 \\ &\leq E\left(F'(\theta_\eta)\left(\theta_t - \bar{\theta}_t\right)\right)^2 \\ &\leq M^2 E\left(\theta_t - \bar{\theta}_t\right)^2 \\ &= M^2\sigma_t^2 \ . \end{aligned} \tag{5.80}$$

Similarly, an upper bound of the variance of the state after resampling can be obtained too,

$$E\left(x_{r,t} - \bar{x}_{r,t}\right)^2 \leq M^2\sigma_t^2 \ . \tag{5.81}$$

Because the ensemble member of the parameter before and after resampling are independent, the mean square difference between θ_t and $\theta_{r,t}$ can be computed as

$$\begin{aligned} E\left(\theta_{r,t} - \theta_t\right)^2 &= E\left(\theta_{r,t} - \bar{\theta}_t + \bar{\theta}_t - \theta_t\right)^2 \\ &= E\left(\theta_{r,t} - \bar{\theta}_t\right)^2 + E\left(\theta_t - \bar{\theta}_t\right)^2 \\ &= 2\sigma_t^2 \ . \end{aligned} \tag{5.82}$$

Applying the mean value theorem again, the difference between the states before and after resampling is

$$x_{r,t} - x_t = F'\left(\theta_\zeta\right)\left(\theta_{r,t} - \theta_t\right) \ , \tag{5.83}$$

where $\theta_\zeta \in (\theta_{r,t}, \theta_t)$. Here we again assume $\theta_{r,t} < \theta_t$ without loss of generality. Taking expectation of the above equation, we can obtain an upper bound for the expected mean square difference between $x_{r,t}$ and x_t

$$\begin{aligned} E\left(x_{r,t} - x_t\right)^2 &= E\left(F'\left(\theta_\zeta\right)\left(\theta_{r,t} - \theta_t\right)\right)^2 \\ &\leq M^2 E\left(\theta_{r,t} - \theta_t\right)^2 \\ &\leq 2M^2\sigma_t^2 \ . \end{aligned} \tag{5.84}$$

Based on (5.80), (5.81), (5.82) and (5.84) and applying Cauchy-Schwarz inequality, the upper bounds for the differences of covariances before and after resampling are

$$\begin{aligned}
&\left\|C_{\theta_{r,t},x_{r,t}} - C_{\theta_t,x_t}\right\| \\
&= \left\|C_{\theta_{r,t},x_{r,t}} - C_{\theta_{r,t},x_t} + C_{\theta_{r,t},x_t} - C_{\theta_t,x_t}\right\| \\
&\leq \left\|C_{\theta_{r,t},x_{r,t}} - C_{\theta_{r,t},x_t}\right\| + \left\|C_{\theta_{r,t},x_t} - C_{\theta_t,x_t}\right\| \\
&= \left\|E\left(\theta_{r,t} - \bar{\theta}_t\right)\left(x_{r,t} - x_t\right)\right\| + \left\|E\left(\theta_{r,t} - \theta_t\right)\left(x_t - \bar{x}_t\right)\right\| \\
&\leq \sqrt{E\left(\theta_{r,t} - \bar{\theta}_t\right)^2 E\left(x_{r,t} - x_t\right)^2} + \sqrt{E\left(\theta_{r,t} - \theta_t\right)^2 E\left(x_t - \bar{x}_t\right)^2} \\
&\leq 2\sqrt{2}M\sigma_t^2 \ ,
\end{aligned} \tag{5.85}$$

$$\begin{aligned}
&\left\|C_{x_{r,t},x_{r,t}} - C_{x_t,x_t}\right\| \\
&= \left\|C_{x_{r,t},x_{r,t}} - C_{x_{r,t},x_t} + C_{x_{r,t},x_t} - C_{x_t,x_t}\right\| \\
&\leq \left\|C_{x_{r,t},x_{r,t}} - C_{x_{r,t},x_t}\right\| + \left\|C_{x_{r,t},x_t} - C_{x_t,x_t}\right\| \\
&= \left\|E\left(x_{r,t} - \bar{x}_{r,t}\right)\left(x_{r,t} - x_t\right)\right\| + \left\|E\left(x_{r,t} - x_t\right)\left(x_t - \bar{x}_t\right)\right\| \\
&\leq \sqrt{E\left(x_{r,t} - \bar{x}_{r,t}\right)^2 E\left(x_{r,t} - x_t\right)^2} + \sqrt{E\left(x_{r,t} - x_t\right)^2 E\left(x_t - \bar{x}_t\right)^2} \\
&\leq 2\sqrt{2}M^2\sigma_t^2 \ .
\end{aligned} \tag{5.86}$$

□

From previous derivation, a similar variance update equation for the parameter θ can be obtained,

$$C_{\hat{\theta}_{r,t+1},\hat{\theta}_{r,t+1}} = C_{\hat{\theta}_{r,t},\hat{\theta}_{r,t}} - C_{\hat{\theta}_{r,t},H\hat{x}_{r,t}}\left(C_{H\hat{x}_{r,t},H\hat{x}_{r,t}} + \Gamma\right)^{-1} C_{H\hat{x}_{r,t},\hat{\theta}_{r,t}} \ , \tag{5.87}$$

except that the variables here are the those after the resampling process. If the special case where θ and Hx are all scalars, the relation is reduced to:

$$\sigma_{t+1}^2 = \sigma_t^2 - \frac{C_{\hat{\theta}_{r,t},H\hat{x}_{r,t}} C_{H\hat{x}_{r,t},\hat{\theta}_{r,t}}}{C_{H\hat{x}_{r,t},H\hat{x}_{r,t}} + \Gamma} \ . \tag{5.88}$$

From the monotone convergence theorem, it can also be obtained that the sequence $\{\sigma_t\}_{t=1}^{\infty}$ is convergent, and we can denote the limit as σ_*. Because of the additional random disturbance added by resampling $\Delta_{r,t}$, the covariance $C_{\hat{\theta}_{r,t},H\hat{x}_{r,t}}$ will not be equal to zero unless $\Delta_{r,t} = 0$ (i.e. $\sigma_t = 0$ based on Eq. (5.72)). Mathematically, this is equivalent to: there exists a non-negative function $g(\cdot)$ such that

$$\left|C_{\hat{\theta}_{r,t},H\hat{x}_{r,t}}\right| \geq g\left(\sigma_t\right) > 0, \ \forall \sigma_t \neq 0, \tag{5.89}$$

and $g(\sigma_t) = 0$ only when $\sigma_t = 0$. Then Eq. (5.88) can be converted to

$$\sigma_{t+1}^2 \leq \sigma_t^2 - cg^2(\sigma_t) \ , \tag{5.90}$$

where $c > 0$ is some constant to take account the effect of the denominator of the second term on the right hand side of Eq. (5.88). Then taking limits on both hand sides of the above inequality as $t \to \infty$ yields

$$\sigma_*^2 \leq \sigma_*^2 - cg^2(\sigma_*) \Rightarrow g^2(\sigma_*) \leq 0 \Rightarrow g(\sigma_*) = 0 \ . \tag{5.91}$$

Because zero is the only stationary point of $g(\cdot)$, it can be obtained that $\sigma_* = 0$, i.e.

$$\lim_{t\to\infty} \sigma_t^2 = 0 \ . \tag{5.92}$$

Therefore, based on (5.85), as the iteration step t increases, the difference between $C_{\theta_{r,t},x_{r,t}}$ and C_{θ_t,x_t} will be very small and asymptotically converges to zero as t increases. Similar conclusions hold true for the difference between $C_{x_{r,t},x_{r,t}}$ and C_{x_t,x_t}. This indicates that except at the early stage of the iteration process, the change of the Kalman gains will remain small and asymptotically converge to zero if the mean and the covariance of the parameter ensemble are kept the same before and after the resampling process.

To verify the conclusion above, IEnKF with resampling is applied to the test example defined in Equation (5.9) - Equation (5.10). Gaussian distribution is used as the resampling distribution. Figure 5.4 shows the evolution of the covariances with resampling implemented. Compared to the results without resampling, the covariance $C_{\hat{\theta},H\hat{x}}$ and the Kalman gain K_t will not approach to zero in the early stage to cause $C_{\hat{\theta},\hat{\theta}}$ and $C_{H\hat{x},H\hat{x}}$ stop updating. Instead, all covariances converge to zero simultaneously and roughly at the same time that the magnitude of the innovation $\|\bar{y} - H\hat{x}\|$ converges to zero (see Figure 5.5). This indicates that the "early stopping" of standard IEnKF is prevented by resampling as comparing to the simulations without resampling where the Kalman gain K_t converges to zero before the innovation is minimized (i.e. converges to zero).

Figure 5.4(a) also shows that $C_{\hat{\theta},\hat{\theta}}$ converges to zero as t increases. This verifies the argument we made in Equation (5.92), and along with Theorem 5.4.1, leads to the conclusion that the change of the Kalman gain after resampling will remain small and asymptotically converge to zero. This conclusion is numerically verified by results shown in Figure 5.6, i.e. the difference of the Kalman gain before and after resampling quickly decreases, remains bounded by a small quantity, and ultimately converges to zero as t increases.

Figure 5.7 and Figure 5.8 show the solution path with resampling implemented in the x and θ space respectively. They both show that the "early stopping" of IEnKF is prevented and the solutions are able to converge to the true solution. Note that there are multiple local minima for the test problem and the solution only converges to one of them depending on the initial condition given. More information needs to be provided if we want to pick out a particular local minimum.

In summary, the resampling process helps to prevent the "early stopping" of iterative ensemble Kalman filter by preventing the Kalman gain K_t from approaching to zero before

the innovation is reduced to zero. On the other hand, Theorem 5.4.1 gives the small deviation condition of the Kalman Gain for resampling, that is, by keeping the mean and covariance of the parameter ensemble unchanged during the resampling process, the Kalman gain is almost kept unchanged after the resampling to ensure the update "direction" is correct.

5.4.3 Influence of Higher Order Moments on Convergence

In Section 5.4.1 and Section 5.4.2, we have shown how to use resampling to prevent the early stopping of iterative ensemble Kalman filter and improve its convergence. Gaussian distribution is used during the resampling process while the first and second order moments are kept unchanged. However, other distributions with different higher order moments can also be used to resample the ensemble. Because it is meaningless to consider the skewness (the third order moment) of the resampling distribution without prior knowledge, we here mainly discuss the influence of kurtosis (the fourth order moment) on the convergence of iterative ensemble Kalman filter. Three different resampling distributions are considered here (see Figure 5.9):

- Uniform distribution: kurtosis = 1.8;
- Gaussian distribution: kurtosis = 3;
- Laplace distribution: kurtosis = 6.

The skewness of all the above distributions is equal to zero, and the mean and variance are set to be the same as the ensemble before resampling. The numerical simulation results for the above resampling distributions are shown in Figure 5.10, which yield two major take-home messages:

- Larger kurtosis makes the convergence more oscillatory. In Figure 5.10, the main trends of the convergence for uniform and gaussian resampling (smaller kurtosis) are almost monotonic while the convergence for Laplace resampling (larger kurtosis) is rather oscillatory. This is because the distribution with larger kurtosis is more likely to generate outliers, which will reflect as more fluctuations in the ensemble mean estimation of the parameter. However, this is not necessarily a disadvantage as this naturally adds more mutation into the solution at each iteration and may help the solution to jump out of the local minima and converge to the global minimum.
- Smaller kurtosis accelerates the convergence rate. It can also be observed in Figure 5.10 that Laplace resampling (with the largest kurtosis) yields the largest iteration number for convergence (about 1200 steps). Even comparing uniform resampling and Gaussian resampling which yield almost the same convergence iteration steps (about 600 steps), we can find that gaussian resampling (with larger kurtosis) takes more iteration steps to converge to the neighborhood of local minimums around $(-1, -1)$ than uniform resampling. This is because resampling distribution with smaller kurtosis is less likely

to generate extreme outliers and most of the new ensembles will be near the ensemble mean, which is in general a better estimator of the parameter value than an individual ensemble member. Therefore smaller kurtosis tends to accelerate the convergence.

In summary, larger kurtosis for resampling distribution adds more mutations in the solution at each step, and smaller kurtosis concentrates ensemble members more around the ensemble mean and thus speeds up the convergence if the ensemble mean is a good estimator of the solution. However, there is no short answer for whether smaller or larger kurtosis is good or not. The influence of the kurtosis and higher order moments of the resampling distribution needs to be further investigated.

5.5 Conclusion

Herein a comprehensive study of the convergence of iterative ensemble Kalman filter is conducted and a potential method to improve its convergence was proposed. To motivate this work, we first showed the necessity of iterations for ensemble Kalman method to apply to nonlinear inverse problems by reformulating it as a constrained optimization minimizing the innovation $\|y - Hx\|$ while satisfying the forward model equation $x = F(\theta)$. Then the shrinking effect of the standard Kalman iterations on ensemble covariances was studied, and along with the nonlinearity of the forward model, was later shown to be the reason that caused the Kalman gain to approach to zero before innovation was minimized, i.e. the early stopping of IEnKF. To resolve this issue, we added an additional step at each iteration to resample the parameter posterior ensemble with the mean and covariance kept unchanged before assigning to the next iteration. The idea is to prevent early stopping by perturbing the shrinking of the ensemble covariances while still keeping the correct Kalman update directions. After that, we explored different resampling distributions and studied the effect of their higher order moments on the convergence of iterative ensemble Kalman filter. Numerical simulations are presented to reproduce the early stopping phenomenon and demonstrate the effectiveness of the proposed resampling method.

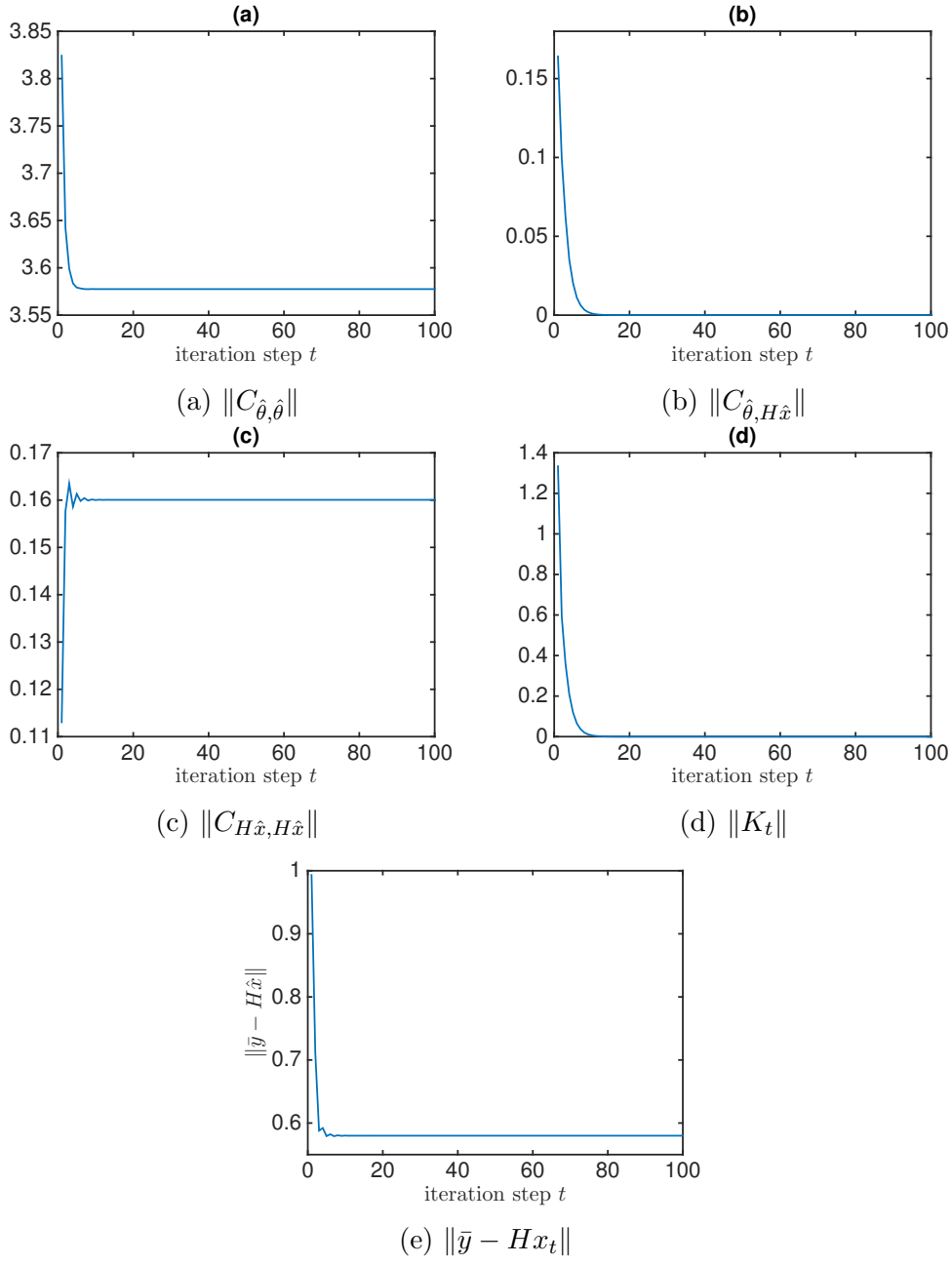

(a) $\|C_{\hat{\theta},\hat{\theta}}\|$ (b) $\|C_{\hat{\theta},H\hat{x}}\|$

(c) $\|C_{H\hat{x},H\hat{x}}\|$ (d) $\|K_t\|$

(e) $\|\bar{y} - Hx_t\|$

Figure 5.2: Evolution of the norms of the covariances, Kalman gain and innovation for the IEnKF applied to the example in §5.2.4.

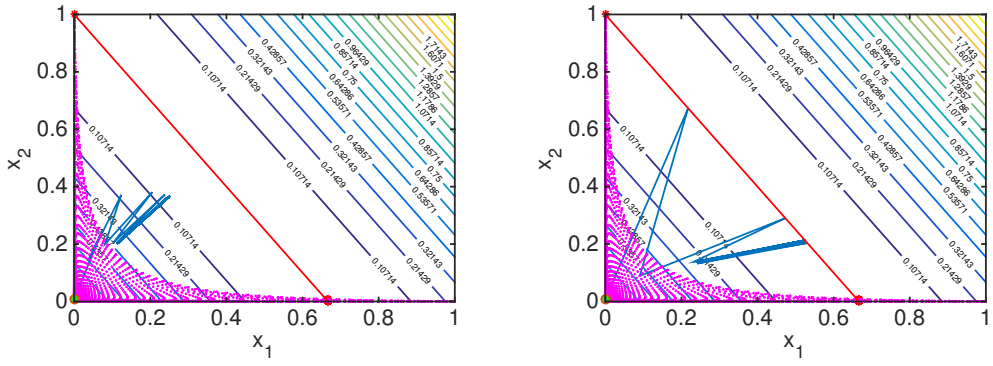

Figure 5.3: (Left) the solution path of the ensemble mean of x when $\Gamma = 0.1$. (Right) the solution path of the ensemble mean of x when $\Gamma = 0.0001$.

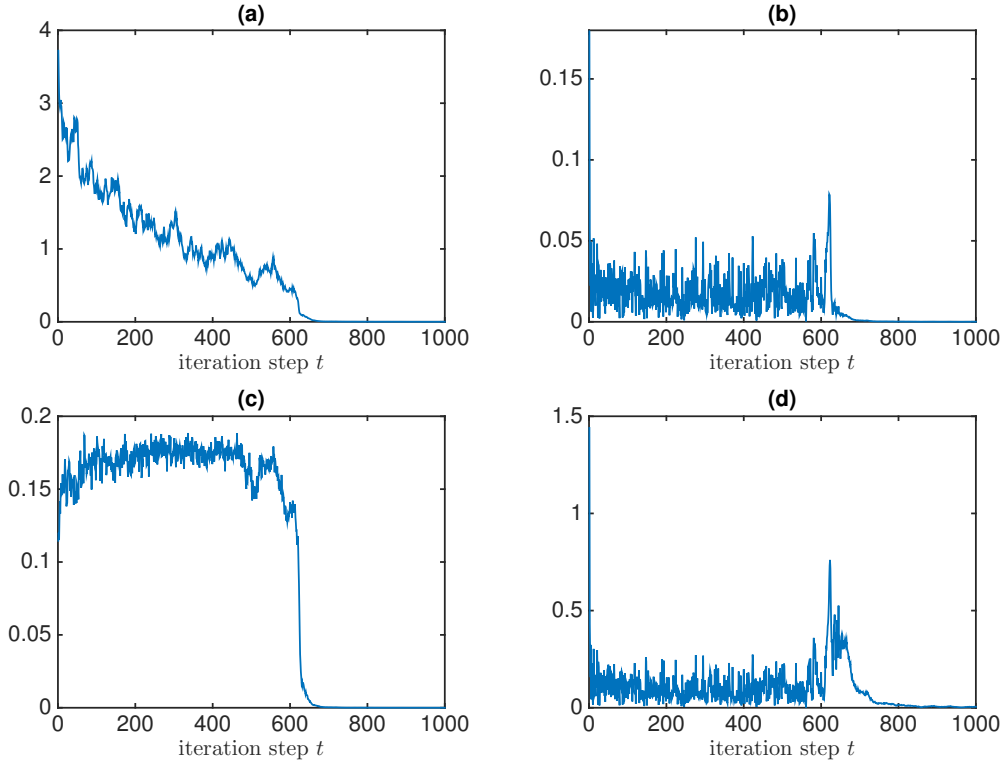

Figure 5.4: The evolution of the norms of the covariances and the Kalman gain with resampling implemented. (a): $\left\|C_{\hat{\theta},\hat{\theta}}\right\|$, (b): $\left\|C_{\hat{\theta},H\hat{x}}\right\|$, (c): $\|C_{H\hat{x},H\hat{x}}\|$, (d): $\|K_t\|$

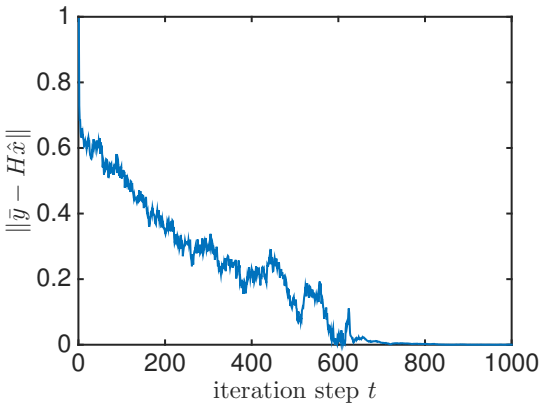

Figure 5.5: The evolution of the magnitude of innovation $\|\bar{y} - H\hat{x}\|$ with resampling implemented.

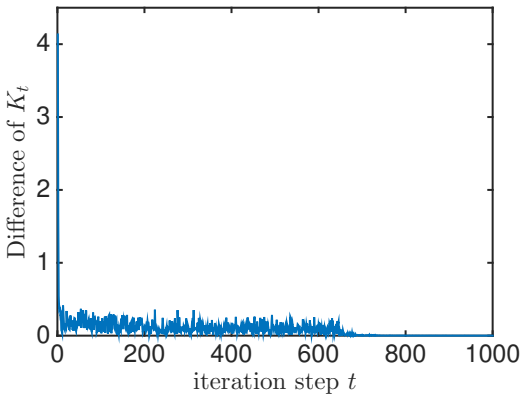

Figure 5.6: The difference between the Kalman gains before resampling $K_{t,before}$ and after resampling $K_{t,after}$.

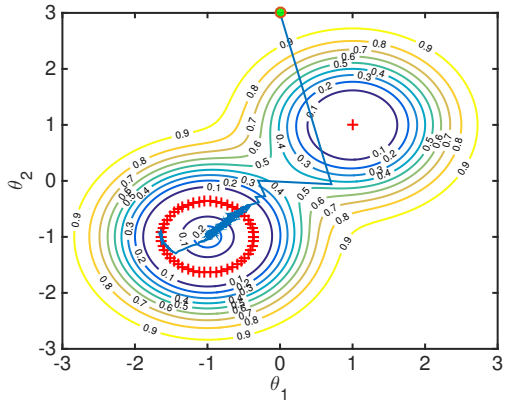

Figure 5.7: The solution path of the ensemble mean of θ with resampling implemented. The red "+" represent the θ values that minimize $\|\bar{y} - HF(\theta)\|^2$. The green circle denotes the starting point.

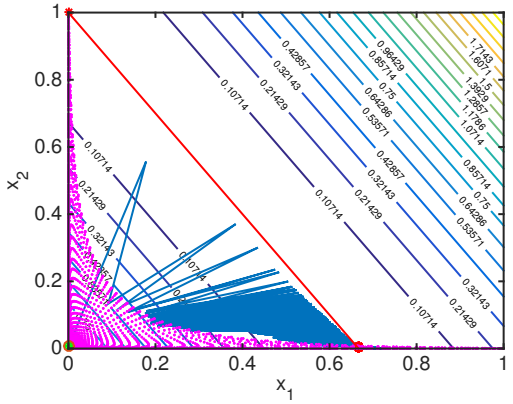

Figure 5.8: The solution path of the ensemble mean of x with resampling implemented. The red line in the middle represents the level sets of $\bar{y} - Hx = 0$. The dotted region in the lower left corner represents the image of the forward mapping $F(\cdot)$. The green circle denotes the starting point.

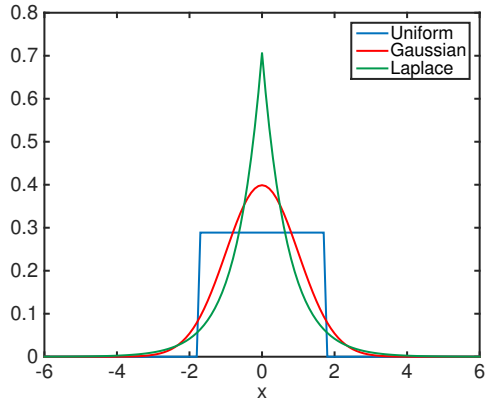

Figure 5.9: The probability density functions of the three distributions used for resampling. Uniform distribution: kurtosis = 1.8 . Gaussian distribution: kurtosis = 3 . Laplace distribution: kurtosis = 6 .

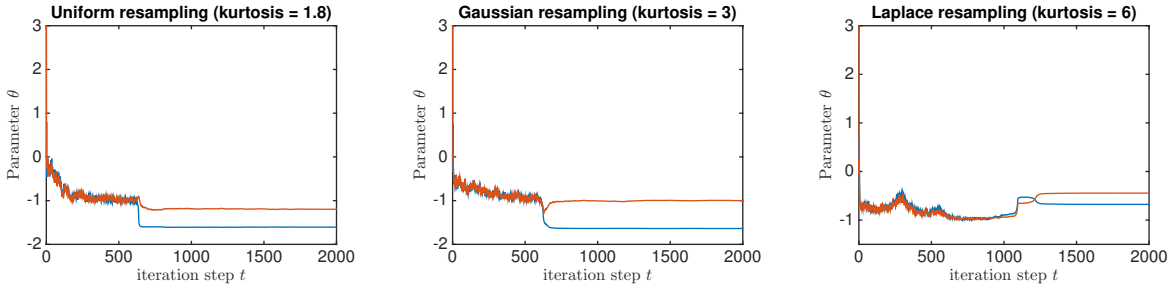

Figure 5.10: The convergence of parameter θ estimation with different resampling distributions implemented. (Left) Uniform distribution. (Middle) Gaussian distribution. (Right) Laplace distribution.

Chapter 6

Adding Constraints to Bayesian Inverse Problems

6.1 Introduction

Inverse problems are often ill-posed due to limited measurement data, and thus the solution for the hidden unknown parameters are not unique. Adding additional constraints from prior knowledge to the inverse problems can be a potential solution. However, most existing Bayesian methods can not directly take constraints into account [106]. Initial progress has been made to incorporate constraints into certain Bayesian filters. For example, Simon et al. [109] considered equality constraints in the standard Kalman filter by projecting the Kalman updated solution onto the state constraint surface. Shao et al. [106] developed a constrained sequential Monte Carlo algorithm based on acceptance/rejection and an optimization strategy. Most recently, Gardner et al. [50] also considered inequality constraints in the context of Bayesian optimization. However, the existing approaches to incorporate constraints have been developed for each specific Bayesian filter, and most of them are based on a linearized form of the constraints, which is limiting when constraint functions are complicated and highly nonlinear. Moreover, in many complex systems, the constraints are approximations to reality and formulating the constraint in a deterministic way may neglect the uncertainties associated with constraint itself.

In this work, we proposed a general approach to incorporate physics-based constraints into the Bayesian inversion framework, where uncertainty associated with the constraint itself can also been considered. Moreover, this idea is also extended to an approximate Bayesian approach–the ensemble Kalman filter.

6.2 Methodology

A mathematical model of system defines a *forward problem* that can be formulated as

$$\mathbf{x} = F(\theta), \tag{6.1}$$

where $\theta \in \mathbb{R}^{d_\theta}$ are model parameters and $\mathbf{x} \in \mathbb{R}^{d_x}$ are the states of the system. The forward operator F is nominally assumed to describe a physical system, whereby F typically represents a suite of algebraic and/or differential equations. In most cases, the model parameters θ are uncertain or unknown, and the state variables $\mathbf{x}$ are largely unobservable. Therefore, the unknown parameters and hidden states need to be inferred from observations $\mathbf{y} \in \mathbb{R}^{d_y}$. These observations indirectly and incompletely describe the state of the system, which can be formulated mathematically as

$$\mathbf{y} = H\mathbf{x} + \epsilon, \tag{6.2}$$

where H is a projection operator projecting the full state to the observed space and ϵ represents measurement error. The standard inverse problem deals with estimating the unknown parameters θ (or the hidden states x) based on the observations y. In practice, approximate Bayesian inversion frameworks, such as Kalman filtering and Sequential Monte Carlo, are used for computational efficiency.

6.2.1 Constraints in Exact Bayesian Inference

Inverse problems are typically ill-posed because the observational data is not sufficient to uniquely determine the unknown parameters. Thus, specification of additional constraints can be useful to regularize the inverse problem. Equality constraints can be defined with respect to the state variables x as,

$$G(x) = \left[g_1(x), g_2(x), ..., g_{d_g}(x)\right]^T = \mathbf{0}\ , \tag{6.3}$$

where $g_i(x), i = 1, 2, ..., d_g$ represent different equality constraints. In many application, the constraint only approximates reality. Thus, instead of directly imposing a hard constraint, we assume that each constraint satisfies a zero-mean Gaussian distribution, expressed as

$$G(x) \sim \mathcal{N}(\mathbf{0}, \Sigma_c)\ . \tag{6.4}$$

where the Σ_c is a covariance matrix used to control the strictness of each constraint. Since x is intrinsically a function of θ, the constraints can alternatively be expressed in terms of the parameters

$$G(x) = G(F(\theta)) \sim \mathcal{N}(\mathbf{0}, \Sigma_c)\ . \tag{6.5}$$

As such, these constraints on the parameters θ can be more naturally considered within the Bayesian framework by imposing additional likelihood functions introduced by these nondeterministic constraints.

Without loss of generality, both the prior and likelihood are assumed Gaussian. Namely, the prior of the parameters θ is defined by

$$p(\theta) = \frac{1}{\sqrt{(2\pi)^{d_\theta}|\Sigma_\theta|}} \exp\left(-\frac{1}{2}(\theta - \hat{\theta})^T \Sigma_\theta^{-1} (\theta - \hat{\theta})\right)\ , \tag{6.6}$$

where $\hat{\theta}$ and Σ_θ are the prior mean and covariance, which are based on existing knowledge or preliminary estimation. The observation data errors are also assumed to follow a zero-mean Gaussian distribution, i.e., $\epsilon \in N(0, \Sigma_l)$, thus the likelihood of the observed data set on y is,

$$p(\mathcal{D}|\theta) = \frac{1}{\sqrt{(2\pi)^{d_y}|\Sigma_l|}} \exp\left(-\frac{1}{2}(y - HF(\theta))^T \Sigma_l^{-1}(y - HF(\theta))\right) . \tag{6.7}$$

The covariance matrix Σ_l is obtained by estimating the sample variance of the observed data sets $\mathcal{D}$. The constraints are imposed by considering the following likelihood function,

$$p\left(G(x) = \mathbf{0} \mid \theta\right) = \frac{1}{\sqrt{(2\pi)^{d_g}|\Sigma_c|}} \exp\left(-\frac{1}{2}G(F(\theta))^T \Sigma_c^{-1} G(F(\theta))\right) . \tag{6.8}$$

The likelihood of the constraints defines a fitness of a specific value of θ based on the satisfaction of the constraints. By introducing this Gaussian-type likelihood function, we enable a "soft" enforcement of the constraints. The strictness of the constraint can be controlled by the diagonal variance matrix Σ_c,

$$\Sigma_c = \text{diag}\{\sigma_{c,1}^2, \sigma_{c,2}^2, ..., \sigma_{c,d_g}^2\} . \tag{6.9}$$

where the variance σ_i represent a confidence on the accuracy of the constraint. Smaller $\sigma_{c,i}$ corresponds to a stricter constraint.

Inequality constraints can be converted to equivalent equality constraints. For example, a scalar inequality constraint $g(x) \leq 0$ can be expressed as

$$\max\left(0, g(x)\right) = 0 , \tag{6.10}$$

and thus the corresponding likelihood can be expressed as

$$p\left(g(x) \leq 0 \mid \theta\right) = \frac{1}{\sqrt{2\pi\sigma_c^2}} \exp\left(-\frac{1}{2\sigma_c^2}\left[\max\left(0, g(x)\right)\right]^2\right) . \tag{6.11}$$

Imposing constraints through a likelihood function can also be extended to disjunctive constraints. For example, consider a constraint of the form $g_1(x) = 0 \vee g_2(x) = 0$. By the union rule of probability

$$\begin{aligned}
&p\left(g_1(x) = 0 \vee g_2(x) = 0 \mid \theta\right) \\
&= p\left(g_1(x) = 0|\theta\right) + p\left(g_2(x) = 0|\theta\right) - p\left(g_1(x) = 0 \wedge g_2(x) = 0|\theta\right) \\
&= \frac{1}{\sqrt{2\pi\sigma_{c,1}^2}} \exp\left(-\frac{g_1(F(\theta))^2}{2\sigma_{c,1}^2}\right) + \frac{1}{\sqrt{2\pi\sigma_{c,2}^2}} \exp\left(-\frac{g_2(F(\theta))^2}{2\sigma_{c,2}^2}\right) \\
&- \frac{1}{\sqrt{(2\pi)^2|\Sigma_c|}} \exp\left(-\frac{1}{2}\begin{bmatrix} g_1(F(\theta)) \\ g_2(F(\theta)) \end{bmatrix}^T \Sigma_c^{-1} \begin{bmatrix} g_1(F(\theta)) \\ g_2(F(\theta)) \end{bmatrix}\right) ,
\end{aligned} \tag{6.12}$$

where Σ_c again defines the covariance matrix of constraints.

With the prior distribution, likelihood of the data, and likelihood of the constraints now defined, the posterior probability distribution conditioned on the observed data $\mathcal{D}$ and the constraints $G(x)$ can be defined as

$$\begin{aligned} p(\theta|\mathcal{D}, G(x) = \mathbf{0}) &= \frac{p(\mathcal{D}|\theta)p(G(x) = \mathbf{0}|\theta)p(\theta)}{p(\mathcal{D}, G(x) = \mathbf{0})} \\ &\propto p(\mathcal{D}|\theta)p(G(x) = \mathbf{0}|\theta)p(\theta) \ . \end{aligned} \tag{6.13}$$

Since the posterior distribution cannot be solved analytically in general, it is commonly evaluated based on MCMC sampling.

6.2.2 Constraints in Approximate Bayesian Inference

The direct Bayesian inference based on MCMC sampling is usually intractable when the likelihood calculation involves a computationally expensive model; instead approximate Bayesian approaches are commonly used to provide a more computationally tractable solution. The EnKF is one such method, which is a variant of the standard Kalman filter where the covariance matrix is replaced by Monte Carlo samples.

For EnKF, we combine the original hidden states x and the unknown parameters θ into a new augmented state

$$z = \left[\theta^T, x^T\right]^T \ , \tag{6.14}$$

which will be updated during the filtering process according to the observed data $\mathcal{D}$. The initial ensemble is first obtained by sampling the prior distribution $p(\theta)$ and evaluating the model at each ensemble member

$$\left\{\hat{z}^{(j)}\right\}_{j=1}^{J} = \left\{\left[\hat{\theta}^{(j)}; \hat{x}^{(j)}\right]^T\right\}_{j=1}^{J} = \left\{\left[\hat{\theta}^{(j)}; F\left(\hat{\theta}^{(j)}\right)\right]^T\right\}_{j=1}^{J} \ , \tag{6.15}$$

where J is the number of ensemble members. The probability associated with each ensemble member is initially set to be uniform

$$w_j \triangleq p(z = \hat{z}^{(j)}) = \frac{1}{J}, \quad j = 1, 2, ..., J \ . \tag{6.16}$$

Then the expectation and covariance matrix of the state variables are estimated from the ensemble as

$$\mathbb{E}(\hat{z}) = \sum_{j=1}^{J} w_j \hat{z}^{(j)} \ , \tag{6.17}$$

$$\mathbb{C}(\hat{z}) = \sum_{j=1}^{J} w_j (\hat{z}^{(j)} - \mathbb{E}(\hat{z}))(\hat{z}^{(j)} - \mathbb{E}(\hat{z}))^T \ . \tag{6.18}$$

If the observed data follows a normal distribution $N(\bar{y}, \Sigma_l)$, the prior ensemble can be updated by the observed data $\mathcal{D}$ according to the Kalman update

$$z^{(j)} = \hat{z}^{(j)} + \mathbb{C}(\hat{z})H^T(H\mathbb{C}(\hat{z})H^T + \Sigma_l)^{-1}(\bar{y} - Hz^{(j)}), \\ j = 1, 2, ..., J \ . \tag{6.19}$$

The posterior ensemble $\left\{z^{(j)}\right\}_{j=1}^{J}$ represents a sampling for the posterior probability distribution $p(z|\mathcal{D})$, with the probability associated with each ensemble member equal to

$$p(z^{(j)}|\mathcal{D}) = w_j, \quad \forall j = 1, 2, ..., J \ . \tag{6.20}$$

Now we consider inclusion of constraints. The likelihood of the constraint $G(x) = \mathbf{0}$ to be satisfied conditioned on each member of the posterior ensemble can be computed as

$$\begin{aligned} Lg^{(j)} &\triangleq p\left(G(x) = \mathbf{0}|z^{(j)}\right) \\ &= \frac{1}{\sqrt{(2\pi)^{d_g}|\Sigma_c|}} \exp\left(-\frac{1}{2}G\left(x^{(j)}\right)^T \Sigma_c^{-1} G\left(x^{(j)}\right)\right) \ . \end{aligned} \tag{6.21}$$

By Bayes theorem, the posterior probability density of each ensemble member conditioned on the observed data $\mathcal{D}$ and constraints $G(x) = \mathbf{0}$ is given by

$$\begin{aligned} p\left(z^{(j)}|\mathcal{D}, G(x) = \mathbf{0}\right) &= \frac{1}{Z} p\left(G(x) = \mathbf{0}, z^{(j)}|\mathcal{D}\right) \\ &= \frac{1}{Z} p\left(G(x) = \mathbf{0}|z^{(j)}\right) p\left(z^{(j)}|\mathcal{D}\right) = \frac{1}{Z} w_j Lg^{(j)} \end{aligned} \tag{6.22}$$

where Z is the normalization constant defined as

$$Z = \sum_{j=1}^{J} p\left(G(x) = \mathbf{0}|x^{(j)}\right) p\left(x^{(j)}|\mathcal{D}\right) = \sum_{j=1}^{J} w_j Lg^{(j)} \ . \tag{6.23}$$

The empirical distribution for $p\left(z|\mathcal{D}, G(x) = \mathbf{0}\right)$ can be described by the posterior ensemble $\left\{z^{(j)}\right\}_{j=1}^{J}$, and the associated probability mass

$$p\left(z = z^{(j)}|\mathcal{D}, G(x) = \mathbf{0}\right) = \frac{w_j Lg^{(j)}}{\sum_{p=1}^{J} w_j Lg^{(p)}}, \quad \forall j = 1, 2, ..., J, \tag{6.24}$$

for each ensemble member. We here re-define the new weights for each ensemble members as

$$w_j' \triangleq \frac{w_j Lg^{(j)}}{\sum_{p=1}^{J} w_j Lg^{(p)}} \ . \tag{6.25}$$

The state estimation for the current iteration step is thus computed as the expectation of the empirical posterior distribution conditioned on the data $\mathcal{D}$ and the prior knowledge that $G(x) = \mathbf{0}$ according to

$$\begin{aligned}\bar{z} = \mathbb{E}\left(z|\mathcal{D}, G(x) = \mathbf{0}\right) &= \sum_{j=1}^{J} p\left(z = z^{(j)}|\mathcal{D}, G(x) = \mathbf{0}\right) z^{(j)} \\ &= \sum_{j=1}^{J} w_j' z^{(j)} \ . \end{aligned} \tag{6.26}$$

Then the estimation of the unknown parameters $\bar{\theta}$ can be extracted from the estimation of the full augmented state. Also, the covariance of the parameter θ with respect to $p\left(z|\mathcal{D}, G(x) = \mathbf{0}\right)$ can be computed as

$$\Sigma_\theta = \sum_{i=1}^{J} \left(\theta^{(j)} - \bar{\theta}\right) \mathrm{diag}\left\{w_j'\right\}_{j=1}^{J} \left(\theta^{(j)} - \bar{\theta}\right)^T \ . \tag{6.27}$$

The new prior ensemble for the next iteration step is obtained by sampling the following normal distribution

$$\hat{\theta}^{(j)} \sim N(\bar{\theta}, \Sigma_\theta), \quad j = 1, 2, ..., J \ , \tag{6.28}$$

to maximize the next step prior entropy [91] while keeping the mean and covariance the same as the previous posterior distribution. The iterative process continues until a stopping criterion is satisfied or the maximum iteration number is reached.

6.3 Results and Discussion

6.3.1 Model Test Problem

To verify the effectiveness of the constrained Bayesian inference framework described above, a simple test case is presented here. The forward model mapping from the parameter space $\Theta \subset \mathbb{R}^2$ to the state space $X \subset \mathbb{R}^2$ is defined as

$$\begin{bmatrix} x_1 \\ x_2 \end{bmatrix} = F(\theta) = \begin{bmatrix} \exp(-(\theta_1 + 1)^2 - (\theta_2 + 1)^2) \\ \exp(-(\theta_1 - 1)^2 - (\theta_2 - 1)^2) \end{bmatrix} \ . \tag{6.29}$$

The projection matrix mapping from state space to output is given by

$$H = [-1.5, -1.0] \ , \tag{6.30}$$

and thus the reconstructed output is

$$\begin{aligned} HF(\theta) = &-1.5 \exp(-(\theta_1 + 1)^2 - (\theta_2 + 1)^2) \\ &- 1.0 \exp(-(\theta_1 - 1)^2 - (\theta_2 - 1)^2) \ , \end{aligned} \tag{6.31}$$

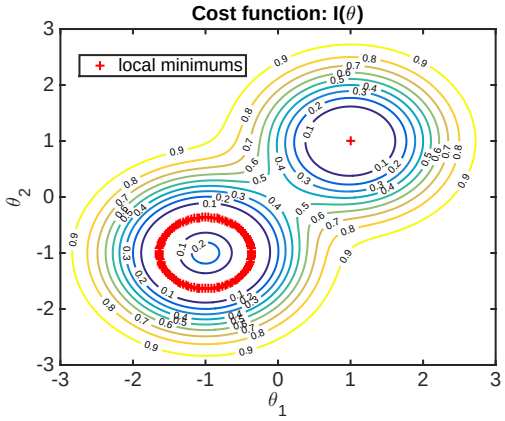

Figure 6.1: Contour plot of the cost function $I(\theta)$ with respect to parameters $\theta = [\theta_1, \theta_2]$ The red "+" denote the local minima of the cost function.

where $HF(\theta) \in \mathbb{R}^1$. We consider the following constraint:

$$G(x) = -0.25 \log x_1 + 0.25 \log x_2 - 2 = 0 \ , \tag{6.32}$$

which can be equivalently written in terms of θ,

$$G(F(\theta)) = \theta_1 + \theta_2 - 2 = 0 \ . \tag{6.33}$$

We assume the observed data follow the normal distribution $N(\bar{y}, \Sigma_l)$ where the mean $\bar{y} = -1.0$ and the covariance matrix Σ_l is chosen based on the uncertainty associated with data.

This model is chosen to create a simple scenario with multiple local minimums. Namely, regardless of the prior information and constraints, we seek the model parameters that minimize the difference between the observed output and reconstructed output, quantified by the cost function

$$\begin{aligned} I(\theta) &= \|\bar{y} - HF(\theta)\|^2 \\ &= \big(1.5 \exp(-(\theta_1 + 1)^2 - (\theta_2 + 1)^2) \\ &\quad + 1.0 \exp(-(\theta_1 - 1)^2 - (\theta_2 - 1)^2) - 1.0\big)^2 \ . \end{aligned} \tag{6.34}$$

which has minimums at (a) $\theta^* = (1, 1)$; and (b) θ on the circle defined by

$$(\theta_1 + 1)^2 + (\theta_2 + 1)^2 = \log 1.5 \ . \tag{6.35}$$

The contour plot of the cost function and the local minimums are visualized in Figure 6.1. Here we assume $\theta^* = (1, 1)$ is the true value of the parameter θ, and the constraint (6.33) will help to eliminate convergence to other local minima.

The situation of multiple local minima is a common challenge in solving inverse problems, because the observed output information is usually not enough to uniquely determine the unknown parameters. We show below that imposing constraints can help the solution to converge to the true value.

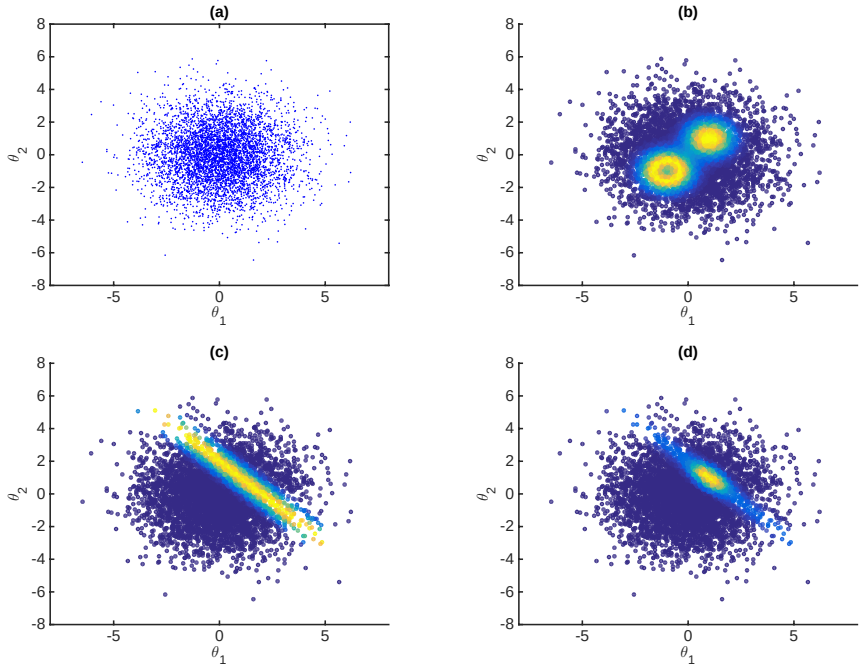

Figure 6.2: (a) Sampling of the prior distribution; (b) Sample + data likelihood $p(\mathcal{D}|\theta)$; (c) Sample + constraint likelihood $p(G(x) = \mathbf{0}|\theta)$; (d) Sample + posterior distribution $p(\theta|\mathcal{D}, G(x) = \mathbf{0})$

	θ_1	θ_2	x_1	x_2	y
True values	1	1	0	1	-1
No constraint	-0.0448	-0.0722	0.1698	0.1063	-0.3610
With constraints (EXP)	0.9926	0.9449	0.0004	0.9969	-0.9976
With constraints (MAP)	0.9845	0.9698	0.0004	0.9988	-0.9994

Table 6.1: Parameters θ, states x and output y estimated using sample-based Bayesian inference with no constraint imposed and with constraint imposed.

6.3.2 Exact Bayesian Inference

The prior distribution (6.6) is first sampled with $J = 5000$ samples. The mean and the covariance matrix are set to

$$\hat{\theta} = \begin{bmatrix} 0 \\ 0 \end{bmatrix}, \quad \Sigma_\theta = \begin{bmatrix} 3 & 0 \\ 0 & 3 \end{bmatrix} . \tag{6.36}$$

The distribution of the samples is visualized in Figure 6.2(a). The trivial zero mean represents non-informative prior knowledge of θ, and the large variance defined by Σ_θ above denotes large uncertainty about the prior. Ideally if better prior knowledge exists, we can

specify a better prior here, with more accurate mean and less uncertainty. After sampling the prior, the likelihood function of data $p(\mathcal{D}|\theta)$ is evaluated at each individual sample point $\left\{\theta^{(j)}\right\}_{j=1}^{J}$. The likelihood of the data is plotted with respect to each sample in Figure 6.2(b). The value of the likelihood is indicated by the brightness of the sample. It can be clearly observed that the brightest regions coincide with the local minimums in Figure 6.1, which shows the region of the highest likelihood of data . Similarly, we evaluate the likelihood function of the constraint $p(G(x) = \mathbf{0}|\theta)$ at each sample, and the likelihood is visualized in Figure 6.2(c). The region with the highest likelihood represents the form of the constraint in (θ_1, θ_2) space, which is $\theta_1 + \theta_2 - 2 = 0$. The variance for the constraint is set to be $\Sigma_c = 0.5$, which controls how strict the constraint is enforced. Lastly, the posterior $p(\theta|\mathcal{D}, G(x) = \mathbf{0})$ is evaluated at each samples, and the distribution of the sample along with the posterior weights are plotted in Figure 6.2(d). It is clearly observed that the location with the highest posterior density correspond to the intersection between the regions with high likelihood of data $\mathcal{D}$ and high likelihood of the constraint satisfaction. This intersection region picks out the true value of the parameter θ. Computing the weighted sum of the parameter samples $\left\{\theta^{(j)}\right\}_{j=1}^{J}$ with respect to the posterior weights yields the final estimation of the unknown parameter $\theta^*_{\text{Exp}} = \sum_{j=1}^{J} p\left(\theta^{(j)}|\mathcal{D}, G(x) = \mathbf{0}\right)\theta^{(j)} = \sum_{j=1}^{J} w_j\theta^{(j)}$. Or simply taking the sample $\theta^{(j)}$ that maximize the posterior $p\left(\theta^{(j)}|\mathcal{D}, G(x) = \mathbf{0}\right)$ yields the maximum a posteriori estimation (MAP) of the unknown parameter, i.e. θ^*_{MAP}. Once the parameter is estimated, the estimated value of the state variables x and output y can be computed by evaluating the forward model $F(\theta^*)$. These estimated values are listed in Table 6.1 for the case of including and not including constraint. It can be seen from this table that imposing the constraint significantly increase the estimation accuracy in the case where multiple local minimums exist.

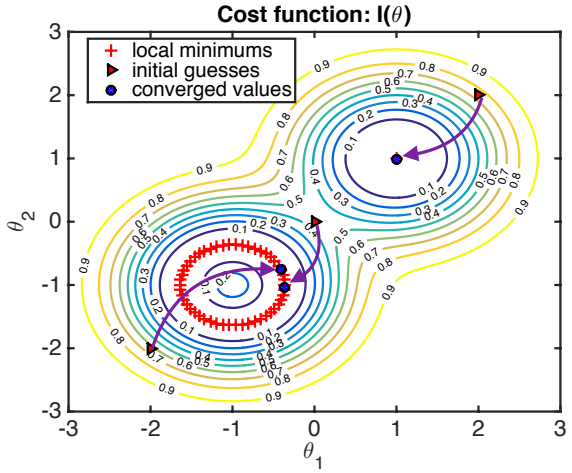

Figure 6.3: Different initial guesses of the unknown parameter θ (marked with red triangles) and their corresponding converged values after 1000 EnKF iteration steps (marked with blue circles), with no constraint imposed.

6.3.3 Approximate Bayesian Inference

6.3.3.1 No constraint imposed.

Iterative ensemble Kalman filter estimates the unknown model parameters θ in a iterative manner. Since the cost function $I(\theta)$ has multiple local minimums, different initial guesses of θ will converge to different local minimums. We here define

$$\text{Group I} \triangleq \left\{\theta^* \in \mathbb{R}^2 | \theta^* = (1,1)\right\} , \tag{6.37}$$

$$\text{Group II} \triangleq \left\{\theta^* \in \mathbb{R}^2 | (\theta_1^* + 1)^2 + (\theta_2^* + 1)^2 = \log 1.5\right\} , \tag{6.38}$$

which represent two different local minimum regions. θ^* represents the converged value of the parameter after ensemble Kalman filter iterations.

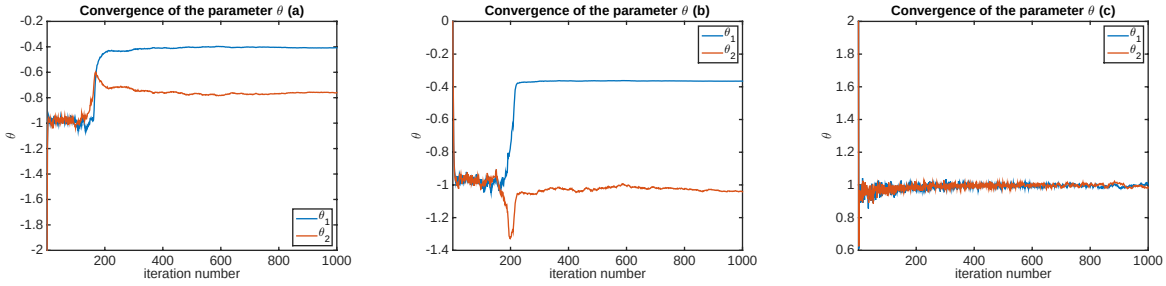

Figure 6.4: Results for the convergence of the parameter θ with no constraint imposed. (a) Initial guess: $\theta^0 = (-2, -2)$; (b) initial guess: $\theta^0 = (0, 0)$; (c) initial guess: $\theta^0 = (2, 2)$.

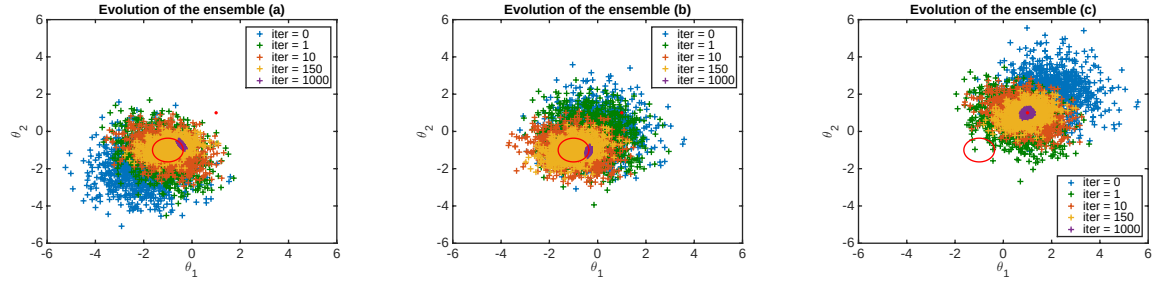

Figure 6.5: Evolution of the ensemble of the parameter θ with no constraint imposed. The points on the red circle centered at (-1,-1) and the red point at (1,1) denote the local minimums of the cost function $I(\theta)$. (a) Initial guess: $\theta^0 = (-2, -2)$; (b) initial guess: $\theta^0 = (0, 0)$; (c) initial guess: $\theta^0 = (2, 2)$.

Here we simulated three different cases with different initial guesses: (a) $\theta^0 = (-2, -2)$; (b) $\theta^0 = (0, 0)$; (c) $\theta^0 = (2, 2)$. The covariance matrix of the prior and the covariance of the data likelihood are given as $\Sigma_\theta = [1, 0; 0, 1]$ and $\Sigma_l = 0.01$. The results for the three different simulations are visualized in the parameter space of θ in Figure 6.3. It can be seen that the

upper right initial guess at $(2, 2)$ converges to local minimum Group I, and the other two initial guesses both converge to local minimum Group II. The convergence processes of the parameter θ for the three different initial guesses are plotted in Figure 6.4. It can be seen that all converge to the corresponding local minimum groups within about 400 iterations. The main difference is that while Case (c) converges to the local minimum $(1, 1)$, i.e., Group I, directly after a few iterations, Case (a) and (b) converge to $\theta = (-1, -1)$ first, which is the center of the local minimum circle of Group II, and then shift to a local minimum on the circle of Group II at around the 200th iteration (indicated by the "jump"). The reason behind this is that we use the mean of the ensemble of each step as the estimated parameter value. When the ensemble converges to the local neighborhood of Group II, the mean of the ensemble will generally be the center of the local minimum circle because the high likely ensemble members are roughly symmetrically distributed around the center $(-1, -1)$. The mean of the ensemble will gradually shift to certain points on the circle based on the distribution of the ensemble members. The evolution of the ensemble for different initial guesses is shown in Figure 6.5. It can be seen that the variance of the ensemble gradually decrease until all ensemble members collapse to the corresponding local minimum.

The convergence results for the three different initial guesses are summarized here,

$$\begin{aligned}
\theta^0 = (-2, -2) &\to \theta^* = (-0.4080, -0.7598) \in \text{Group II} , \\
\theta^0 = (0, 0) &\to \theta^* = (-0.3654, -1.0421) \in \text{Group II} , \\
\theta^0 = (2, 2) &\to \theta^* = (0.9998, 0.9812) \in \text{Group I} .
\end{aligned}$$

The reconstructed outputs $HF(\theta^*)$ for the above cases all converge to the target value $\bar{y} = -1$ within 1000 EnKf iterations. However, with no constraint is imposed, the estimate of the parameter θ will converge to the closer local minimum group based on where the initial guesses are. The initial guess in the middle $(0, 0)$ converges to the local minimum Group II because Group II contains more local minimums than Group I, and therefore the the solution is more likely to converge to Group II when initial guess is in the middle. More broadly, there is no guarantee that the estimate of the parameter will converge to the the true parameter value $(1, 1)$.

6.3.3.2 With constraint imposed

For the local minimums in Group I and Group II, only the true parameter value $(1, 1)$ satisfies the constraint. We test here whether imposing the constraint can help the convergence of the parameter estimation to the true value.

Three cases of different initial guesses are simulated with constraint imposed by re-weighing individual ensembles based on their likelihood of satisfying the constraint (see (6.26)). The covariances are $\Sigma_\theta = [1, 0; 0, 1]$ and $\Sigma_l = 0.01$, which are kept the same as previous simulations. The covariance of the constraint used here is $\Sigma_c = 2.0$, which defines a certainty about the constraint. The simulation results are shown in Table 6.2 and visualized in Figure 6.6 (left). It can be seen that the solution converges to the true value $(1, 1)$ when

starting from $(0, 0)$ and $(2, 2)$, and the solution converges to the local minimum Group II when starting from $(-2, -2)$. It is interesting to note that the middle initial point $(0, 0)$, which originally converges to Group II, now is able to converge to the true value $(1, 1)$.

The reason that the solution starting from the lower left initial guess $(-2, -2)$ cannot converges to the true value $(1, 1)$ is because it is too far way from the true value and the variance of the prior is not large enough to sample the parameter space near the true value $(1, 1)$. Therefore, even though the constraint has been imposed, the solution cannot converge to the true value. To verify this, we simulated the three different starting locations with a larger prior variance $\Sigma_\theta = [3, 0; 0, 3]$, while the covariance of the data likelihood $\Sigma_l = 0.01$ and the covariance of the the constraint $\Sigma_c = 2.0$ are kept the same. The simulation results are shown in Table 6.3 and visualized in Figure 6.6 (middle), demonstrating that all the three initial guesses lead to the true parameter value $(1, 1)$.

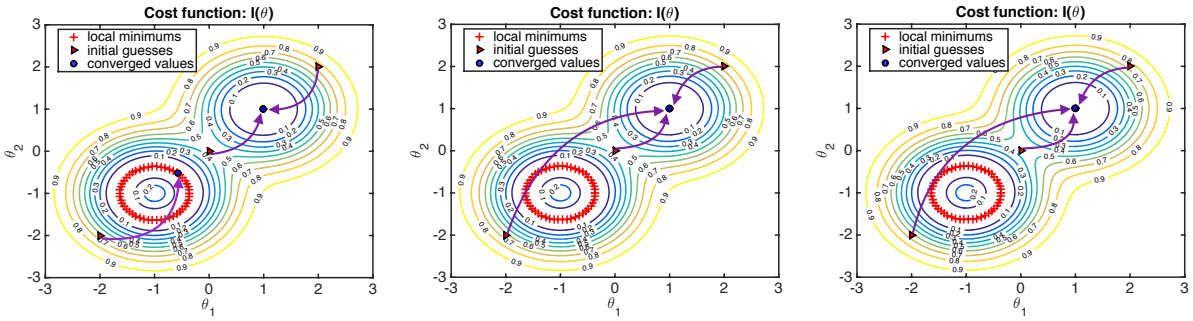

Figure 6.6: Parameter convergence results with constraint imposed. (Left) When $\Sigma_\theta = [1, 0; 0, 1]$ and $\Sigma_c = 2.0$, the initial guesses at the $(2, 2)$ and $(0, 0)$ converge to the true local minimum $(1, 1)$; (Middle) When $\Sigma_\theta = [3, 0; 0, 3]$ and $\Sigma_c = 2.0$, all initial guesses converge to the true local minimum $(1, 1)$; (Right) When $\Sigma_\theta = [1, 0; 0, 1]$ and $\Sigma_c = 1.0$, all initial guesses converge to the true local minimum $(1, 1)$.

As a further test, we decreased the variance of the constraint Σ_c to 1.0 to see how this influences the parameter estimation. The results in Table 6.4 and Figure 6.6 (right) demonstrate that (contrary to original conditions in the left panel) all three initial guesses converge to the true parameter value $\theta^* = (1, 1)$. Thus decreasing the variance of the constraint can also improve convergence to the true parameter value in cases where the constraint is more certain.

6.3.4 Relation between Bayesian inference and optimization

Using Bayesian inference framework to estimate the unknown model parameters is intrinsically related to solving a corresponding optimization problem [8]. To see this, we write out the posterior probability distribution of the unknown parameter θ conditioned on the

θ^0	(-2, -2)	(0, 0)	(2, 2)
θ^*	(-0.5685, -0.5173)	(0.9839, 1.0013)	(0.9837, 1.0015)
$HF(\theta^*)$	-0.9948	-0.9958	-0.9958
Group	II	I	I

Table 6.2: Simulation results with the constraint imposed for different initial guesses with $\Sigma_\theta = [1, 0; 0, 1]$, $\Sigma_l = 0.01$ and $\Sigma_c = 2.0$.

θ^0	(-2 , -2)	(0, 0)	(2, 2)
θ^*	(0.9947, 0.9962)	(0.9958, 0.9943)	(0.9955, 0.9942)
$HF(\theta^*)$	-0.9859	-0.9897	-0.9908
Group	I	I	I

Table 6.3: Simulation results with the constraint imposed for different initial guesses with $\Sigma_\theta = [3, 0; 0, 3]$, $\Sigma_l = 0.01$ and $\Sigma_c = 2.0$.

θ^0	(-2, -2)	(0, 0)	(2, 2)
θ^*	(0.9976, 0.9984)	(0.9888, 1.0063)	(0.9863, 1.0087)
$HF(\theta^*)$	-0.9888	-0.9957	-0.9962
Group	I	I	I

Table 6.4: Simulation results with the constraint imposed for different initial guesses with $\Sigma_\theta = [1, 0; 0, 1]$, $\Sigma_l = 0.01$ and $\Sigma_c = 1.0$.

observed data $\mathcal{D}$ and the fact that the constraint needs to be satisfied,

$$\begin{aligned} p(\theta|\mathcal{D}, G(x) = \mathbf{0}) &\propto p(\mathcal{D}|\theta)p(G(x) = \mathbf{0}|\theta)p(\theta) \\ &= \frac{1}{Z'} \exp\left(-\frac{1}{2}\left\|\Sigma_\theta^{-\frac{1}{2}}(\theta - \hat{\theta})\right\|^2 - \frac{1}{2}\left\|\Sigma_l^{-\frac{1}{2}}(y - HF(\theta))\right\|^2 \right. \\ &\quad \left. -\frac{1}{2}\left\|\Sigma_c^{-\frac{1}{2}}G(F(\theta))\right\|^2\right) , \end{aligned} \tag{6.39}$$

where Z' is a normalization constant. As mentioned before, the final estimation of the parameter θ can be taken as the posterior expectation $\mathbb{E}(\theta|\mathcal{D}, G(x) = \mathbf{0})$, or as the value that maximizes the posterior probability (MAP)

$$\theta^* = \arg\max_\theta p(\theta|\mathcal{D}, G(x) = \mathbf{0}) . \tag{6.40}$$

Based on (6.39), solving the MAP estimation of θ is equivalent to the following optimization problem:

$$\min_{\theta} \left\| \Sigma_{\theta}^{-\frac{1}{2}} (\theta - \hat{\theta}) \right\|^2 + \left\| \Sigma_{l}^{-\frac{1}{2}} (y - HF(\theta)) \right\|^2 + \left\| \Sigma_{c}^{-\frac{1}{2}} G(F(\theta)) \right\|^2 , \tag{6.41}$$

where the three terms in the cost function from left to right represent the contributions from the prior, the data and the constraint. Therefore using Bayesian inference to estimate model parameters is equivalently solving an optimization problem of minimizing the miss-match between the observed output and the reconstructed output, while penalizing based on the prior and satisfaction of the constraints. It is easier to see the relations between different terms if we assume all quantities are scalar:

$$\min_{\theta} \frac{1}{\sigma_{\theta}^2} \|\theta - \hat{\theta}\|^2 + \frac{1}{\sigma_{l}^2} \|y - HF(\theta)\|^2 + \frac{1}{\sigma_{c}^2} \|G(F(\theta))\|^2 . \tag{6.42}$$

It can be seen that the variances of the prior, the data and the constraints define the relative importance of each individual terms. The smaller the variance, the more important the corresponding term is in the cost function. This is reasonable because the information source with smaller belief uncertainty should naturally get more weight. Increasing the variance of the prior σ_{θ} not only samples a broader region but also places more relative weight on satisfying the constraint, which is why increasing the variance of the prior led to convergence of all three initial guesses to the true value (see Table 6.3 and Figure 6.6 (middle)). Similarly, decreasing the variance of the constraint can also put more relative weight on the constraint, which is verified in the results shown in Table 6.4 and Figure 6.6 (right). In the cases of multiple constraints, the variance for each constraint can be used to tune the relative importance of the constraint.

6.3.5 Extensions

The constrained Bayesian inference approach here was developed to address non-uniqueness of the solutions for inverse problems. However, it can also be extended as a way to solve more general constrained optimization problems. An advantage of this approach, compared to traditional gradient-based optimization, is that it is derivative-free and does not require construction of the cost function gradient. Gradient information is implicitly represented by the ensemble. This approach can also provide a potential framework to incorporate domain knowledge in learning models to accelerate convergence and improve accuracy.

Although we assumed Gaussian distributions, this approach can be extended to non-Gaussian distributions. This ultimately leads to a different "weighting" on the ensemble members (see Eq. (6.25)). Applying different distributions for the constraints, prior or data can be useful. For example, assuming a Laplace likelihood for the constraint results in L_1-regularization instead of L_2-regularization in (6.41), and a skew likelihood for the constraint will result in different strictness on either side of the constraint surface in parameter space.

6.4 Conclusion

To address the non-uniqueness of the feasible solutions for ill-posed inverse problems due to model complexity and lack of observation dimension, we here proposed a general method to constrain the inverse problem in a Bayesian inference framework. The constraint is imposed by constructing a likelihood function denoting the fitness of a solution. Then the posterior distribution for the unknown parameter conditioned on both the observation data and the constraint is obtained, and the final parameter estimation is given by the MAP estimation or the posterior mean. This method was also extended to an approximate Bayesian inference framework in terms of the ensemble Kalman filter, which was shown to lead to a re-weighing of ensemble members based on their fitness to the constraint. Numerical simulations were carried out to demonstrate the effectiveness of this approach for basic proof-of-concept.

Chapter 7

Conclusions

This thesis focused on two main tasks: (1) mathematical modeling of vascular adaptation and the homeostatic state; (2) improving data filtering methods from a Bayesian inference perspective for nonlinear inverse problems arising from model calibration.

In Chapter 2, a computational framework to couple vascular growth and remodeling (G&R) with blood flow simulation in a 3D patient-specific geometry was presented. Hyperelastic and anisotropic properties were considered for the vessel wall material and a constrained mixture model was used to represent multiple constituents in the vessel wall, which was modeled as a membrane. The coupled simulation was divided into two time scales – a longer time scale for G&R and a shorter time scale for fluid dynamics simulation. G&R was simulated to evolve the boundary of the fluid domain, and the fluid simulation was in turn used to generate wall shear stress and transmural pressure data that regulated G&R. To minimize required computation cost, the fluid dynamics were only simulated when G&R caused significant vascular geometric change. For demonstration, this coupled model was used to study the influence of stress-mediated growth parameters and blood flow mechanics on the behavior of the vascular tissue growth in a model of the infrarenal aorta derived from medical image data.

In Chapter 3, a method to numerically generate vascular homeostatic state for patient-specific geometries was proposed. First, a growth based algorithm was designed to generate a proper residual stress distribution such that the vascular stress was equal to a prescribed homeostatic stress distribution at physiological pressure. This method was supplemented through supervised learning to estimate and correct residual stresses at geometrically complex regions, which could be viewed as a regularization process at locations where stresses tended to significantly deviate from homeostatic values. The framework was also extended to include stress-driven fiber deposition through an optimization process, which defined the distribution of the fiber alignments in the vascular homeostatic state. Numerical simulations were conducted to test this two-stage homeostasis generation algorithm in both an idealized cylinder and a patient-specific bifurcation geometry, yielding results that agreed favorably with prior numerical and experimental data.

In Chapter 4, a stability analysis was conducted for governing equations of vascular adap-

tation around vascular homeostatic state. We started from the integral state equations of the continuum-based constrained mixture theory of vascular growth and remodeling and obtained a system of time-delayed differential equations describing vascular growth. By employing an exponential form of the constituent survival function, the delayed differential equations could be reduced to a nonlinear ODE system. We demonstrated the degeneracy of the linearized system about the homeostatic state, which was a fundamental cause of the neutral stability observations reported in prior studies. Due to this degeneracy, stability conclusions for the original nonlinear system could not be directly inferred. To resolve this problem, a sub-system was constructed by recognizing a linear relation between two states. Subsequently, Lyapunov's indirect method was used to connect stability properties between the linearized system and the original nonlinear system, to rigorously establish the neutral stability properties of the original system. In particular, this analysis led to a stability criterion for vascular expansion in terms of growth and remodeling kinetic parameters, geometric quantities and material properties. Numerical simulations were conducted to evaluate the theoretical stability criterion under broader conditions, as well as study the influence of key parameters and physical factors on growth properties. The theoretical results were also compared with prior numerical and experimental findings in the literature.

In Chapter 5, we provided a comprehensive convergence analysis of the IEnKF and proposed a new method to improve its convergence. First, the need for iterations in nonlinear inverse problems was established. Namely, the IEnKF was shown to construct a constrained optimization problem, which solved for model parameters that minimizes the innovation while satisfying the forward model. Second, a theoretical analysis of the standard IEnKF was considered and the declining utility of the Kalman updates on the ensemble covariances was revealed. Third, we demonstrated that the interaction between the nonlinearity of the forward model and the diminishing effect of the Kalman updates resulted in "early stopping" of the IEnKF, i.e. the Kalman gain converged to zero before the innovation was minimized. Furthermore, the steady state behavior of the early stopping phenomenon and its relation to observation uncertainty was demonstrated. We then proposed an approach to prevent the early stopping by perturbing the covariance with hidden parameter ensemble resampling. The ensemble mean and covariance were kept unchanged during the resampling process, which guaranteed that the change of the Kalman gain at each iteration caused by resampling maintained correct Kalman update directions. Furthermore, we demonstrated the influence of the kurtosis of the resampling distribution on convergence. Parallel to the above developments, a synthetic model was presented to demonstrate the early stopping effect, and the application and merit of the proposed resampling scheme.

In Chapter 6, we proposed an approach to improve parameter estimation in ill-posed nonlinear inverse problems by incorporating constraints in a Bayesian inference framework. Constraints were imposed by constructing a likelihood function based on fitness of the solution to the constraints. The posterior distribution of the parameters conditioned on (1) the observed data and (2) satisfaction of the constraints was obtained, and the estimate of the parameters was given by the maximum a posteriori estimation or posterior mean. Both equality and inequality constraints could be considered by this framework, and the strictness

of the constraints could be controlled by constraint uncertainty denoting a confidence on its correctness. Furthermore, we extended this framework to an approximate Bayesian inference framework in terms of the ensemble Kalman filter method, where the constraint was imposed by re-weighing the ensemble members based on the likelihood function. A synthetic model was presented to demonstrate the effectiveness of the proposed method and in both the exact Bayesian inference and ensemble Kalman filter scenarios, numerical simulations showed that imposing constraints using the method presented improved identification of the true parameter solution among multiple local minima.

Beyond the topics discussed in this thesis, there are several other topics that need future research. For modeling vascular adaptation and homeostasis, we only considered the effect of mechanical stimuli (wall tension and wall shear stress) while biochemical stimuli also play an important role. With the help of more advanced imaging techniques (such as PET-CT), more information about the mechanotransduction signaling cascades can be revealed, which characterizes the vascular adaption at the cellular level. Inclusion of a cellular level sub-module into the current coupled simulation framework can reveal more interesting dynamical behavior of vascular adaptation. This will not only help us to better understand vascular homeostasis but can also potentially provide more accurate predictions for related disease progressions such as aneurysm growth. For the model calibration portion of the work presented herein, the methods we developed are motivated by modeling biomedical systems but can be extended to implementations in other fields. For example, the idea of adding constraints via Bayesian inference framework can be combined with generic machine learning problems to either accelerate convergence rate or eliminate irrelevant local minima. The methods to incorporate more complicated constraints such as differential equations are also worth being studied in future works.

Bibliography

[1] H. Abdul-Hussien et al. "Collagen degradation in the abdominal aneurysm: a conspiracy of matrix metalloproteinase and cysteine collagenases". In: *The American Journal of Pathology* 170.3 (2007), pp. 809–817.

[2] V. Alastrué et al. "Assessing the use of the "opening angle method" to enforce residual stresses in patient-specific arteries". In: *Annals of Biomedical Engineering* 35.10 (2007), pp. 1821–1837.

[3] V. Alastrué et al. "Numerical framework for patient-specific computational modelling of vascular tissue". In: *International Journal for Numerical Methods in Biomedical Engineering* 26.1 (2010), pp. 35–51. ISSN: 20407939. DOI: 10.1002/cnm.1234.

[4] J. Anderson. "An adaptive covariance inflation error correction algorithm for ensemble filters". In: *Tellus A: Dynamic Meteorology and Oceanography* 59.2 (2007), pp. 210–224.

[5] J. Anderson. "Spatially and temporally varying adaptive covariance inflation for ensemble filters". In: *Tellus A: Dynamic Meteorology and Oceanography* 61.1 (2009), pp. 72–83.

[6] J. Anderson and S. Anderson. "A Monte Carlo implementation of the nonlinear filtering problem to produce ensemble assimilations and forecasts". In: *Monthly Weather Review* 127.12 (1999), pp. 2741–2758.

[7] P. Aparício et al. "Modelling the influence of endothelial heterogeneity on the progression of arterial disease: Application to abdominal aortic aneurysm evolution". In: *International Journal for Numerical Methods in Biomedical Engineering* 30.5 (2014), pp. 563–586.

[8] A. Aravkin, J. Burke, and G. Pillonetto. "Optimization viewpoint on Kalman smoothing with applications to robust and sparse estimation". In: *Compressed Sensing and Sparse Filtering*. Springer, 2014, pp. 237–280.

[9] M. Asch, M. Bocquet, and M. Nodet. *Data assimilation: methods, algorithms, and applications*. Vol. 11. SIAM, 2016.

[10] C. M. Augustin, G. A. Holzapfel, and O. Steinbach. "Classical and all-floating FETI methods for the simulation of arterial tissues". In: *International journal for numerical methods in engineering* 99.4 (2014), pp. 290–312.

[11] G. M. Austin, W. Schievink, and R. Williams. "Controlled pressure-volume factors in the enlargement of intracranial aneurysms." In: *Neurosurgery* 24.5 (1989), pp. 722–730.

[12] S. Baek, K. R. Rajagopal, and J. D. Humphrey. "A theoretical model of enlarging intracranial fusiform aneurysms". In: *Journal of Biomechanical Engineering* 128.1 (2006), pp. 142–149.

[13] S. Baek, K. R. Rajagopal, and J. D. Humphrey. "Competition between radial expansion and thickening in the enlargement of an intracranial saccular aneurysm". In: *Journal of Elasticity* 80.1-3 (2005), pp. 13–31.

[14] C. Bellini et al. "A microstructurally motivated model of arterial wall mechanics with mechanobiological implications". In: *Annals of Biomedical Engineering* 42.3 (2014), pp. 488–502.

[15] K. Bergemann and S. Reich. "A localization technique for ensemble Kalman filters". In: *Quarterly Journal of the Royal Meteorological Society* 136.648 (2010), pp. 701–707.

[16] K. Bergemann and S. Reich. "A mollified ensemble Kalman filter". In: *Quarterly Journal of the Royal Meteorological Society* 136.651 (2010), pp. 1636–1643.

[17] T. Berry and T. Sauer. "Adaptive ensemble Kalman filtering of non-linear systems". In: *Tellus A: Dynamic Meteorology and Oceanography* 65.1 (2013), p. 20331.

[18] J. G. Betts et al. "Anatomy and physiology". In: (2014).

[19] D. K. Bogen and T. A. McMahon. "Do cardiac aneurysms blow out?" In: *Biophysical Journal* 27.2 (1979), p. 301.

[20] J. Bols et al. "A computational method to assess the in vivo stresses and unloaded configuration of patient-specific blood vessels". In: *Journal of Computational and Applied Mathematics* 246 (2013), pp. 10–17.

[21] M. L. Bots et al. "Isolated systolic hypertension and vessel wall thickness of the carotid artery. The Rotterdam Elderly Study." In: *Arteriosclerosis, Thrombosis, and Vascular Biology* 13.1 (1993), pp. 64–69.

[22] A. C. Burton. "Relation of structure to function of the tissues of the wall of blood vessels". In: *Physiol. Rev* 34.6 (1954).

[23] R. Bustamante and G. A. Holzapfel. "Methods to compute 3D residual stress distributions in hyperelastic tubes with application to arterial walls". In: *Int. J. Eng. Sci.* 48.11 (2010), pp. 1066–1082. ISSN: 00207225. DOI: 10.1016/j.ijengsci.2010.06.005.

[24] E. Choke et al. "A review of biological factors implicated in abdominal aortic aneurysm rupture". In: *European Journal of Vascular and Endovascular Surgery* 30.3 (2005), pp. 227–244.

[25] C. J. Chuong and Y. C. Fung. "Residual stress in arteries". In: *Frontiers in Biomechanics*. Springer, 1986, pp. 117–129.

[26] C. J. Chuong and Y. C. Fung. "Three-Dimensional Stress Distribution in Arteries". In: *Journal of Biomechanical Engineering* 105.3 (1983), p. 268. ISSN: 01480731. DOI: 10.1115/1.3138417.

[27] S. L. Cotter et al. "Bayesian inverse problems for functions and applications to fluid mechanics". In: *Inverse problems* 25.11 (2009), p. 115008.

[28] C. J. Cyron, R. C. Aydin, and J. D. Humphrey. "A homogenized constrained mixture (and mechanical analog) model for growth and remodeling of soft tissue". In: *Biomechanics and modeling in mechanobiology* 15.6 (2016), pp. 1389–1403.

[29] C. J. Cyron and J. D. Humphrey. "Preferred fiber orientations in healthy arteries and veins understood from netting analysis". In: *Mathematics and Mechanics of Solids* 20.6 (2015), pp. 680–696. ISSN: 17413028. DOI: 10.1177/1081286514551495.

[30] C. J. Cyron and J. D. Humphrey. "Vascular homeostasis and the concept of mechanobiological stability". In: *International Journal of Engineering Science* 85 (2014), pp. 203–223.

[31] C. J. Cyron, J. S. Wilson, and J. D. Humphrey. "Mechanobiological stability: a new paradigm to understand the enlargement of aneurysms?" In: *Journal of the Royal Society Interface* 11.100 (2014), p. 20140680.

[32] S. De, F. Guilak, and M. Mofrad. *Computational modeling in biomechanics*. Springer, 2010.

[33] P. Del Moral, A. Doucet, and A. Jasra. "Sequential monte carlo samplers". In: *Journal of the Royal Statistical Society: Series B (Statistical Methodology)* 68.3 (2006), pp. 411–436.

[34] J. M. Dijk et al. "Increased arterial stiffness is independently related to cerebrovascular disease and aneurysms of the abdominal aorta the Second Manifestations of Arterial Disease (SMART) Study". In: *Stroke* 35.7 (2004), pp. 1642–1646.

[35] K. L. Dorrington and N. G. McCrum. "Elastin as a rubber". In: *Biopolymers* 16.6 (1977), pp. 1201–1222.

[36] M. Esmaily Moghadam et al. "A modular numerical method for implicit 0D/3D coupling in cardiovascular finite element simulations". In: *Journal of Computational Physics* 244 (2013), pp. 63–79.

[37] N. Etminan et al. "Age of collagen in intracranial saccular aneurysms". In: *Stroke* 45.6 (2014), pp. 1757–1763.

[38] G. Evensen. "Sequential data assimilation with a nonlinear quasi-geostrophic model using Monte Carlo methods to forecast error statistics". In: *Journal of Geophysical Research: Oceans* 99.C5 (1994), pp. 10143–10162.

[39] G. Evensen. "The ensemble Kalman filter: Theoretical formulation and practical implementation". In: *Ocean dynamics* 53.4 (2003), pp. 343–367.

[40] D. G. Ezra et al. "Changes in fibroblast mechanostat set point and mechanosensitivity: an adaptive response to mechanical stress in floppy eyelid syndrome". In: *Investigative ophthalmology & visual science* 51.8 (2010), pp. 3853–3863.

[41] C. A. Figueroa et al. "A computational framework for fluid–solid-growth modeling in cardiovascular simulations". In: *Computer Methods in Applied Mechanics and Engineering* 198.45 (2009), pp. 3583–3602.

[42] C. A. Figueroa et al. "A computational framework for fluid–solid-growth modeling in cardiovascular simulations". In: *Computer Methods in Applied Mechanics and Engineering* 198.45-46 (2009), pp. 3583–3602.

[43] C. A. Figueroa et al. "NIH Public Access". In: *Methods* 198 (2010), pp. 3583–3602. DOI: 10.1016/j.cma.2008.09.013.A.

[44] H. M. Finlay, L. McCullough, and P. B. Canham. "Three-dimensional collagen organization of human brain arteries at different transmural pressures". In: *Journal of Vascular Research* 32.5 (1995), pp. 301–312.

[45] H. M Finlay, P. Whittaker, and P. B. Canham. "Collagen organization in the branching region of human brain arteries". In: *Stroke* 29.8 (1998), pp. 1595–1601.

[46] P. J. Flory. "Thermodynamic relations for high elastic materials". In: *Transactions of the Faraday Society* 57 (1961), pp. 829–838.

[47] J. Friedman, T. Hastie, and R. Tibshirani. *The elements of statistical learning*. Vol. 1. Springer series in statistics New York, 2001.

[48] Y. C. Fung. "Mechanical properties and active remodeling of blood vessels". In: *Biomechanics*. Springer, 1993, pp. 321–391.

[49] Y. C. Fung. "What are the residual stresses doing in our blood vessels?" In: *Annals of Biomedical Engineering* 19.3 (1991), pp. 237–249.

[50] J. R. Gardner et al. "Bayesian Optimization with Inequality Constraints." In: *ICML*. 2014, pp. 937–945.

[51] T. C. Gasser, R. W. Ogden, and G. A. Holzapfel. "Hyperelastic modelling of arterial layers with distributed collagen fibre orientations". In: *J. R. Soc. Interface* 3.6 (2006), pp. 15–35. DOI: 10.1098/rsif.2005.0073. eprint: 0312002v1 (arXiv:q-bio).

[52] J. Geest, M. S. Sacks, and D. A. Vorp. "Age dependency of the biaxial biomechanical behavior of human abdominal aorta". In: *Journal of Biomechanical Engineering* 126.6 (2004), pp. 815–822.

[53] C. Geuzaine and J. Remacle. "Gmsh: A 3-D finite element mesh generator with built-in pre-and post-processing facilities". In: *International Journal for Numerical Methods in Engineering* 79.11 (2009), pp. 1309–1331.

[54] A. Grytsan et al. "Growth Description for Vessel Wall Adaptation: A Thick-Walled Mixture Model of Abdominal Aortic Aneurysm Evolution". In: *Materials* 10.9 (2017), p. 994. ISSN: 1996-1944. DOI: 10.3390/ma10090994. URL: http://www.mdpi.com/1996-1944/10/9/994.

[55] O. Gültekin, H. Dal, and G. A. Holzapfel. "On the quasi-incompressible finite element analysis of anisotropic hyperelastic materials". In: *Computational mechanics* 63.3 (2019), pp. 443–453.

[56] I. Hariton, T. C. Gasser, G. A. Holzapfel, et al. "Stress-modulated collagen fiber remodeling in a human carotid bifurcation". In: *Journal of Theoretical Biology* 248.3 (2007), pp. 460–470.

[57] S. Haykin. *Kalman filtering and neural networks*. Vol. 47. John Wiley & Sons, 2004.

[58] Y. He and D. Xiu. "Numerical strategy for model correction using physical constraints". In: *Journal of Computational Physics* 313 (2016), pp. 617–634.

[59] J. Helfenstein et al. "On non-physical response in models for fiber-reinforced hyperelastic materials". In: *International Journal of Solids and Structures* 47.16 (2010), pp. 2056–2061.

[60] G. A. Holzapfel. "Determination of material models for arterial walls from uniaxial extension tests and histological structure". In: *Journal of theoretical biology* 238.2 (2006), pp. 290–302.

[61] G. A. Holzapfel, T. C. Gasser, and R. W. Ogden. "A new constitutive framework for arterial wall mechanics and a comparative study of material models". In: *Journal of Elasticity and the Physical Science of Solids* 61.1-3 (2000), pp. 1–48.

[62] G. A. Holzapfel, T. C. Gasser, and M. Stadler. "A structural model for the viscoelastic behavior of arterial walls: continuum formulation and finite element analysis". In: *European Journal of Mechanics-A/Solids* 21.3 (2002), pp. 441–463.

[63] G. A. Holzapfel and R. W. Ogden. "Modelling the layer-specific three-dimensional residual stresses in arteries, with an application to the human aorta." In: *J. R. Soc. Interface* 7.46 (2010), pp. 787–799. ISSN: 1742-5689. DOI: 10.1098/rsif.2009.0357.

[64] G. A. Holzapfel and R. W. Ogden. "On Fiber Dispersion Models: Exclusion of Compressed Fibers and Spurious Model Comparisons". In: *J. Elast.* 129.1-2 (2017), pp. 49–68. ISSN: 0374-3535. DOI: 10.1007/s10659-016-9605-2.

[65] G. A. Holzapfel and R. W. Ogden. "On the tension-compression switch in soft fibrous solids". In: *European Journal of Mechanics - A/Solids* 49 (2015), pp. 561–569. ISSN: 0997-7538. DOI: 10.1016/J.EUROMECHSOL.2014.09.005.

[66] G. A. Holzapfel et al. "Layer-Specific 3D Residual Deformations of Human Aortas with Non-Atherosclerotic Intimal Thickening". In: *Ann. Biomed. Eng.* 35.4 (2007), pp. 530–545. ISSN: 0090-6964. DOI: 10.1007/s10439-006-9252-z.

[67] Y. Huang et al. "Common iliac artery aneurysm: expansion rate and results of open surgical and endovascular repair". In: *Journal of Vascular Surgery* 47.6 (2008), pp. 1203–1211.

[68] J. D. Humphrey. *Cardiovascular Solid Mechanics: Cells, Tissues, and Organs*. New York, NY: Springer New York, 2002, p. 757. ISBN: 0387951687. DOI: 10.1017/CBO9781107415324.004. arXiv: arXiv:1011.1669v3.

[69] J. D. Humphrey. *Cardiovascular Solid Mechanics: Cells, Tissues, and Organs*. Springer-Verlag New York, 2013.

[70] J. D. Humphrey. "Towards a Theory of Vascular Growth and Remodeling". In: *Mechanics of Biological Tissue*. Ed. by GA Holzapfel and RW Ogden. Springer Berlin Heidelberg, 2006, pp. 3–15. DOI: 10.1007/3-540-31184-X_1.

[71] J. D. Humphrey. "Vascular adaptation and mechanical homeostasis at tissue, cellular, and sub-cellular levels". In: *Cell Biochemistry and Biophysics* 50.2 (2008), pp. 53–78. DOI: 10.1007/s12013-007-9002-3.

[72] J. D. Humphrey and G. A. Holzapfel. "Mechanics, mechanobiology, and modeling of human abdominal aorta and aneurysms". In: *Journal of Biomechanics* 45.5 (2012), pp. 805–814.

[73] J. D. Humphrey and S. Na. "Elastodynamics and arterial wall stress". In: *Ann. Biomed. Eng.* 30.4 (2002), pp. 509–523. ISSN: 00906964. DOI: 10.1114/1.1467676. arXiv: 0035988856.

[74] J. D. Humphrey and S. L. O'Rourke. *An introduction to biomechanics: Solids and fluids, analysis and design, second edition*. Vol. 102. Pt 1. New York, NY: Springer New York, 2015, pp. 1–692. ISBN: 9781493926237. DOI: 10.1007/978-1-4939-2623-7.

[75] J. D. Humphrey and K. R. Rajagopal. "A constrained mixture model for growth and remodeling of soft tissues". In: *Mathematical Models and Methods in Applied Sciences* 12.03 (2002), pp. 407–430.

[76] M. A. Iglesias, K. Law, and A. M. Stuart. "Ensemble Kalman methods for inverse problems". In: *Inverse Problems* 29.4 (2013), p. 045001.

[77] M. A. Iglesias, K. Lin, and A. M. Stuart. "Well-posed Bayesian geometric inverse problems arising in subsurface flow". In: *inverse problems* 30.11 (2014), p. 114001.

[78] S. J. Julier and J. K. Uhlmann. "Unscented filtering and nonlinear estimation". In: *Proceedings of the IEEE* 92.3 (2004), pp. 401–422.

[79] R. E. Kalman. "A new approach to linear filtering and prediction problems". In: *Journal of basic Engineering* 82.1 (1960), pp. 35–45.

[80] H. Kato et al. "A data assimilation methodology for reconstructing turbulent flows around aircraft". In: *Journal of Computational Physics* 283 (2015), pp. 559–581.

[81] K. Law, A. M. Stuart, and K. Zygalakis. "Data assimilation". In: *Cham, Switzerland: Springer* (2015).

[82] K. Li, R. W. Ogden, and G. A. Holzapfel. "An Exponential Constitutive Model Excluding Fibers Under Compression: Application to Extension-Inflation of a Residually Stressed Carotid Artery". In: *Mathematics and Mechanics of Solids* (2017), pp. 1–30. DOI: 10.1177/1081286517712077.

[83] Z. Li et al. "A data-driven adaptive Reynolds-averaged Navier–Stokes k–ω model for turbulent flow". In: *Journal of Computational Physics* 345 (2017), pp. 111–131.

[84] A. Logg, K. Mardal, and G. Wells. *Automated solution of differential equations by the finite element method: The FEniCS book*. Vol. 84. Springer Science & Business Media, 2012.

[85] A. J. Majda and X. Tong. "Performance of Ensemble Kalman filters in large dimensions". In: *Communications on Pure and Applied Mathematics* 71.5 (2018), pp. 892–937.

[86] A. Malek and S. Izumo. "Physiological fluid shear stress causes downregulation of endothelin-1 mRNA in bovine aortic endothelium". In: *American Journal of Physiology-Cell Physiology* 263.2 (1992), pp. C389–C396.

[87] H. Niedermüller et al. "Investigations on the kinetics of collagen-metabolism in young and old rats". In: *Experimental Gerontology* 12.5 (1977), pp. 159–168.

[88] J. A. Niestrawska et al. "Microstructure and mechanics of healthy and aneurysmatic abdominal aortas: experimental analysis and modelling". In: *Journal of The Royal Society Interface* 13.124 (2016), p. 20160620.

[89] R. Nissen, G. J. Cardinale, and S. Udenfriend. "Increased turnover of arterial collagen in hypertensive rats". In: *Proceedings of the National Academy of Sciences* 75.1 (1978), pp. 451–453.

[90] F. Pedregosa et al. "Scikit-learn: Machine learning in Python". In: *Journal of Machine Learning Research* 12.Oct (2011), pp. 2825–2830.

[91] P. Penfield Jr. "Principle of maximum entropy". In: *Information, Entropy and Computation* (2010), pp. 104–12.

[92] D. A. Peter et al. "Fluid structure interaction with contact surface methodology for evaluation of endovascular carotid implants for drug-resistant hypertension treatment". In: *Journal of Biomechanical Engineering* 134.4 (2012), p. 041001.

[93] D. M. Pierce et al. "A method for incorporating three-dimensional residual stretches/stresses into patient-specific finite element simulations of arteries". In: *Journal of the Mechanical Behavior of Biomedical Materials* 47 (2015), pp. 147–164.

[94] M. Rizvi and P. R. Myers. "Nitric oxide modulates basal and endothelin-induced coronary artery vascular smooth muscle cell proliferation and collagen levels". In: *Journal of Molecular and Cellular Cardiology* 29.7 (1997), pp. 1779–1789.

[95] M. Rizvi et al. "The effects of endothelin-1 on collagen type I and type III synthesis in cultured porcine coronary artery vascular smooth muscle cells". In: *Journal of Molecular and Cellular Cardiology* 28.2 (1996), pp. 243–252.

[96] M. R. Roach and A. C. Burton. "The reason for the shape of the distensibility curves of arteries". In: *Can. J. Biochem. Physiol.* 35.8 (1957), pp. 681–690. ISSN: 0576-5544. DOI: 10.1139/o57-080.

[97] E. K. Rodriguez, A. Hoger, and A. D. McCulloch. "Stress-dependent finite growth in soft elastic tissues". In: *Journal of Biomechanics* 27.4 (1994), pp. 455–467.

[98] M. E. Safar, M. F. O'Rourke, and E. D. Frohlich. *Blood Pressure and Arterial Wall Mechanics in Cardiovascular Diseases*. Springer, 2014.

[99] A. Salsac et al. "Evolution of the wall shear stresses during the progressive enlargement of symmetric abdominal aortic aneurysms". In: *Journal of Fluid Mechanics* 560 (2006), pp. 19–51.

[100] C. Sansour. "On the physical assumptions underlying the volumetric-isochoric split and the case of anisotropy". In: *European Journal of Mechanics-A/Solids* 27.1 (2008), pp. 28–39.

[101] G. Satha, S. B. Lindström, and A. Klarbring. "A goal function approach to remodeling of arteries uncovers mechanisms for growth instability". In: *Biomechanics and Modeling in Mechanobiology* 13.6 (2014), pp. 1243–1259.

[102] J. Satta et al. "Increased turnover of collagen in abdominal aortic aneurysms, demonstrated by measuring the concentration of the aminoterminal propeptide of type III procollagen in peripheral and aortal blood samples". In: *Journal of Vascular Surgery* 22.2 (1995), pp. 155–160.

[103] C. Schillings and A. M. Stuart. "Analysis of the ensemble Kalman filter for inverse problems". In: *SIAM Journal on Numerical Analysis* 55.3 (2017), pp. 1264–1290.

[104] C. Schillings and A. M. Stuart. "Convergence Analysis of the Ensemble Kalman Filter for Inverse Problems: the Noisy Case". In: *arXiv preprint arXiv:1602.02020v* (2017).

[105] A. Selimovic, Y. Ventikos, and P. N. Watton. "Modelling the Evolution of Cerebral Aneurysms: Biomechanics, Mechanobiology and Multiscale Modelling". In: *Procedia IUTAM* 10 (2014), pp. 396–409.

[106] X. Shao, B. Huang, and J. Lee. "Constrained Bayesian state estimation–A comparative study and a new particle filter based approach". In: *Journal of Process Control* 20.2 (2010), pp. 143–157.

[107] A. Sheidaei et al. "Simulation of abdominal aortic aneurysm growth with updating hemodynamic loads using a realistic geometry". In: *Medical Engineering & Physics* 33.1 (2011), pp. 80–88.

[108] Y. Shi et al. "Parameter estimation of a physically-based land surface hydrologic model using an ensemble Kalman filter: A multivariate real-data experiment". In: *Advances in water resources* 83 (2015), pp. 421–427.

[109] D. Simon and T. Chia. "Kalman filtering with state equality constraints". In: *IEEE transactions on Aerospace and Electronic Systems* 38.1 (2002), pp. 128–136.

[110] O. M. Smedstad and J. J. O'Brien. "Variational data assimilation and parameter estimation in an equatorial Pacific Ocean model". In: *Progress in Oceanography* 26.2 (1991), pp. 179–241.

[111] L. A. Taber. "A model for aortic growth based on fluid shear and fiber stresses". In: *Journal of Biomechanical Engineering* 120.3 (1998), pp. 348–354.

[112] L. A. Taber and J. D. Humphrey. "Stress-modulated growth, residual stress, and vascular heterogeneity". In: *Journal of Biomechanical Engineering* 123.6 (2001), pp. 528–535.

[113] K. Takamizawa and K. Hayashi. "Strain energy density function and uniform strain hypothesis for arterial mechanics". In: *Journal of Biomechanics* 20.1 (1987), pp. 7–17. ISSN: 00219290. DOI: 10.1016/0021-9290(87)90262-4.

[114] X. Tong, A. J. Majda, and D. Kelly. "Nonlinear stability of the ensemble Kalman filter with adaptive covariance inflation". In: *arXiv preprint arXiv:1507.08319* (2015).

[115] M. Uematsu et al. "Regulation of endothelial cell nitric oxide synthase mRNA expression by shear stress". In: *American Journal of Physiology-Cell Physiology* 38.6 (1995), p. C1371.

[116] A. Updegrove et al. "SimVascular - An open source pipeline for cardiovascular simulation". In: *Annals of Biomedical Engineering* (2016).

[117] A. Valentín and G. A. Holzapfel. "Constrained mixture models as tools for testing competing hypotheses in arterial biomechanics: A brief survey". In: *Mechanics Research Communications* 42 (2012), pp. 126–133.

[118] A. Valentin and J. D. Humphrey. "Evaluation of fundamental hypotheses underlying constrained mixture models of arterial growth and remodelling". In: *Philosophical Transactions of the Royal Society of London A: Mathematical, Physical and Engineering Sciences* 367.1902 (2009), pp. 3585–3606.

[119] A. Valentín, J. D. Humphrey, and G. A. Holzapfel. "A finite element-based constrained mixture implementation for arterial growth, remodeling, and adaptation: Theory and numerical verification". In: *International Journal for Numerical Methods in Biomedical Engineering* 29.8 (2013), pp. 822–849.

[120] A. Valentín et al. "Complementary vasoactivity and matrix remodelling in arterial adaptations to altered flow and pressure". In: *Journal of The Royal Society Interface* 6.32 (2009), pp. 293–306.

[121] F. Verhulst. *Nonlinear Differential Equations and Dynamical Systems*. Springer-Verlag Berlin Heidelberg, 1996.

[122] W. W. Von Maltzahn, R. G. Warriyar, and W. F. Keitzer. "Experimental measurements of elastic properties of media and adventitia of bovine carotid arteries". In: *Journal of Biomechanics* 17.11 (1984), pp. 839–847. ISSN: 00219290. DOI: 10.1016/0021-9290(84)90142-8.

[123] E. A. Wan and R. Van Der Merwe. "The unscented Kalman filter for nonlinear estimation". In: *Adaptive Systems for Signal Processing, Communications, and Control Symposium 2000. AS-SPCC. The IEEE 2000*. Ieee. 2000, pp. 153–158.

[124] J. Wang, X. Hu, and S. C. Shadden. "Data-augmented modeling of intracranial pressure". In: *arXiv preprint arXiv:1807.10345* (2018).

[125] J. Wang and H. Xiao. "Data-driven CFD modeling of turbulent flows through complex structures". In: *International Journal of Heat and Fluid Flow* 62 (2016), pp. 138–149.

[126] J. Wang et al. "Inferring tsunami flow depth and flow speed from sediment deposits based on Ensemble Kalman Filtering". In: *Geophysical Journal International* 212.1 (2017), pp. 646–658.

[127] P. N. Watton, N. A. Hill, and M. Heil. "A mathematical model for the growth of the abdominal aortic aneurysm". In: *Biomechanics and Modeling in Mechanobiology* 3.2 (2004), pp. 98–113.

[128] P. N. Watton et al. "Coupling the hemodynamic environment to the evolution of cerebral aneurysms: computational framework and numerical examples". In: *Journal of Biomechanical Engineering* 131.10 (2009), p. 101003.

[129] J. S. Wilson, S. Baek, and J. D. Humphrey. "Importance of initial aortic properties on the evolving regional anisotropy, stiffness and wall thickness of human abdominal aortic aneurysms". In: *Journal of The Royal Society Interface* 9.74 (2012), pp. 2047–2058.

[130] J. S. Wilson, S. Baek, and J. D. Humphrey. "Parametric study of effects of collagen turnover on the natural history of abdominal aortic aneurysms". In: *Proceedings of the Royal Society A: Mathematical, Physical and Engineering Science* 469.2150 (2013), p. 20120556.

[131] N. M. Wilson, A. K. Ortiz, and A. B. Johnson. "The Vascular Model Repository: A public resource of medical imaging data and blood flow simulation results". In: *Journal of Medical Devices* 7.4 (2013), p. 040923.

[132] H. Wolinsky. "Long-term effects of hypertension on the rat aortic wall and their relation to concurrent aging changes: morphological and chemical studies". In: *Circulation Research* 30.3 (1972), pp. 301–309.

[133] P. Wriggers. *Nonlinear finite element methods*. Springer Science & Business Media, 2008.

[134] J. Wu and S. C. Shadden. "Coupled Simulation of Hemodynamics and Vascular Growth and Remodeling in a Subject-Specific Geometry". In: *Annals of Biomedical Engineering* 43.7 (2015), pp. 1543–1554.

[135] J. Wu, J. Wang, and S. C. Shadden. "Adding Constraints to Bayesian Inverse Problems". In: *arXiv preprint arXiv:1812.06212* (2018).

[136] Y. Ying and F. Zhang. "An adaptive covariance relaxation method for ensemble data assimilation". In: *Quarterly Journal of the Royal Meteorological Society* 141.692 (2015), pp. 2898–2906.

[137] S. Zeinali-Davarani and S. Baek. "Medical image-based simulation of abdominal aortic aneurysm growth". In: *Mechanics Research Communications* 42 (2012), pp. 107–117.

[138] S. Zeinali-Davarani, A. Sheidaei, and S. Baek. "A finite element model of stress-mediated vascular adaptation: application to abdominal aortic aneurysms". In: *Computer Methods in Biomechanics and Biomedical Engineering* 14.9 (2011), pp. 803–817.

[139] Y. Zhen and J. Harlim. "Adaptive error covariances estimation methods for ensemble Kalman filters". In: *Journal of computational physics* 294 (2015), pp. 619–638.